An alternative p-y model for the simulation of large diameter offshore monopiles for wind turbines founded on granular soils under monotonic and cyclic loading

A thesis submitted for the degree of Master of Science in Engineering to the Graduate Division of the Universidad del Norte, Barranquilla, Colombia

---

By

Melany **Gil Rueda**

Barranquilla, Colombia

February 2021

MASTER'S THESIS

Author:	Melany Gil Rueda gmelany@uninorte.edu.co Student code Nr. 200054243

Thesis title (English):	An alternative p-y model for the simulation of large diameter offshore monopiles for wind turbines founded on granular soils under monotonic and cyclic loading.
Thesis title (Spanish):	Un modelo p-y alternativo para la simulación de monopilotes offshore de gran diámetro para turbinas eólicas fundadas en suelos granulares bajo carga monotónica y cíclica.

Supervisors:	Professor William Mario Fuentes Lacouture, Ph.D. wfuentes@uninorte.edu.co Professor Vicente Manuel Andrés Mercado Puche, Ph.D. vmercado@uninorte.edu.co

Field of study:	Geotechnical Engineering.
Research line:	Offshore engineering, Finite Element Modelling, Foundation Engineering.
Research group:	GIEG, IDS.

Abstract

The offshore wind energy industry has exponentially grown during the past decades. Monopiles with large diameters and reduced slenderness ratios are the most common foundation solutions for Offshore Wind Turbines (OWTs). Such monopile foundations behave differently from the long slender piles with small diameters, for which the current design standards were developed. Therefore, further investigation on the behavior of such foundations needs to be conducted, so new design and modelling methods for large diameter monopiles are proposed and applied in the engineering practice.

In the present work, the behavior of laterally loaded monopiles in sands is investigated using a numerical approach based on three-dimensional (3D) Finite Element (FE) modelling and one-dimensional (1D) finite difference modelling. In the 3D FE simulations, hypoplastic constitutive models were used to simulate the behavior of the soil supporting the monopiles. The hypoplastic model for sands proposed by von Wolffersdorff (von Wolffersdorff, 1996) combined with the Intergranular Strain (IS) extension proposed by Niemunis and Herle (Niemunis & Herle, 1997) was used for this purpose. The FE models were built using the commercial software Abaqus Standard incorporating user material codes (UMATs). In addition, the 1D modelling of monopiles was conducted following the Beam on a Non-linear Winkler Foundation (BNWF) approach by means of a developed MATLAB script. The scope of the modelling work was narrowed to monopiles in cohesionless soils subjected to monotonic lateral loads.

For the analysis of monopiles under monotonic lateral loading conditions, a series of 3D FE simulations were conducted accounting for variations of pile geometry, soil properties and loading cases. The simulations results were used to propose and calibrate a novel 1D p-y model based on the BNWF approach for large diameter monopiles subjected to lateral loading. The p-y model was formulated in the present study considering new distributions for the ultimate soil resistance p_u and the initial subgrade modulus E_{py0} along depth, as well as a shear force at the base of the monopile. Also included in the formulation of the p-y equation was a factor that accounts for the effects of soil density and loading amplitude on

the accumulation of pile displacements under cyclic lateral loading conditions, termed as the ‘cyclic factor’. The calibration of the cyclic factor was conducted considering some FE simulations results of long-term cyclic lateral loaded monopiles previously reported in the literature. At the end, the performance of the proposed model was evaluated through comparisons with a field test and a centrifuge test.

Acknowledgment

I wish to express my sincere appreciation to my supervisors, Professors William Fuentes Lacouture and Vicente Mercado Puche, for their time and support during this research project. The consistent guidance of Professor Fuentes Lacouture was of incredible value to this work, and his enthusiasm and dedication made possible its accomplishment. Specifically, the expertise of Professor Fuentes Lacouture in the field of constitutive modelling and finite element modelling were truly appreciated during this research. To Professor Mercado Puche, I express my deep gratitude for his contribution in the supervision and revision of this thesis, and for his teachings throughout this journey. I would like to highlight how both Professors Fuentes Lacouture and Mercado Puche have inspired me with their passion for understanding the behavior of the soil in each of their areas of expertise. Finally, I am also truly grateful to my family and friends for their unconditional support and encouragement during my studies.

Table of Contents

Abstract i

Acknowledgment iii

Table of Contents iv

Chapter 1: Introduction 1

1.1. Framework of the Research Project 1

1.1.1. Wind energy 1

1.1.2. Offshore wind energy 2

1.1.3. National framework: Colombia 3

1.1.4. Foundations for offshore wind turbines 5

1.1.5. General considerations on the design of monopiles in sands 6

1.1.5.1. Loading conditions 6

1.1.5.2. Geotechnical design considerations 8

1.1.5.3. Dynamic design considerations 8

1.1.5.4. Main issues of current design approaches 9

1.2. Research justification and purpose of the research project 10

1.3. Research objectives 11

1.3.1. General objective 11

1.3.2. Specific objectives 11

1.4. Research structure and methodology 11

Chapter 2: Literature Review on laterally loaded monopiles 13

2.1. Conventional ***p-y*** analysis 13

2.1.1. ***p-y*** method and BNWF approach 13

2.1.2. $\boldsymbol{p}$-$\boldsymbol{y}$ curves 15
2.1.3. Governing beam-column differential equation 16
2.1.4. Solution of the beam-column differential equation 17
2.2. Design guidelines 19
2.2.1. List of design guidelines 19
2.2.2. API/DNV-GL-AS $\boldsymbol{p}$-$\boldsymbol{y}$ method for sands 20
2.3. State-of-the-art research 21
2.3.1. Monotonic behavior 21
2.3.2. Cyclic behavior 23
Chapter 3: Constitutive modelling of soil behavior 25
3.1. Hypoplasticity 25
3.2. Hypoplastic model for sands 26
3.3. Intergranular Strain concept 28
Chapter 4: Parametric study of monopiles under static lateral loading conditions 29
4.1. Generalities 29
4.2. Description of the FE models 29
4.2.1. Geometry and mesh 29
4.2.2. Materials 31
4.2.3. Soil-structure contact 32
4.2.4. Initial and boundary conditions 33
4.2.5. Loading conditions 37
4.2.6. Steps of analysis 37
4.2.7. Lists of FE models and simulations 38
4.3. Description of the FE simulation results 43
4.3.1. First set of simulations 43
4.3.2. Second set of simulations 47
4.3.3. Third set of simulations 51
4.3.4. Determination of the base shear reaction 52
4.3.5. Implications of the ‘wished-in-place’ approach 56
Chapter 5: *p-y* model for large diameter monopiles in sands 57
5.1. Generalities 57

5.2. Formulation of the $\boldsymbol{p}$-$\boldsymbol{y}$ model 58
5.2.1. Ultimate soil resistance 58
5.2.2. Soil reaction 64
5.2.3. Initial subgrade reaction modulus 64
5.2.4. Base shear reaction 65
5.2.5. Cyclic loading factor 67
5.3. Calibration and evaluation of the $\boldsymbol{p}$-$\boldsymbol{y}$ model 71
5.3.1. Methodology 71
5.3.2. Base shear reaction 71
5.3.3. Static analysis 72
5.3.4. Cyclic behavior 78
5.4. Evaluation of model performance with field and centrifuge tests 84
5.4.1. Simulation of a Centrifuge test 84
5.4.2. Simulation of Field tests 88
Chapter 6: Conclusions and Outlook 92
6.1. Summary of conclusions 92
6.2. Outlook 93
Bibliography 95

Chapter 1: Introduction

1.1. Framework of the Research Project

1.1.1. Wind energy

According to the Global Renewables Outlook report by the International Renewable Energy Agency (IRENA), carbon dioxide emissions related to the energy industry have been increasing year over year for the past decade at a rate of 1 per cent per year (IRENA, 2020). However, as stated in the mentioned report, emissions should instead reduce by a minimum of 3.8 per cent each year to ensure a climate-safe energy system. The need for energy decarbonization is imminent considering the increasing negative environmental effects of climate change, like air, water and soil pollution. Global and regional commitments have been made to address this problem and to guide the transformation of the global energy system to a sustainable zero-carbon system. Some examples are the United Nations 2030 Agenda, the Paris Agreement in 2015 and the European Green Deal. In the years to come, in order to meet the stablished sustainability goals, policy initiatives and investments into the global renewable energy infrastructure will be needed.

Modern renewable energy markets provide a major contribution for the energy decarbonization plans. According to the IRENA, these markets represent nowadays, apart from traditional uses of bioenergy, about 10 per cent of the global energy consumption (IRENA, 2020). However, their contribution has to increase up to 66 per cent in order to keep the global temperature rise below 2 °C during this century, as it is desired. Wind energy is a type of modern renewable energy that has been exploited worldwide for the past decades and it is expected to grow significantly in the years to come. It is by now the second largest renewable energy source after hydropower (IEA, 2019b). According to the 15th Global Wind Report by the Global Wind Energy Council (GWEC), the current global cumulative wind power capacity has reached about 651 Gigawatts (GW) (GWEC, 2020). Also, new installations of about 60.4 GW of power capacity were made in 2019, which corresponds to

an increase of 19 per cent compared to the new installations in the previous year and demonstrates the accelerated growth of the wind energy industry.

As per the GWEC in (GWEC, 2020), in terms of cumulative installations, the largest markets up to date are the People's Republic of China, the United States of America, Germany, India and Spain. In terms of new installations in 2019, the largest markets were the People's Republic of China, the United States of America, the United Kingdom, India and Spain. Accordingly, the regions with most investments on the wind energy industry in 2019 were Asia Pacific, Europe and North America, with 50.7 per cent, 25.5 per cent and 16.1 per cent of the global new installations respectively.

Wind energy sources have proven their potential to be a principal source of energy for a country. For example, in the case of Denmark, almost 50 per cent of the generated electricity in 2018 was provided by this industry (IEA, 2019a). Moreover, in the case of Germany, wind energy was the main energy source in 2019, surpassing any other type of energy sources, including lignite and hard coal (GWEC, 2020).

1.1.2. Offshore wind energy

According to the International Energy Agency (IEA), offshore wind energy stands as a latent pillar of the future world's energy supply, having the technical potential to supply more than the total energy consumed worldwide (IEA, 2019b). Fig. 1 presents an sketch of an Offshore Wind Turbine (OWT) supported by a monopile foundation. Its main parts are indicated, including foundation, substructure or transition piece, tower and rotor-nacelle assembly.

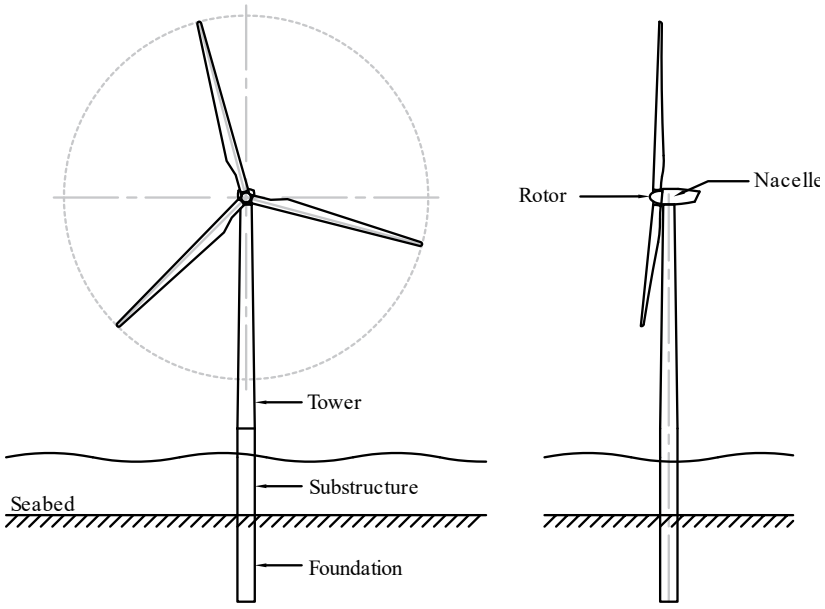

Fig. 1 Main parts of an offshore wind turbine.

Offshore locations provide benefits over onshore sites such as less turbulent winds with more consistent wind speed and direction, as well as the avoidance of land use and less aesthetic impact. Besides, the competitiveness of this industry increases, as the technology continuously expands with larger turbines and higher turbine ratings, and also as risks and uncertainty for investors reduce due to gained experiences in the past years (IRENA, 2020).

The offshore wind energy industry has been growing at a positive rate of 30 per cent each year from 2010 to 2018 (IEA, 2019a). This industry also logged record installations of 6.1 GW in 2019, achieving a total offshore wind power capacity of 29 GW, as reported in (GWEC, 2020). According to the latter report, the United Kingdom is by now the largest market in terms of cumulative offshore wind power capacity. In terms of new installations, the largest markets in 2019 were the People's Republic of China, the United Kingdom and Germany, with new installations of 2.3 GW, 1.8 GW and 1.1 GW respectively.

Technology improvements in the offshore wind energy field continuously lead to larger-capacity turbines by allowing the increase in their hub heights and rotor diameters. While in 2010, the average turbine rating was 3.0 MW, in 2018 this value increased to 5.5 MW (IRENA, 2019). Following the estimations from the IRENA (IRENA, 2019), offshore wind turbines with power ratings of 15 to 20 MW are expected to be commercially available in two decades (see Fig. 2, where RD stands for Rotor Diameter).

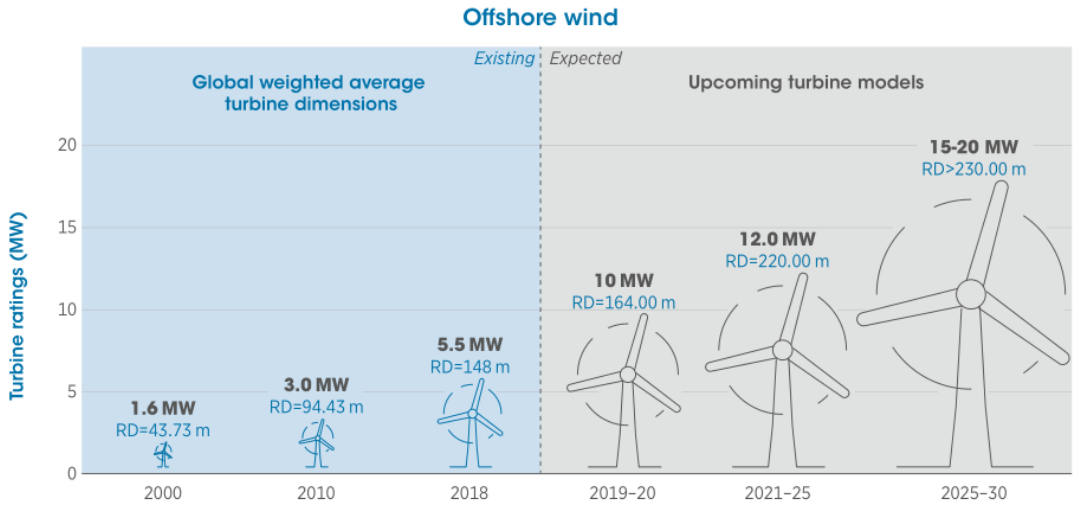

Fig. 2 Evolution of the average size of offshore wind turbines. Taken from (IRENA, 2019).

1.1.3. National framework: Colombia

Colombia's energy market depends primarily on hydropower and thermoelectric plants using fossil fuels such as natural gas, coal and diesel as energy sources. In 2019, the country's energy installations reached about 17.5 GW of national power capacity, which is distributed as 11.92 GW for hydropower (68.24 per cent of the total power capacity), 5.37 GW for fossil fuels (30.75 per cent) and less than 0.2 GW for biomass, solar and wind energy (1.01

per cent) (XM, 2019). Based on these statistics, Colombia's wind power installations in 2019 had a capacity of 18.42 MW, corresponding to the only wind park in the country connected to the National Interconnected System, namely the Jepírachi wind park located in the country's northern peninsula La Guajira.

Although hydropower stands as the main source of energy, when El Niño phenomenon occurs, severe droughts in the country cause it to depend on its second largest source of energy, which are fossil fuels. As stated by the Planning Office for Mining and Energy (UPME, for its acronym in Spanish), this dependence represents a periodic and increasing risk of scarcity and high energy prices for the country (UPME, 2015). The country's need for diversification of the energy matrix could be addressed by the inclusion of modern renewable energy sources, such as wind energy.

Many studies have shown the high technical potential for wind energy in the country. Specifically, the country's northern Caribbean coast and the departments of Santander, Norte de Santander, Risaralda, Tolima, Valle del Cauca, Huila and Boyacá have been addressed as potential locations for wind energy harnessing (UPME, 2015). Fig. 3 shows the annual distribution of the wind speed at a height of 80 m across the country as reported by the National Meteorological, Hydrological and Environmental Institute (IDEAM, for its acronym in Spanish). Wind speeds near 15 m/s are obtained in the country's northern Caribbean coast, which indicates a high potential for offshore wind energy harnessing. Some estimations suggest that the national energy demand could be fulfilled only by using half of the technical wind energy potential in the region La Guajira, which was evaluated as 18 GW (Pérez Bedoya & Osorio Osorio, 2002). Also, according to (Carvajal-Romo et al., 2019), the onshore and offshore wind energy potential in La Guajira could provide seven and eight times the national demand respectively. Added to this is the fact that there is a complementarity between wind- and hydropower energy in Colombia (Vergara et al., 2010).

In spite of its excellent potential in the country, wind energy remains as an unexploited energy resource. However, recent progress in the inclusion of non-conventional renewable energy sources have been seen in the last couple of years. In 2014, Law 1715 was released aiming to promote the development and use of non-conventional energy sources, mainly those of a renewable nature. Moreover, 23 new wind energy projects were registered in 2019 in the UPME system which are either under pre-feasibility or feasibility studies (UPME, 2020). Also in 2019, the country launched auctions, as a market-based mechanism to support the development of the renewable energy market. Resulting from this, in October 2019, 15-year Power Purchase Agreement deals were awarded to seven wind power projects, which are expected to provide 1.17 GW of wind power in La Guajira by 2022 (GWEC, 2020). For all that, Colombia has been positioned as a potential powerful wind market in Latin America (GWEC, 2020).

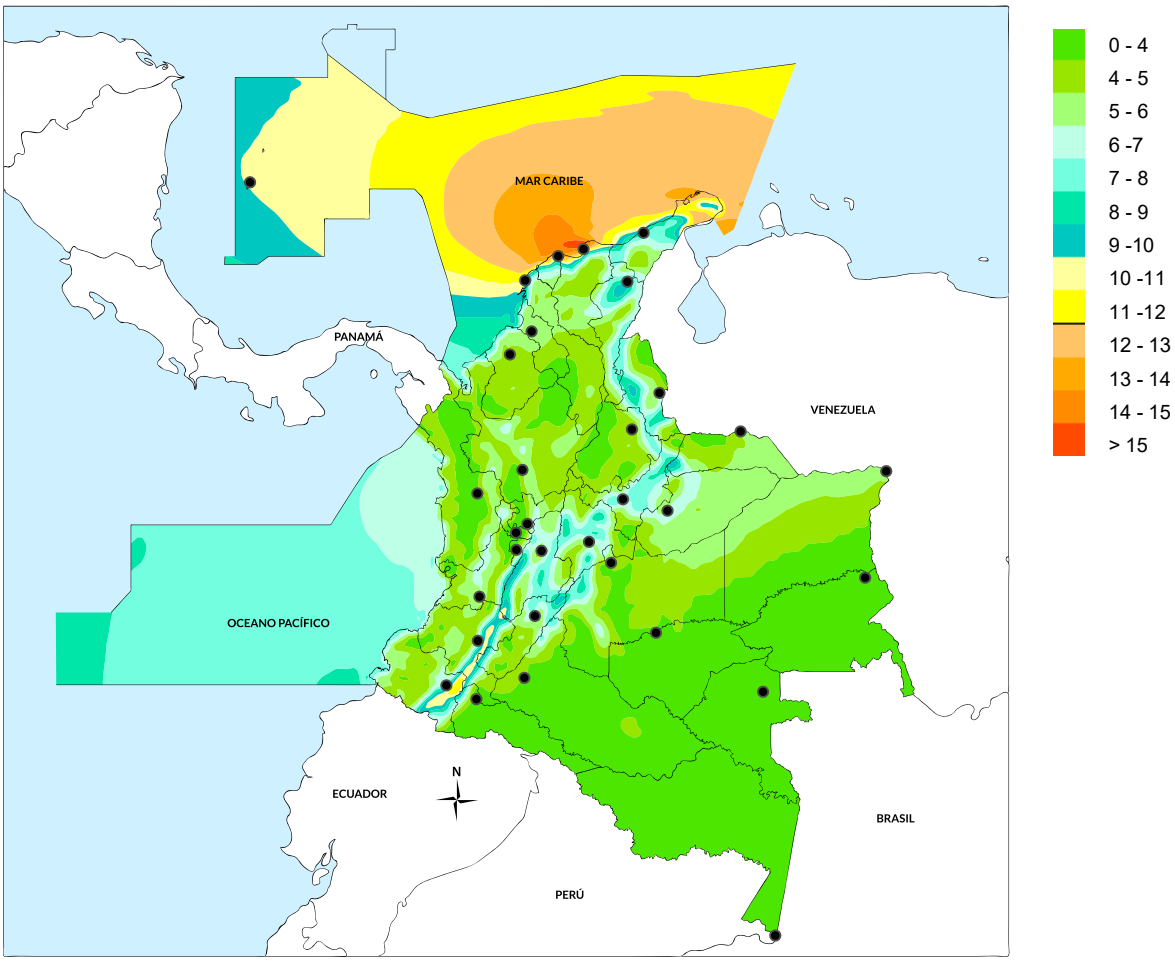

Fig. 3 Distribution of the wind speed in m/s at a height of 80 m in Colombia. Modified image. Taken from (IDEAM, 2015).

1.1.4. Foundations for offshore wind turbines

There are several foundation concepts for offshore wind turbines, such as gravity based, monopile, suction bucket, jacket and tripod foundations, as shown in Fig. 4. Large environmental lateral loads of cyclic nature, as well as large gravitational loads, must be resisted by the chosen foundation. The most popular foundation concept are monopile foundations, mostly because of its relatively low-cost and ease of installation. A monopile foundation consists of an open-ended pipe pile made of steel with a large diameter of several meters. These foundations are installed into the seabed by driving, jacking or vibrating installation methods. In 2019, monopiles covered 81 per cent of the installed foundations for offshore wind turbines in Europe, corresponding to 4258 units, followed by jacket foundations with 8.9 per cent (WindEurope, 2020).

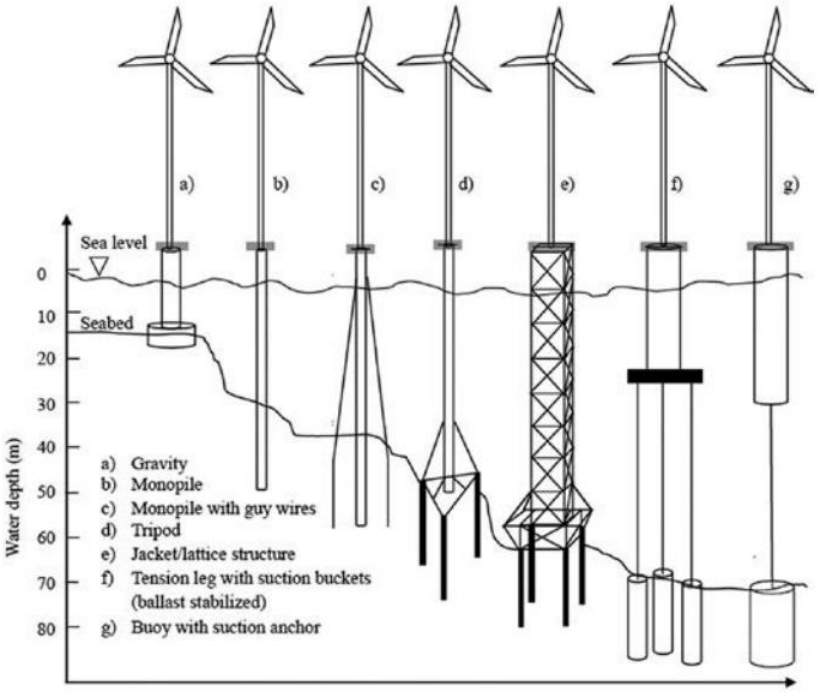

Fig. 4 Foundation concepts for offshore wind turbines. Taken from (Arshad & O'Kelly, 2016).

Monopile foundations are suitable for shallow to intermediate water depths of less than 50 m (IEA, 2019a). The typical outer diameter D of monopiles ranges between 3 m and 8 m. However, diameters up to 10 m are being considered in the industry, termed as 'XL monopiles'. Monopiles usually have embedment lengths L between 20 m and 40 m, keeping an embedment length-to-diameter ratio (L/D) of less than 10.

As long as larger turbines are developed, loading demands on foundations will increase and consequently larger foundations will be needed to support them. The analysis of monopiles with larger diameters is under current state of research. The proper analysis and design optimization of these structures is crucial for the feasibility of future projects, considering that the cost of foundations corresponds to about 25 per cent of the total cost of an offshore wind project (IEA, 2019a).

1.1.5. General considerations on the design of monopiles in sands

A brief overview of several factors considered in the analysis and design of monopiles founded in sands are presented below.

1.1.5.1. Loading conditions

The analysis and design of monopiles for offshore wind turbines is a multidisciplinary task, which considers the site-specific geotechnical conditions as well as the ocean-environmental loading conditions. Offshore wind turbines are subjected to environmental loads generated

by the action of wind, ocean waves, water currents and mean sea level variations due to tides and swell, see Fig. 5. Ideally, these loads are transmitted to the monopile as equivalent horizontal forces and bending moments at the pile head, along with the static axial load due to the self-weight of the superstructure. The lateral environmental loads on monopiles have a cyclic nature with varying direction, amplitude and frequency.

For monopile foundations, lateral loads are more significant in magnitude than vertical loads. Therefore, the analysis of monopile foundations under lateral loading is the major concern (Arshad & O'Kelly, 2016). Often, the loading conditions on monopiles are simplified as unidirectional monotonic or quasi-static cyclic loading composed by several load parcels with constant amplitude. However, considering the complex nature of the loading conditions, several topics are still open for investigation, such as the evaluation of multi-amplitude cyclic loading (Abadie et al., 2015; Wang & Larsen, 2019), multi-directional lateral loading (Sheil & McCabe, 2017; Staubach & Wichtmann, 2020), combined axial and lateral loading (Lu & Zhang, 2020), among others.

Monopiles must also withstand dynamic lateral excitations caused by the vibrations of the superstructure. The most relevant excitations for design are related to mass imbalances in the blades and the so-called blade shadowing effect, which is caused by the blades passing the tower. The first has a frequency equal to the rotor revolution frequency (termed as $1P$) and the latter has a frequency equal to thrice the rotor revolution frequency (termed as $3P$) (Arany et al., 2017).

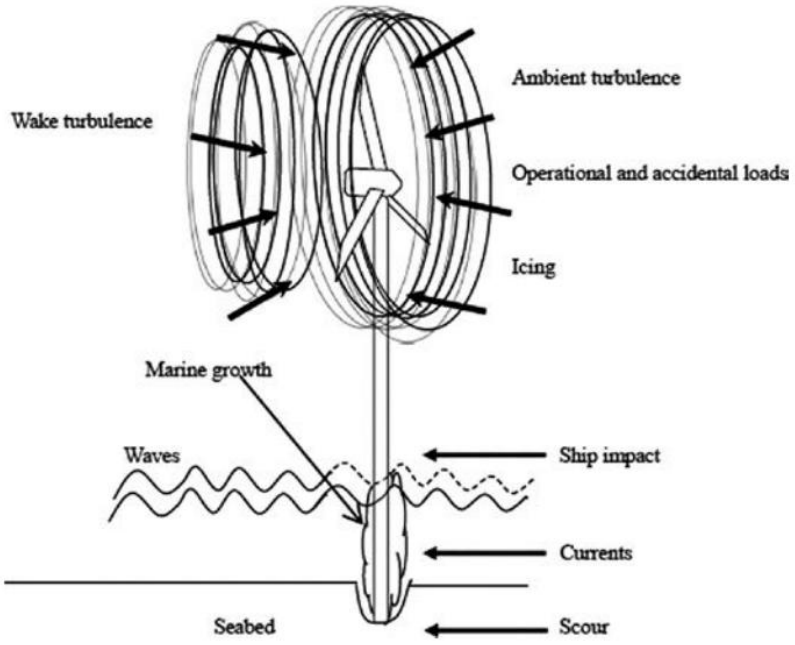

Fig. 5 Loading conditions on an offshore wind turbine. Taken from (Arshad & O'Kelly, 2016).

1.1.5.2. Geotechnical design considerations

According to current design standards, such as the Det Norske Veritas - Germanischer Lloyd Group (DNV-GL-AS, 2016) and the American Petroleum Institute (API, 2014a) standards, the geotechnical design of monopiles in sands must be checked with respect to two limit states, namely, the Ultimate Limit State (ULS) and the Serviceability Limit State (SLS). The design is usually controlled by the SLS rather than the ULS.

For the design in the ULS, monopiles must resist the action of lateral and axial loading under extreme loading conditions. According to the DNV-GL standards (DNV-GL-AS, 2016), two requirements shall be met. First, the theoretical ultimate pile resistance must be compared to the design loads. Second, the pile displacements and rotations at the pile head under extreme lateral loading conditions must not reach excessive values that can be considered as a failure state.

For the design in the SLS, the permanent pile displacements and rotations at the pile head must be under some defined deformation limit to ensure adequate turbine performance. Special attention must be given to the behavior under long-term cyclic loading. The DNV-GL standards (DNV-GL-AS, 2016) recommend to set $0.5°$ as the maximum allowable accumulated rotation at the pile head, from which $0.25°$ account for possible pile rotations caused during the installation of the monopile and $0.25°$ account for the permanent rotation due to the lateral loading.

1.1.5.3.Dynamic design considerations

The analysis of the dynamic behavior of monopiles regarding its small-strain stiffness, natural frequency and damping is also a relevant topic, specially for the design of the entire OWT structure. The natural frequency of the OWT and foundation system f_0 should be carefully estimated in order to avoid possible resonance phenomena with the excitation frequencies. In practice, this resonance avoidance criterion is accomplished by a "soft-stiff" design, in which f_0 is greater than the rotor frequency $1P$ and lower than the blade passing frequency $3P$, see Fig. 6. The DNV-GL standards (DNV-GL-AS, 2016) recommend to satisfy the conditions $1P/f_0 \leq 0.95$ and $3P/f_0 \geq 1.05$. The $1P$ frequency band usually lies between 0.17 Hz and 0.33 Hz, while the $3P$ frequency band usually lies between 0.5 Hz and 1.0 Hz (Arshad & O'Kelly, 2016).

The natural frequency f_0 is influenced by the soil-structure interaction. For its proper estimation, it is necessary to calculate the soil-monopile dynamic stiffness under small-strain amplitudes, which strongly depends on the soil behavior. This task is rather complicated since several topics must be considered, such as the effect of long term cyclic loading conditions on the soil stiffness, soil dissipative phenomena (damping), hydro-mechanical coupling under cyclic loading conditions, among others. Some studies have found that the measured natural frequencies of OWTs are higher than the previously calculated design values, which

may be related to an underestimation of the pile-soil stiffness (Damgaard et al., 2014; D. Kallehave et al., 2012), and may result in waste of pile material and more fatigue damage accumulation (Versteijlen et al., 2014). This discrepancy and the assessment of the different factors affecting the soil-structure interaction is still a research topic unresolved.

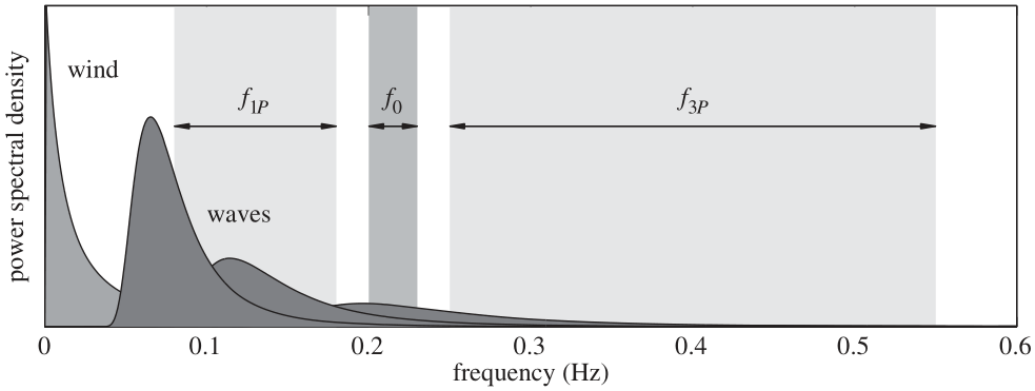

Fig. 6 Dynamic design criteria for offshore wind turbines. Taken from (Dan Kallehave et al., 2015).

1.1.5.4. Main issues of current design approaches

The geotechnical analysis approach for OWT monopiles was developed from the semi-empirical approach and design criteria already developed for piles from the offshore oil and gas industry. In comparison with the latter, monopile foundations present larger diameters as well as smaller length-to-diameter ratios. Therefore, the extrapolation of such criteria to OWT monopiles has been widely questioned in the literature, mainly because of their larger size and more significant lateral cyclic loads (Westermann et al., 2014b; Choo & Kim, 2016; Byrne et al., 2017; Martin Achmus et al., 2019).

As for the monotonic response, the conventional design method for monopiles in sands, i.e. the p-y method by API (API, 2014a), was developed for flexible slender piles with small diameters (Cox et al., 1974; Murchison & O'Neill, 1984). In contrast, monopiles are likely to exhibit a rigid or semi-rigid behavior with a combination of translational and rotational motion. Resulting from this discrepancy, the applicability of some aspects of the conventional p-y method as the distributions of the initial soil-stiffness and the ultimate soil resistance has been questioned in the literature (M. Achmus et al., 2007; Bouzid, 2018; Choo & Kim, 2016; D. Kallehave et al., 2012; W. Li et al., 2017; Sørensen et al., 2010; Wiemann et al., 2004). Furthermore, rigid or semi-rigid pile motion are related to additional soil reactions, different from the lateral soil reaction p already considered in the p-y method (Byrne et al., 2017; W. Li et al., 2017; Burd et al., 2019). Despite their relevance on the analysis of monopiles, there is still no consensus on how to evaluate these types of additional reactions in engineering practice for different types of soils.

As for the cyclic response, there is a lack of guidance in the design standards on how to assess the accumulated response of monopiles due to long-term cyclic loading (Ma et al., 2017). The methods from the oil and gas offshore industry, as the one by API (API, 2014a), are not suitable, since they are based on the results from tests on small diameter piles under a relatively small number of load cycles (Cox et al., 1974). Moreover, these methods do not consider some factors affecting the accumulated deflection, such as the number of load cycles, soil density and the loading amplitude, already confirmed by some authors (Staubach & Wichtmann, 2020; Westermann et al., 2014b). These and other limitations motivate to conduct more investigation on new methods providing accurate estimations to overcome the mentioned issues.

1.2. Research justification and purpose of the research project

As a novel and rather immature technology, offshore wind engineering is still under continuous development in many fields. Particularly, the design of monopile foundations for offshore wind turbines faces several challenges. Probably, one of the most important issues is the lack of applicability of the design methods adopted from the offshore oil and gas industry. Besides, as larger turbine sizes are being proposed in the industry, larger foundations will be needed. Consequently, the dimensions of monopiles may fall continuously further from the range of pile geometries already studied in the field of offshore geotechnical engineering.

In order to ensure a reliable design for OWT monopiles, the need is identified to study new approaches to the analysis of monopile foundations taking into account their associated range of pile geometries and loading conditions. Furthermore, considering that foundations represent a significant part of the budget of a wind energy project, optimizing the pile geometry through improved design methods is relevant to the feasibility of future projects.

In light of this, the current research project focuses on the application of numerical methods to improve the analysis and design of monopile foundations for OWTs under monotonic and long-term cyclic loading conditions. To begin, the study focuses on three dimensional (3D) Finite Element (FE) modelling of these structures. This modelling approach offers several benefits on the analysis of monopile foundations. First, it considers the non-linearity of the soil response as well as its volumetric behavior. With the use of advanced constitutive laws to model the soil behavior, accurate predictions of the whole monopile-soil system are expected. Second, the study of complex soil-structure interactions, such as the one between the monopile and supporting soil, is usually accomplished through 3D numerical techniques such as FE modelling. Third, it is a relatively low-cost technique for analyzing varying geometries, as well as different loading and soil conditions. Thus, this work attempts to offer an insight into the complex monopile response using 3D FE modelling, and it is additionally offered as an example of the use of 3D FE modelling for offshore geotechnical applications. In addition, although FE modelling is a very capable tool, it can also be very time-consuming

for design. As consequence, this research project also deals with one-dimensional (1D) modelling of monopiles using the Beam on a Non-Linear Winkler (BNWF) approach. The main idea is to provide a simplified methodology to analyze monopiles, which corresponds to the development of a novel 1D p-y model considering the results from the performed 3D FE simulations.

1.3. Research objectives

1.3.1. General objective

To develop a novel p-y model for offshore monopiles for wind turbines founded on granular soils under monotonic and cyclic loading.

1.3.2. Specific objectives

i. To compile and analyze current modelling and design approaches for laterally loaded monopiles.
ii. To develop 3D FE models for the simulation of laterally loaded monopiles incorporating advanced soil constitutive models.
iii. To analyze the performance of the soil-monopile system under monotonic conditions considering variations of pile geometry, soil conditions and loading cases.
iv. To provide possible modifications on current standards in order to improve the modelling and design of monopiles under static loading conditions and long-term cyclic loading conditions.

1.4. Research structure and methodology

The contents of this thesis have been organized into the following chapters:

In Chapter 1, the project framework is presented along with the research justification, purpose, objectives and structure. The project framework covers topics such as the wind energy market at a global and national scale, along with general information about offshore monopile foundations and relevant issues concerning their analysis and design.

In Chapter 2, a review of the literature on laterally loaded monopiles in sands is provided. The conventional analysis of a laterally loaded monopile is outlined. For this, the p-y method is carefully explained. The most known design standards and their limitations are also presented. Then, an overview of state-of-the-art research works on laterally loaded monopiles is provided.

In Chapter 3, the soil constitutive modelling approach adopted in the present study is addressed. First, the basics of hypoplastic modelling of soils are explained. Then, the chosen soil constitutive models incorporated in the FE models are introduced, namely, the hypoplastic model for sands by von Wolffersdorff (von Wolffersdorff, 1996) and the

Intergranular Strain (IS) extension for hypoplastic models by Niemunis and Herle (Niemunis & Herle, 1997).

In Chapter 4, a comprehensive parametric numerical study of monopiles under static lateral loading conditions using 3D FE simulations is presented. Variations of pile geometry, loading cases and soil materials are accounted for. The model's geometry, mesh generation, simulation steps, materials, applied loads and soil-structure interaction configuration are described. The results are presented and discussed.

In Chapter 5, a simplified 1D model for large diameter monopiles in sands under static- and long-term cyclic lateral loading conditions is proposed. The model is calibrated using the results from the parametric numerical study from Chapter 4 and other FE simulations results found in the literature. The capabilities of the model are evaluated by comparing the results of the proposed 1D model with experimental field and centrifuge tests.

In Chapter 6, a summary of the conclusions from previous chapters are presented.

Chapter 2: Literature Review on laterally loaded monopiles

2.1. Conventional p-y analysis

2.1.1. p-y method and BNWF approach

The Beam on a Non-linear Winkler Foundation approach (BNWF) is frequently employed on engineering design for the analysis of laterally loaded monopiles and has been recommended in several design guidelines such as (API, 2014a; DNV-GL-AS, 2016). In this method, also known as the p-y method, the monopile is simplified as an elastic Euler-Bernoulli beam supported by uncoupled springs with non-linear depth-dependent elastic behavior, which represent the lateral soil reaction. The spring stiffness is given by the secant stiffness of the so-called p-y curves, which relate the lateral soil reaction p with the pile horizontal displacement y at a given depth, see Fig. 7.c.

The lateral soil reaction p can be understood as the result from the integration around the pile perimeter of the lateral components of the mobilized radial stresses acting on the pile. When a pile is unloaded, the distribution of radial stresses around the pile is ideally uniform, as shown in Fig. 7.b, and there is no lateral soil reaction. Once the monopile is laterally loaded and deflects, it experiences an increase of the radial stresses acting on the pile which results in the lateral soil reaction p.

The basic principles of the p-y method were developed by Reese and Matlock (Lymon C Reese & Matlock, 1956) and McClelland and Focht (McClelland & Focht, 1956). These works were motivated by the expansion of the offshore oil and gas industry in the 1950s. Later, Cox et al. (Cox et al., 1974) presented the results from a series of tests on full-scale fully instrumented piles in medium dense sand at Mustang Island, Texas. These tests became the basis for the early formulations of the p-y method in the following years.

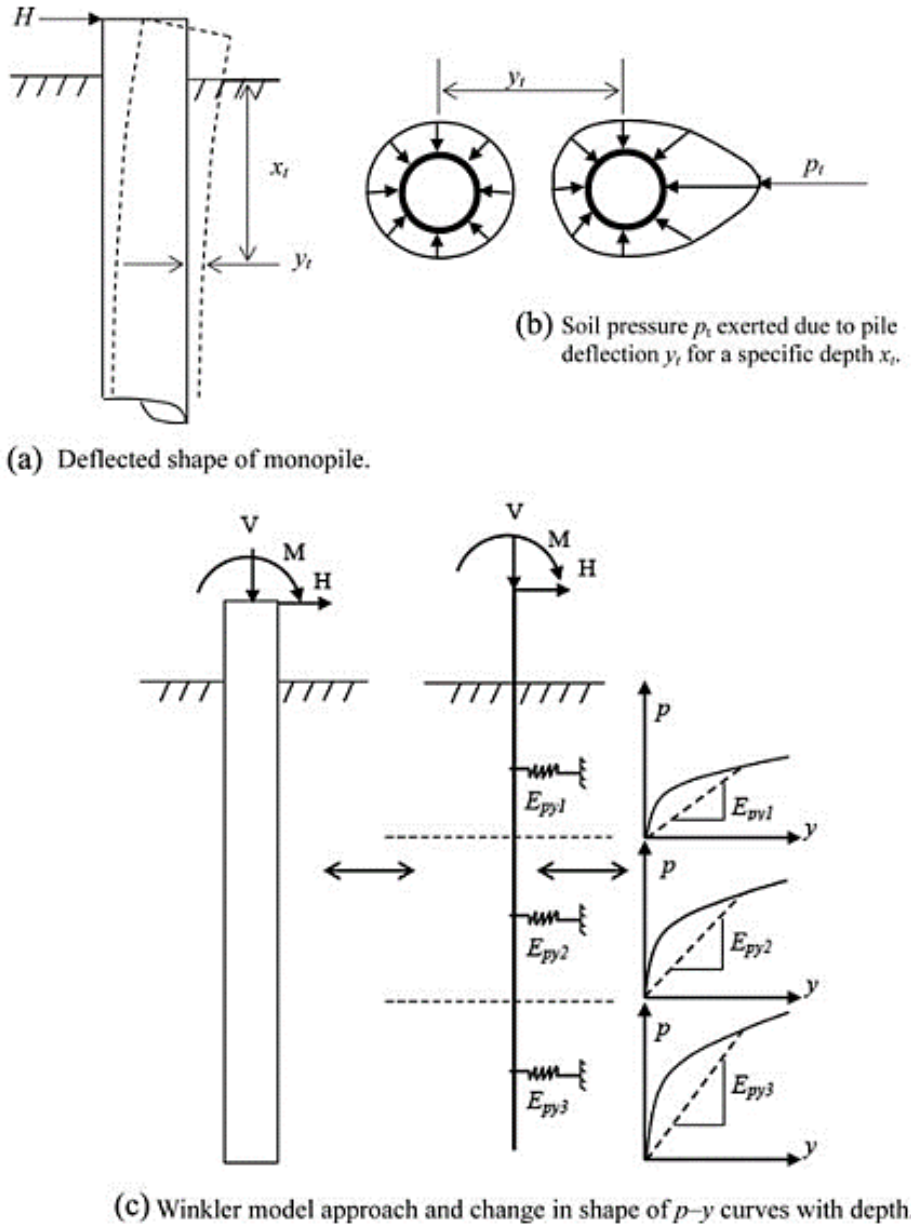

(a) Deflected shape of monopile.

(b) Soil pressure p_t exerted due to pile deflection y_t for a specific depth x_t.

(c) Winkler model approach and change in shape of p–y curves with depth.

Fig. 7 Sketch of the conventional BNWF approach for laterally loaded piles. Taken from (Arshad & O'Kelly, 2016).

The tests by Cox et al. (Cox et al., 1974) were conducted on two identical slender pipe piles made of steel with a diameter of 0.61 m and a length-to-diameter ratio of 34.4. Two static and five cyclic tests with less than 100 loading cycles were conducted. Based on those results, Reese et al. (Lymon C. Reese et al., 1974) presented the first formulation for p-y curves in sands. This is a semi-empirical formulation in which the p-y curves consist of four segments assembled together, namely an initial straight line to define the initial subgrade reaction modulus E_{py0}, a parabolic function, another straight line and a horizontal upper limit, termed as the ultimate soil resistance p_u. The latter was analytically obtained by Reese

et al. (Lymon C. Reese et al., 1974) assuming a wedge type failure mechanism at the top of the pile and a flow-around failure mechanism at greater depths. An empirical factor was introduced in the formulation of p_u to match the results from the field tests. Later, Murchison and O'Neill (Murchison & O'Neill, 1984) suggested a simplified version of the formulation by Reese et al. (Lymon C. Reese et al., 1974) which displays a tangent hyperbolic form for the p-y curve and introduces a simplified relationship for p_u. This relationship was validated against a relatively large database of full-scale laterally loaded pile tests and it was later adopted by design codes.

2.1.2. p-y curves

Nowadays, p-y curves are available in engineering practice from different types of sources, such as in-situ testing on instrumented piles, proposed empirical and analytical formulations in the literature and site-specific advanced numerical simulations. Regarding the empirical and analytical formulations, several p-y curves have been proposed for very specific types of soils, pile geometries and loading conditions. These curves usually depend on the pile geometry and on some measure of the soil strength, such as soil properties from laboratory testing or results from CPT field testing. Probably, the most employed curves for sands are the ones recommended by the API guidelines (API, 2014a), which are a modified version of the original p-y curves proposed by Reese et al. (Lymon C. Reese et al., 1974).

A typical p-y curve is shown in Fig. 8. p-y curves are usually described by two components, namely, the ultimate soil resistance p_u and the initial reaction modulus E_{py0} (or E_{py}^{*} as in Fig. 8). A brief outline is given below for each component.

i. Ultimate soil resistance, p_u:
   It corresponds to the maximum value of the lateral soil reaction. After p_u is reached, no additional lateral resistance can be gained. Instead, depending on the p-y formulation, either the lateral resistance can stay constant for increasing displacements or it can display a softening behavior.

ii. Initial reaction modulus, E_{py0}:
   It is the initial value of the subgrade reaction modulus, E_{py}. The latter corresponds to the slope of the secant of the p-y curve at a certain point, i.e. $E_{py} = dp/dy$. Many authors argue that the initial reaction modulus can not be understood as a soil property, since it is instead a parameter resulting from the interaction between soil and foundation. The value E_{py0} is of great importance for the dynamic assessment of the monopile.

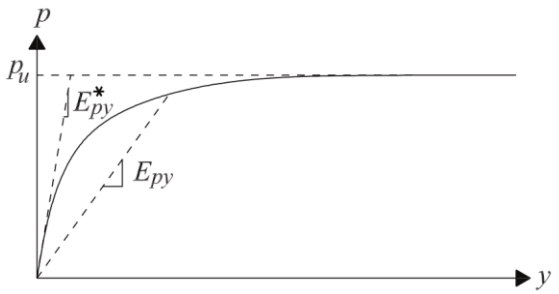

Fig. 8 Sketch of the components of a typical p-y curve. Taken from (Brødbæk et al., 2009).

2.1.3. Governing beam-column differential equation

The p-y method requires the solution of the governing fourth-order differential equation for a beam-column supported by an elastic foundation. Its derivation was given by Hetenyi (Hetenyi, 1946) and is hereafter described. It considers an elastic pile with bending stiffness EI under the action of an axial compressive force N and lateral horizontal loading applied at the top. An infinitely small element of the pile with length dx is examined, as shown in Fig. 9. The element is subjected to a pair of vertical compressive forces N, the shear forces V_v and $(V_v + dV_v)$, the moments M and $(M + dM)$ and the distributed soil reaction p. The equilibrium of moments about point O gives:

$$(M + dM) - M + N\,dy - (V_v + dV_v)dx - p\,dx\frac{dx}{2} = 0 \tag{1}$$

If the second-order terms are neglected, the latter equation results in:

$$(M + dM) - M + N\,dy - V_v\,dx = 0 \tag{2}$$

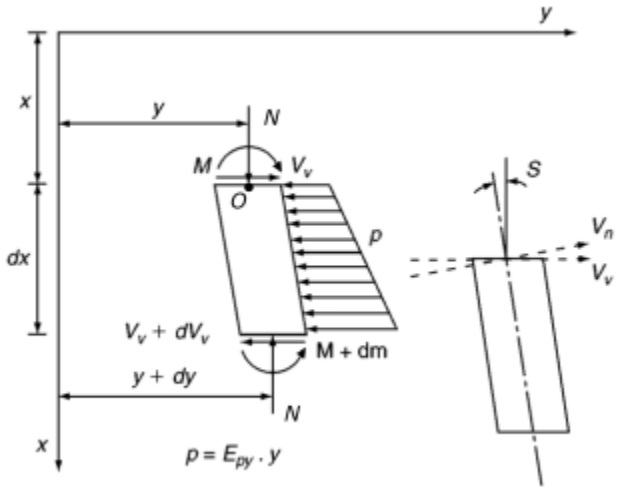

Fig. 9 Forces acting on an infinitively small element of the pile. Modified image. Taken from (L. C. Reese & Van Impe, 2011).

Simplification and double differentiation with respect to x of the last equation gives:

$$\frac{dM}{dx} + N\frac{dy}{dx} - V_v = 0 \tag{3}$$

$$\frac{d^2M}{dx^2} + N\frac{d^2y}{dx^2} - \frac{dV_v}{dx} = 0 \tag{4}$$

Substitution of the identities $dV_v/dx = p = -E_{py}y$ and $d^2M/dx^2 = EI\, d^4y/dx^4$ in the last equation gives the governing differential equation for the bending of the pile:

$$EI\frac{d^4y}{dx^4} + N\frac{d^2y}{dx^2} + E_{py}\, y = 0 \tag{5}$$

where y is the pile displacement at a given depth z and $E_{py} = dp/dy$ is the spring stiffness representing the soil reaction.

2.1.4. Solution of the beam-column differential equation

Different types of solutions for the governing differential beam-column equation are available in the literature, including simplified closed-form solutions and numerical approaches. This section refers to the solution of the governing differential equation by numerical iteration using Finite Difference calculations. For this, the pile is discretized into n segments which results in $n + 1$ nodes. The pile segments have a length of $h = L/n$, where L is the embedment length of the pile (see Fig. 10). Equation (5) shall be applied on each node along the pile. To do so, the derivates are evaluated through Finite Difference equations as:

$$\left.\frac{d^2y}{dx^2}\right|_{x=i} = \frac{y_{i-1} - 2y_i + y_{i+1}}{h^2} \tag{6}$$

$$\left.\frac{d^4y}{dx^4}\right|_{x=i} = \frac{y_{i-2} - 4y_{i-1} + 6y_i - 4y_{i+1} + y_{i+2}}{h^4} \tag{7}$$

Therefore, the finite difference form of Equation (5) for a given node at $x = i$ reads:

$$y_{i-2}\, EI + y_{i-1}(-4\, EI + N\, h^2) + y_i\left(6\, EI - 2\, N\, h^2 + E_{py_i}\, h^4\right) + y_{i+1}\,(-4\, EI + Nh^2) + y_{i+2}\, EI = 0 \tag{8}$$

Note that the last equation requires the pile displacements of the node at $x = i$ (y_i) and the displacements of the four adjacent nodes ($y_{i-2}, y_{i-1}, y_{i+1}$ and y_{i+2}). To solve the last equation for the nodes at the pile head and pile base, two fictional nodes below the pile base and two above the pile head needs to be considered, see Fig. 10.

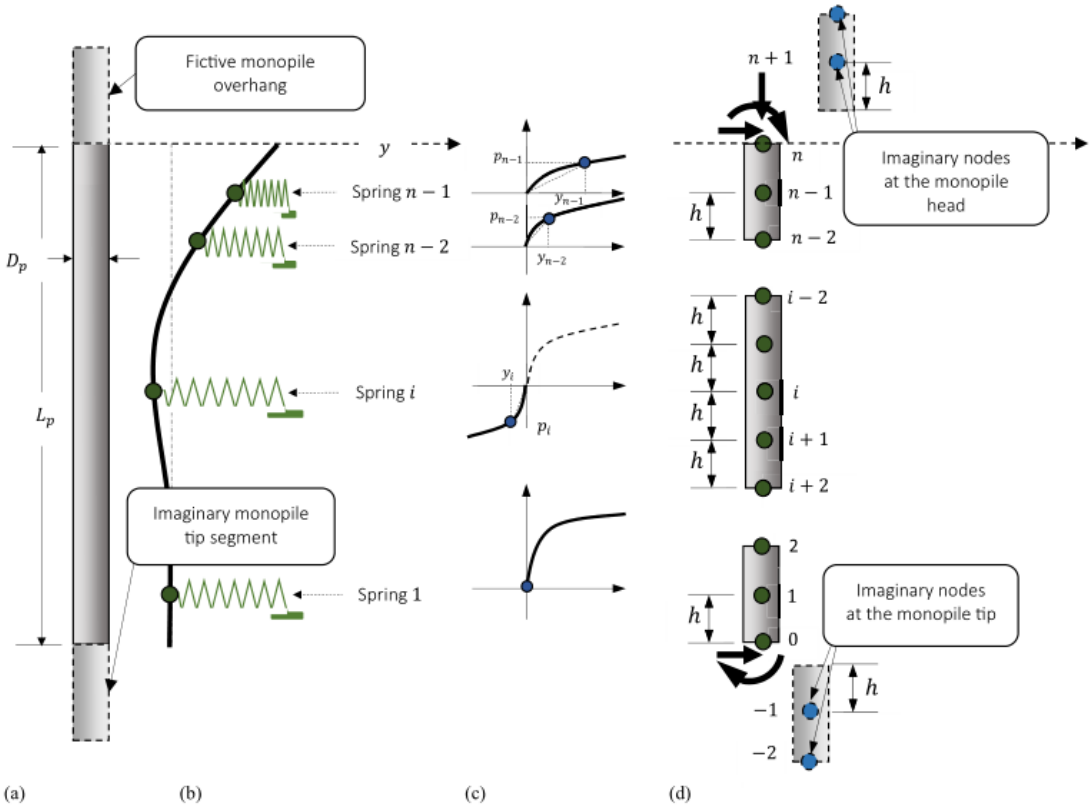

Fig. 10 Discretized pile for the Finite Difference calculations. Taken from (Bouzid, 2018).

A number of $n+1$ equations can be written of the form of Equation (8) for each node along the pile. In consequence, the set of $n+1$ equations results with $n+5$ unknowns, corresponding to the displacements of all fictional and non-fictional nodes along the pile. Therefore, four boundary conditions are needed to complete the set of equations. For a free-head pile, the following equations are commonly employed:

i. Horizontal load H applied at the pile head

$$\frac{EI}{2h^3}(y_{n-2} - 2y_{n-1} + 2y_{n+1} - y_{n+2}) + \frac{N}{2h}(y_{n-1} - y_{n+1}) = H \tag{9}$$

ii. Moment M applied at the pile head

$$\frac{EI}{h^2}(y_{n-1} - 2y_n + y_{n+1}) = M \tag{10}$$

iii. Base shear force S_B

$$\frac{EI}{2h^3}(y_{-2} - 2y_{-1} + 2y_1 - y_2) + \frac{N}{2h}(y_{-1} - y_1) = S_B \tag{11}$$

iv. Base moment M_B

$$\frac{EI}{h^2}(y_{-1} - 2y_0 + y_1) = M_B \tag{12}$$

For long-slender piles, the base shear force and base moment (S_B and M_B) are usually neglected. However, for rigid piles S_B and M_B could have a significant effect on the pile response. The above set of equations is solved by matrix methods to find the horizontal displacements along the pile. Iterative calculations are required when the subgrade reaction modulus E_{py} is obtained applying the p-y method, on account of the dependence of the value E_{py} on the mobilized displacement y at a given depth.

2.2. Design guidelines

2.2.1. List of design guidelines

A list of some design guidelines used for the analysis and design of offshore monopile foundations is presented as follows:

i. DNVGL-ST-0126: Support structures for wind turbines (DNV-GL-AS, 2016).

ii. API RP 2A-WSD: Planning, Designing, and Constructing Fixed Offshore Platforms - Working Stress Design (API, 2014a).

iii. API RP 2GEO: Geotechnical and Foundation Design Considerations (API, 2014b).

iv. ISO 19902:2007/AMD 1:2013: Petroleum and natural gas industries - Fixed steel offshore structures (ISO, 2013).

v. ISO 19901-4:2016: Petroleum and natural gas industries - Specific requirements for offshore structures - Part 4: Geotechnical and foundation design considerations (ISO, 2016).

The standards by the American Petroleum Institute (API, 2014a) and Det Norske Veritas - Germanischer Lloyd Group (DNV-GL-AS, 2016) are the most popular guidelines for the design of monopiles. Both standards adopt the same p-y method (hereafter referred to as the API/DNV-GL-AS method) which was originally developed for long-slender piles, as described in the previous sections. Considering this issue, the DNV-GL-AS standards also suggest to validate the monopile design with more advanced numerical analyses, such as FE modelling.

2.2.2. API/DNV-GL-AS p-y method for sands

The p-y formulation presented by API (API, 2014a) and adopted by DNV-GL-AS (DNV-GL-AS, 2016) refers to a hyperbolic tangent curve. The lateral soil reaction per unit length p [kN/m] is given by:

$$p = A\, p_u \tanh\left(\frac{kz}{A\, p_u} y\right) \tag{13}$$

where A is a factor that accounts for the loading conditions, p_u is the ultimate soil resistance, k is the initial modulus of subgrade reaction, depicted on Fig. 11, and z is the depth. Factor A is computed as:

$$A = \begin{cases} 0.9 & \text{cyclic loading} \\ 3.0 - 0.8\dfrac{z}{D} \geq 0.9 & \text{static loading} \end{cases} \tag{14}$$

where D is the external pile diameter. The ultimate soil resistance per unit length p_u [kN/m] is defined as:

$$p_u = \min\begin{cases} (C_1 z + C_2 D)\, \gamma' z \\ C_3 D \gamma' z \end{cases} \tag{15}$$

where C_1, C_2 and C_3 are factors depending on the friction angle of the soil and γ' is the effective unit weight of the soil. Factors C_1, C_2 and C_3 are shown in Fig. 11.

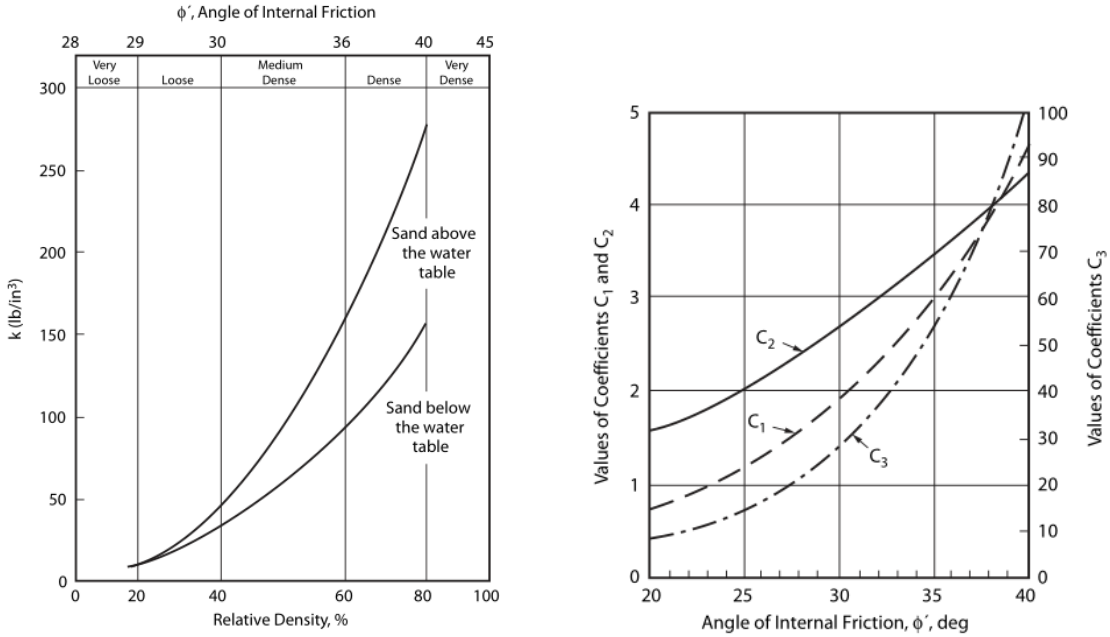

Fig. 11 Constants k, C_1, C_2 and C_3 used on the API/DNV-GL-AS p-y method for sands. Taken from (API, 2014a).

The initial reaction modulus E_{py0} according to this method is obtained from Equation (13) as:

$$E_{py0-API} = \left.\frac{dp}{dy}\right|_{y=0} = kz \tag{16}$$

Note that according to this method the initial reaction modulus increases linearly with depth and is independent of the pile geometry.

2.3. State-of-the-art research

Different geotechnical issues regarding the applicability of the conventional p-y analysis and current design guidelines for large diameter monopiles have been studied by many researchers through field testing, 1-g model testing, centrifuge model testing and numerical analyses (Westermann et al., 2014b; Choo & Kim, 2016; W. Li et al., 2017; Byrne et al., 2017; Martin Achmus et al., 2019). Topics such as load-deflection response of monopiles, modelling of the monopile-soil interface, fatigue analysis and accumulated response due to cyclic loading have been widely discussed. However, there is no consensus on appropriate design methodologies for these structures and further research is required. A discussion on some of these topics is given below.

2.3.1. Monotonic behavior

Some of the first research works on large diameter monopile foundations in sands evaluated the load-deflection response of monopiles through 3D FE simulations and compared their results with conventional methods (M. Achmus et al., 2007; Hearn & Edgers, 2010; Sørensen, 2012; Sørensen et al., 2010; Wiemann et al., 2004). Their simulations results showed that large diameter monopiles behaved as rigid or semi-rigid piles and that conventional methods, such as the API/DNV-GL-AS method, failed to reproduce the observed behavior. Wiemann et al. (Wiemann et al., 2004) concluded that the API/DNV-GL-AS method overestimates the initial subgrade reaction modulus E_{py0} at large depths for large diameter monopiles, which also implied overestimated values of the oedometric stiffness modulus of the soil. Therefore, a modification of the method was proposed in which E_{py0} has a non-linear distribution with depth and depends on the pile diameter D. Hearn and Edgers (Hearn & Edgers, 2010) suggested that the API/DNV-GL-AS method overestimates E_{py0} and p_u for large diameter monopiles, specially at large depths and for increasing soil densities. Sørensen et al. (Sørensen et al., 2010) also presented a modification of E_{py0} which depends on the pile diameter D and the friction angle of the soil φ, and has a non-linear distribution with depth. Similar modifications of E_{py0} were also proposed by Kallehave et al. (D. Kallehave et al., 2012). Furthermore, more specific aspects of the behavior of monopiles under lateral monotonic loading have been investigated through 3D FE

simulations (Ahmed & Hawlader, 2016; S. Li et al., 2019; Lu & Zhang, 2020). For instance, Li et al. (S. Li et al., 2019) evaluated the effect of the drainage conditions on the response of a monopile under monotonic loading. The effect was significant when large loads were considered but negligible at the load levels considered on the design of monopiles. Ahmed and Hawlader (Ahmed & Hawlader, 2016) performed a parametric numerical study to evaluate the load-carrying capacity of monopiles in dense sands. Load-moment capacity interaction diagrams were reported for the design of monopiles. Also, Lu and Zhang (Lu & Zhang, 2020) studied the effect of different combinations of lateral and vertical loads on the response of monopiles. They evaluated the change in soil stiffness due to different loading conditions and proposed a new p-y formulation.

Centrifuge tests on large diameter monopiles under monotonic loading such as (Choo & Kim, 2016; Dyson & Randolph, 2001) have been reported in the literature. Dyson and Randolph (Dyson & Randolph, 2001) applied an acceleration of $160g$ to a 13-mm-diameter model pile to represent an equivalent prototype pile with a diameter D of 2.08 m. The study considered the pile embedded in calcareous sand, evaluated different installation methods and loading rates, and proposed a p-y model based on the cone resistance q_c. Choo and Kim (Choo & Kim, 2016) conducted a series of centrifuge tests with 79.4-mm-diameter model piles of different materials at accelerations of $60g$ and $75g$. The tests were performed to represent equivalent prototype steel piles with a diameter D of 6.00 m. The study obtained experimental p-y curves and compared the results against the API/DNV-GL-AS method. According to their results, the API/DNV-GL-AS method overestimates the initial subgrade modulus E_{py0}, which also presents a non-linear distribution with depth. The effect of a rock bearing layer near the tip of the pile was also evaluated and a strong influence on the E_{py0} values on the adjacent layers was observed.

More recently, field testing research works on large diameter monopiles under monotonic loading have been conducted such as (Byrne et al., 2017; W. Li et al., 2017, p. 201). Li et al. (W. Li et al., 2017) conducted a series of monotonic field tests on reduced scale monopiles with $D = 0.34$ m and $L/D = 6.5$. The test piles were installed on a dense sand at the University College Dublin (UCD) geotechnical research site at Blessington, Ireland. In this study, measurements of the p-y curves along the pile and shear forces at the pile base were made. The measurements were compared to the API/DNV-GL-AS method and it was concluded that the latter overestimates the initial stiffness at large depths and underestimates the ultimate resistance at shallow depths. Additionally, the obtained shear values at the pile base were used to simulate the observed pile response using the p-y approach, proving its importance on a rigid pile response. Finally, to overcome the mentioned limitations, this study proposed some modifications of the API method, namely, the consideration of the base shear force, a power distribution of the initial subgrade modulus and some modifications on the p_u formulation. On a bigger scale, the joint industry PISA project (Burd et al., 2019; Byrne et al., 2017; McAdam et al., 2019; Murphy et al., 2018) conducted a series of medium-

scale field tests on monopiles in a dense marine sand at Dunkirk, France. Three different pile diameters were considered, namely $D = \{0.273, 0.762, 2.0\}$ m with length-to-diameters ratios ranging from $L/D = 3$ to 10. The test results were used to validate a 3D FE modelling technique, which was later used to develop a 1D analysis approach for monopiles. This approach considers the pile as a Timoshenko beam on a 1D FE framework. Additional soil reactions curves, apart from the lateral soil reaction p, were also considered i.e. distributed moment along the pile shaft and concentrated shear force and moment at the pile base. Resulting from this work, two different design techniques were proposed, namely the 'rule-based method' and the 'numerical based method'. The first uses parameterized reaction curves which were calibrated for an specific marine sand (Burd et al., 2019). The second requires a 3D FE calibration study to obtain the site specific reaction curves (Murphy et al., 2018). This project highlighted the need to account for additional soil reaction curves to model the behavior of monopiles. Validation of this method and its comparison with 3D FE simulations with sophisticated material models is under current study (Zachert & Wichtmann, 2020).

Fig. 12 Pile testing arrangements used in the PISA project. Taken from (Byrne et al., 2017).

2.3.2. Cyclic behavior

There is still limited understanding on many aspects regarding the response of monopiles under cyclic loading. One of the main topics that are still open for investigation is the assessment of the accumulated response of monopiles. The API/DNV-GL-AS method fails to properly predict the accumulated pile behavior since it does not account for important factors affecting the soil response under cyclic loading, such as the number of loading cycles, the material properties, the loading characteristics, among others. Different approaches are found in the literature to assess this issue. For instance, some authors have provided formulations which are commonly cataloged into soil resistance degradation (SRD) methods and pile deformation accumulation (PDA) methods. The SRD methods reduce the soil secant stiffness (on the p-y method) to account for the accumulated response (Dührkop, 2009; Lymon C. Reese et al., 1974), while the PDA methods calculate the accumulated response due to N cycles as a function of the groundline displacements of the monopile corresponding

to the first loading cycle. Two types of mathematic models are commonly considered within the PDA methods, namely the power function model (M. Hansen et al., 2013; Klinkvort & Hededal, 2013; Little & Briaud, 1988; Long & Vanneste, 1994; Peralta, 2010; Yang et al., 2018) and the logarithmic function model (Bienen et al., 2012; M. Hansen et al., 2013; Z. Li et al., 2010; Lin & Liao, 1999; Peralta, 2010; Verdure et al., 2003). These models have been proposed on the basis of limited experimental data and require further validation for their application with different monopile geometries and loading conditions (W. Li et al., 2015; Yang et al., 2018). As an alternative, new methodologies incorporating numerical simulations have been presented in the literature (M. Achmus et al., 2009; Sheil & McCabe, 2017). For example, (M. Achmus et al., 2009) proposed the Degradation Stiffness model (DSM) which evaluates the accumulated response of the soil based on a combination of a 3D FE simulation and the results from a series of drained cyclic triaxial tests. This model has been validated by other authors such as (Depina et al., 2015; Yang et al., 2018, 2018). Moreover, (Niemunis et al., 2005) proposed the High Cycle Accumulation (HCA) constitutive model for the soil which can be incorporated into 3D FE simulations of monopiles. The model explicitly considers the effects of the number of loading cycles, soil's density, mean stress, strain amplitude, stress ratio and load polarization. This model has been successfully incorporated in several FE simulations of large diameter monopiles (Staubach & Wichtmann, 2020; Westermann et al., 2014b; Wichtmann et al., 2008; Zachert & Wichtmann, 2020).

Chapter 3: Constitutive modelling of soil behavior

3.1. Hypoplasticity

Constitutive models are mathematical formulations that describe the stress-strain relationship of a particular material. In geomechanics, complex mechanisms, such as anelastic deformations, dependence on loading history, yield surfaces, dilatancy-contractancy and stress dependent stiffness, have to be considered to properly simulate the behavior of the soil. For this purpose, different types of constitutive models have been developed in the past decades, which may be catalogued into stress-based models and strain-based models. Stress-based models are developed from the well-known theory of elastoplasticity, in which strains are divided into elastic and plastic parts and a yield surface is defined in the stress space from which plastic strains are generated. Models families such as critical state models with single yield surface (Roscoe & Burland, 1968), bounding surface models (Dafalias, 1986; Dafalias & Herrmann, 1986), multisurface plasticity models (Mrŏz, 1967; Mrŏz et al., 1978), generalized plasticity models (Pastor et al., 1990), hyperplastic models (Collins & Houlsby, 1997; Houlsby & Puzrin, 2000) and subloading plasticity models (Hashiguchi, 1989; Hashiguchi & Chen, 1998) fall into this category. On the other hand, strain-based models are rather novel proposals, in which the concept of a yield condition in the stress field is dropped, and instead, the plastic mechanism is proposed based on strain space formulation. This category includes, brick type models (Ellison et al., 2012), hypoplastic models extended by intergranular strain (Niemunis & Herle, 1997; von Wolffersdorff, 1996), among others.

In this work, the hypoplastic model for sands proposed by von Wolffersdorff (von Wolffersdorff, 1996) and extended with the intergranular strain concept by Niemunis and Herle (Niemunis & Herle, 1997) has been adopted. The theory of hypoplasticity is one of the alternatives to elastoplasticity to describe the anelastic behavior of the soil. Hypoplasticity considers a single constitutive non-linear tensorial equation for the stress rate (i.e. increment

per time unit) which depends on a given strain rate and the current stress and void ratio states, and does not require a predefined yield surface or plastic potential surface, as in elastoplasticity. This formulation prevents the need to decompose the strain rate into elastic and plastic components, which allows to implement the same single equation for both loading and unloading. This is achieved by a generalized hypoplastic equation such as:

$$\dot{\mathbf{T}} = \mathbf{F}(\mathbf{T}, e, \mathbf{D}) \tag{17}$$

where $\dot{\mathbf{T}}$ is the stress rate tensor (in case of large deformations the jaumann stress rate is used), **F** is a tensorial function, **T** is the Cauchy's effective stress tensor, **D** is the stretching rate tensor and e is the void ratio.

3.2. Hypoplastic model for sands

The hypoplastic model by von Wolffersdorff (von Wolffersdorff, 1996) is one of the most popular hypoplastic models for granular materials. Under this formulation, the following hypoplastic constitutive equation was proposed:

$$\dot{\mathbf{T}} = \mathrm{L}\colon \mathbf{D} + f_d\, \mathbf{N}\, \|\mathbf{D}\| \tag{18}$$

where L is the fourth-order linear stiffness tensor, **N** is the second-order nonlinear stiffness tensor and f_d is a density factor ($0 < f_d < 1$). Tensors L and **N** are defined as:

$$\mathrm{L} = \frac{f_b f_e}{\hat{\mathbf{T}}\colon \hat{\mathbf{T}}} a^2 \left[\left(\frac{F}{a}\right)^2 \mathrm{I} + \hat{\mathbf{T}} \otimes \hat{\mathbf{T}}\right] = \frac{f_b f_e}{\mathbf{T}\colon \mathbf{T}}\, \hat{\mathrm{L}} \tag{19}$$

$$\mathbf{N} = \frac{f_b f_e}{\hat{\mathbf{T}}\colon \hat{\mathbf{T}}} a^2 \left(\frac{F}{a}\right) \left[\hat{\mathbf{T}} + \hat{\mathbf{T}}^*\right] = \frac{f_b f_e}{\mathbf{T}\colon \mathbf{T}}\, \hat{\mathbf{N}} \tag{20}$$

where $\hat{\mathbf{T}}$ and $\hat{\mathbf{T}}^*$ are the relative stress and its deviatoric part respectively, f_b and f_e are the barotropy and piknotropy factors, I is a fourth-order identity tensor and factors F and a are scalar factors.

The density factor f_d is computed as:

$$f_d = \left(\frac{e - e_d}{e_c - e_d}\right)^{\alpha} \tag{21}$$

where α is a material parameter, e is the void ratio and e_d and e_c are the densest and critical void ratios. In this model, the loosest, critical and densest void ratios (e_i, e_c and e_d) are defined according to the Bauer's equation (Bauer, 1992) as:

$$\frac{e_i}{e_{i0}} = \frac{e_c}{e_{c0}} = \frac{e_d}{e_{d0}} = \exp\left[-\left(\frac{-\mathrm{tr}[\mathbf{T}]}{h_s}\right)^{n_B}\right] \tag{22}$$

where h_s and n_B are material parameters, and the constants e_{i0}, e_{c0} and e_{d0} are the loosest, densest and critical void ratios for $\mathbf{T} = 0$.

The relative stress and its deviatoric part $\hat{\mathbf{T}}$ and $\hat{\mathbf{T}}^*$ are defined as:

$$\hat{\mathbf{T}} = \frac{\mathbf{T}}{\mathrm{tr}[\mathbf{T}]} \quad \text{and} \quad \hat{\mathbf{T}}^* = \frac{\mathbf{T}}{\mathrm{tr}[\mathbf{T}]} - \frac{1}{3}\mathbf{1} \tag{23}$$

where $\mathbf{1}$ is a second-order identity tensor.

The barotropy factor f_b adjusts the hypoplastic equation to the Bauer's equation under isotropic compression and reads:

$$f_b = \left(\frac{e_{i0}}{e_{c0}}\right)^{\beta} \frac{h_s}{n_B} \frac{1+e_i}{e_i} \left(\frac{-\mathrm{tr}[\mathbf{T}]}{h_s}\right)^{1-n_B} \left[3 + a^2 - a\sqrt{3}\left(\frac{e_{i0} - e_{d0}}{e_{c0} - e_{d0}}\right)^{\alpha}\right]^{-1} \tag{24}$$

The piknotropy factor f_e incorporates the influence of the void ratio in the material stiffness and reads:

$$f_e = \left(\frac{e_c}{e}\right)^{\beta} \tag{25}$$

The scalar factors F and a are used to align the yield and critical state conditions with the Matsouka-Nakai yield surface, which is controlled by the critical state friction angle φ_c. Factors F and a read:

$$F = \sqrt{\frac{1}{8}\tan^2(\psi) + \frac{2 - \tan^2(\psi)}{2 + \sqrt{2}\tan(\psi)\cos(3\theta)}} - \frac{1}{2\sqrt{2}}\tan(\psi) \tag{26}$$

$$a = \frac{\sqrt{3}(3 - \sin(\varphi_c))}{2\sqrt{2}\sin(\varphi_c)} \tag{27}$$

with

$$\tan(\psi) = \sqrt{3}\left\|\hat{\mathbf{T}}^*\right\| \quad \text{and} \quad \cos(3\theta) = -\sqrt{6}\frac{\mathrm{tr}[\hat{\mathbf{T}}^* \cdot \hat{\mathbf{T}}^* \cdot \hat{\mathbf{T}}^*]}{\left[\hat{\mathbf{T}}^* : \hat{\mathbf{T}}^*\right]^{3/2}} \tag{28}$$

In conclusion, the model requires the definition of eight material parameters, namely $\{\varphi_c, h_s, n_B, e_{d0}, e_{c0}, e_{i0}, \alpha, \beta\}$. The calibration process for these parameters is described in several works such as (Herle & Gudehus, 1999; Mašín, 2019).

3.3. Intergranular Strain concept

The hypoplastic model by von Wolffersdorff (von Wolffersdorff, 1996) successfully predicts the soil behavior in the medium and large strain range. However, for the small strain range and upon cyclic loading, the model requires a modification to incorporate the small-strain stiffness effects (i.e. high quasi-elastic soil stiffness in the small strain range) and to avoid excessive plastic accumulation during cyclic loading (i.e. ratcheting). For this, Niemunis and Herle (Niemunis & Herle, 1997) proposed the Intergranular Strain (IS) concept as an extension for hypoplastic constitutive models. This concept incorporates the idea that for very small strain amplitudes at the beginning of the loading phase, the soil deformation is not caused by the rearrangement of the grain skeleton but by the reversible deformation of an 'intergranular strain layer' and the elastic deformation of the grains. A maximum value of the intergranular strain is defined through a parameter of the constitutive model. Once the intergranular strain reaches this maximum value, the soil deformation is computed using a standard hypoplastic model. This is achieved by introducing an additional state variable, namely the intergranular strain tensor **h**, which in tensorial notation reads:

$$\dot{\mathbf{h}} = \begin{cases} \left(\mathrm{I} - \vec{\mathbf{h}} \otimes \vec{\mathbf{h}}\, \rho^{\beta_r}\right) : \mathbf{D} & \text{for } \vec{\mathbf{h}} : \mathbf{D} > 0 \\ \mathbf{D} & \text{for } \vec{\mathbf{h}} : \mathbf{D} \leq 0 \end{cases} \tag{29}$$

where $\vec{\mathbf{h}} = \mathbf{h}/\|\mathbf{h}\|$ is the direction of the intergranular strain, $\rho = \|\boldsymbol{h}\|/R$ corresponds to its normalized length and β_r and R are material parameters. Parameter β_r controls the intergranular strain evolution and the stiffness degradation curve. Parameter R controls the maximum value of the intergranular strain **h**.

To incorporate the intergranular strain concept, the following general constitutive equation was proposed:

$$\dot{\mathbf{T}} = \mathrm{M} : \mathbf{D} \tag{30}$$

where M is a stiffness tensor and reads:

$$\mathrm{M} = [\rho^{\chi} m_{\mathrm{T}} + (1 - \rho^{\chi}) m_{\mathrm{R}}]\mathrm{L} + \begin{cases} \rho^{\chi}(1 - m_{\mathrm{T}})\mathrm{L} : \left(\vec{\mathbf{h}} \otimes \vec{\mathbf{h}}\right) + \rho^{\chi}\mathbf{N} \otimes \vec{\mathbf{h}} & \text{for } \vec{\mathbf{h}} : \mathbf{D} > 0 \\ \rho^{\chi}(m_{\mathrm{R}} - m_{\mathrm{T}})\mathrm{L} : \left(\vec{\mathbf{h}} \otimes \vec{\mathbf{h}}\right) & \text{for } \vec{\mathbf{h}} : \mathbf{D} \leq 0 \end{cases} \tag{31}$$

where χ, m_{T} and m_{R} are additional parameters. In conclusion, five material parameters, namely $\{\beta_r, R, \chi, m_{\mathrm{T}}, m_{\mathrm{R}}\}$ are required to incorporate the intergranular strain concept proposed by Niemunis and Herle. More details on this concept and the calibration process for these parameters are given in different works such as (Mašín, 2019).

Chapter 4: Parametric study of monopiles under static lateral loading conditions

4.1. Generalities

A numerical parametric study was conducted to analyze the performance of offshore monopiles in cohesionless soils under static lateral loading conditions. The study considered variations of pile geometry, soil properties and loading cases. For this, several 3D FE models were constructed, employing the commercial software Abaqus Standard for this purpose. The study is oriented for the analysis of pipe piles made of steel with diameters between $D = \{5 - 7\}$ m and embedment lengths between $L = \{20 - 30\}$ m. Different relative densities of the soils in the range of $D_r = \{40\% - 80\%\}$ were also investigated. In this study, the parameters of the Karlsruhe fine sand were used on most of the performed simulations. However, additional sands were also studied on some particular simulations.

4.2. Description of the FE models

4.2.1. Geometry and mesh

A sketch of the geometry and the adopted mesh of the Boundary Value Problems (BVPs) is presented in Fig. 13, where only half of an entire model is shown. This study focuses on the modelling of monopile foundations and their supporting soil domain. Therefore, three main parts were assembled in each BVP, namely, the pile, the soil inside the pile and the soil outside the pile (see Fig. 14). The monopile was considered as a 3D solid with a pipe section, given the complex volumetric interactions between pile and soil. The soil regions inside and outside the pile were considered as three-dimensional parts of the FE-model. All parts were constructed using 8-node and 6-node 3D linear continuum elements with full integration, which are available from the Abaqus Standard library. The other parts of the OWT, such as

the rotor-nacelle assembly, tower and substructure (transition piece), were simplified as a pressure applied to the top of the monopile (see Fig. 19).

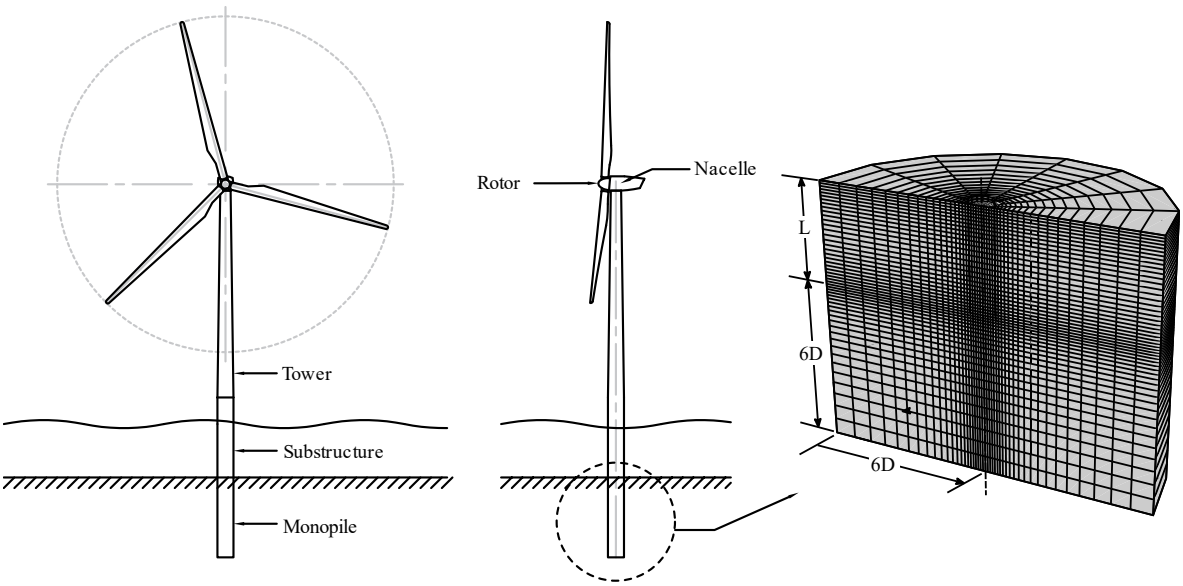

Fig. 13 Geometry and mesh of the FE Models.

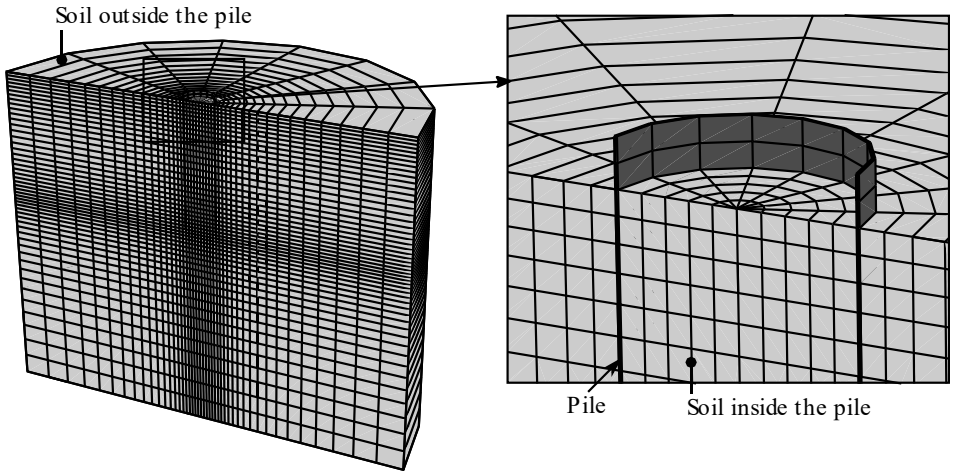

Fig. 14 Parts of the FE Models.

The dimensions of the pile were defined based on systematic variations of the diameter $D = \{5;\ 6;\ 7\}$ m and embedment length $L = \{20;\ 25;\ 30\}$ m. Considering this, the slenderness ratio L/D of the different monopiles ranged between $L/D = \{2.86 - 6.00\}$. The geometric configurations of each model is outlined in detail in Section 4.2.7. The monopile protrudes 1 m above the soil domain. The pile wall thickness was assumed as $t_p = \{0.06;\ 0.07; 0.08\}$

m for the monopiles with diameter $D = \{5;\ 6;\ 7\}$ m respectively, which is in agreement with the minimum wall thickness established by (API, 2014a) as:

$$t_p\ [\text{mm}] = 6.35 + \frac{D\ [\text{mm}]}{100} \tag{32}$$

The length of the soil inside the pile was defined as equal to the embedment length of the monopile, as a fully-plugged pile. The soil domain outside the monopile was modelled within a radius of $6D$ around the pile axis, and up to a distance below the pile base of $6D$ (see Fig. 13). This domain size was chosen in order to avoid boundary effects. A gradual mesh refinement scheme was adopted in the regions near the monopile (specially near the pile's base and head) in order to provide a mesh independent solution. The elements immediately next to the pile had an approximate size of 0.5 m.

4.2.2. Materials

The monopiles were made of steel, which was assumed to be linear elastic. The steel material was characterized by a Young modulus of $E = 210$ GPa, a Poisson's ratio of $\nu = 0.3$ and a unit weight of $\gamma_p = 78.5$ kN/m^3. The latter material properties are summarized in Table 1. The effect of the pile surface roughness was considered in the definition of the frictional behavior described in Section 4.2.3. The mechanical behavior of the soils was simulated with the hypoplastic constitutive model for sands by von Wolffersdorff (von Wolffersdorff, 1996) extended by the Intergranular Strain (IS) approach by Niemunis and Herle (Niemunis & Herle, 1997), which was described in the previous section and is hereafter referred to as the IS-hypoplastic model. The mechanical constitutive behavior of the soil was defined through a user-defined subroutine UMAT, which is written in FORTRAN.

The analysis covered six different sands, varying from fine to coarse grained cohesionless soils. The Karlsruhe fine sand (KFS) was selected for most of the conducted simulations, considering that this sand has been extensively calibrated for simulations on FE-applications (Fuentes et al., 2017; Poblete et al., 2016; Westermann et al., 2014a, 2014b; Wichtmann, 2016). The five additional sands correspond to Hochstetten sand (HS), Toyoura sand (TS), Berlin sand (BS), Komorany sand (KS) and Sand '3'. Table 2 presents a summary of the index properties of the mentioned sands, including main size D_{50}, maximum void ratio $e_{\max}$, minimum void ratio $e_{\min}$, coefficient of uniformity $c_u = D_{60}/D_{10}$ and specific gravity G_s. The saturated unit weight of the soil was assumed for all sands as $\gamma_{sat} = \{18.67;\ 19.03;\ 19.42\}$ kN/m^3 for the relative densities $D_r = \{40\%;\ 60\%;\ 80\%\}$ respectively. The initial relative density of the soil was incorporated into the FE models by initializing the distribution of the void ratio e according to the corresponding relative density D_r (See Equation (33)). For the simulation with the IS-hypoplastic model, material parameters reported in (Herle & Gudehus, 1999; Le, 2015; Mašín, 2019; Westermann et al.,

2014a; Wichtmann, 2005) were directly adopted for the mentioned sands. Their values are given in Table 3.

Table 1 Material properties of the monopiles

E_p [GPa]	ν [−]	γ_p [kN/m^3]
210	0.3	78.5

Table 2 Index properties of different sands considered in the present study. Values adopted from (Herle & Gudehus, 1999; Le, 2015; Mašín, 2019; Westermann et al., 2014a; Wichtmann, 2005)

Material	$e_{\max}$[−]	$e_{\min}$ [−]	D_{50} [mm]	c_u [−]	G_s [−]
Fine sand	1.054	0.677	0.14	1.50	2.66
Hochstetten sand	0.95	0.55	0.20	1.60	2.65
Toyoura sand	0.98	0.61	0.16	1.46	2.64
Berlin sand	0.688	0.391	0.55	3.30	2.61
Komorany sand	0.870	0.350	–	–	–
Sand ’3’	0.874	0.577	0.55	1.80	–

Table 3 Parameters of the IS-hypoplastic model. Values adopted from (Herle & Gudehus, 1999; Le, 2015; Mašín, 2019; Westermann et al., 2014a; Wichtmann, 2005)

Parameter	Karlsruhe fine sand	Hochstetten sand	Toyoura sand	Berlin sand	Komorany sand	Sand ‘3’
φ_c	33.1	33.0	30.0	31.5	35.0	31.2
h_s	862600	1500000	2600000	2300000	50000	591000
n_B	0.32	0.28	0.27	0.30	0.20	0.50
e_{d0}	0.677	0.55	0.61	0.391	0.350	0.577
e_{c0}	1.054	0.95	0.98	0.688	0.870	0.874
e_{i0}	1.212	1.05	1.10	0.791	1.040	1.005
α	0.21	0.25	0.18	0.13	0.26	0.12
β	1.5	1.5	1.1	1.0	4.0	1.0
m_T	2.0	2.0	4.0	2.2	1.7	1.45
m_R	4.0	5.0	8.0	4.4	3.4	2.9
R	1.0×10^{-4}	1.0×10^{-4}	2.0×10^{-5}	1.0×10^{-4}	2.0×10^{-4}	1.0×10^{-4}
β_R	0.1	0.5	0.1	0.2	0.12	0.2
χ	6.0	6.0	1.0	6.0	0.7	6.0

4.2.3. Soil-structure contact

Frictional behavior was set between the soil and the outer and inner sides of the pile. For this, the small-sliding, surface-to-surface master/slave contact pair formulation was set for the contact pairs. The surface-to-surface contact discretization allows for accurate stress and pressure results. The small-sliding tracking approach allows surfaces in contact to undergo sliding of one surface along the other, while providing computational savings and added

robustness compared to the more general finite-sliding tracking approach (ABAQUS, Inc., 2006). For this, relatively minor sliding of one surface along the other is assumed, which also allows the assumption that the interaction between a slave node and its corresponding initial local area of the master surface will be maintained throughout the analysis.

The tangential motion was controlled with the penalty friction method, which accounts for a basic Coulomb friction model and allows for a small amount of elastic slip. The friction model defines a critical shear stress τ_{crit} at which the sliding of one surface along the other starts. The critical shear stress is equal to $\tau_{crit} = \mu\, p_{cont}$, where μ is the coefficient of friction computed in this work as $\mu = \tan\delta$, p_{cont} is the contact pressure between surfaces and δ is the interface friction angle. The angle δ may vary between 0 and φ (peak friction angle of the soil) depending on different aspects such as the pile surface roughness, mean grain size and installation methods. In this study, it was set as $\delta = 2/3\,\varphi$, and φ was assumed as $\varphi = \{35;\ 37;\ 40\}^{\circ}$ for the relative densities $D_r = \{40\%;\ 60\%;\ 80\%\}$ respectively. Still, a FE sensitivity analysis was conducted for an specific pile geometry considering different values of $\delta = \{1/3\,\varphi; 1/2\,\varphi; 2/3\,\varphi\}$ and it was found that its variation under the evaluated range has a negligible effect on the pile displacements predicted by the FE-simulations.

On the other hand, the normal behavior was customized through a hard contact pressure-overclosure relationship. The linear penalty method was used as the constraint enforcement method for this relationship. The hard contact relationship allows the transfer of any contact pressure between the surfaces in contact and disables the transfer of tensile stresses. Therefore, once the contact pressure reaches zero, the surfaces are allowed to separate.

4.2.4. Initial and boundary conditions

Displacement constraints were applied to the lateral and bottom boundary surfaces of the soil domain (see Fig. 15). In this way, the vertical displacements of the soil domain were fixed on the bottom boundary as well as the horizontal displacements on the lateral boundaries. The top boundary of the model is free to displace.

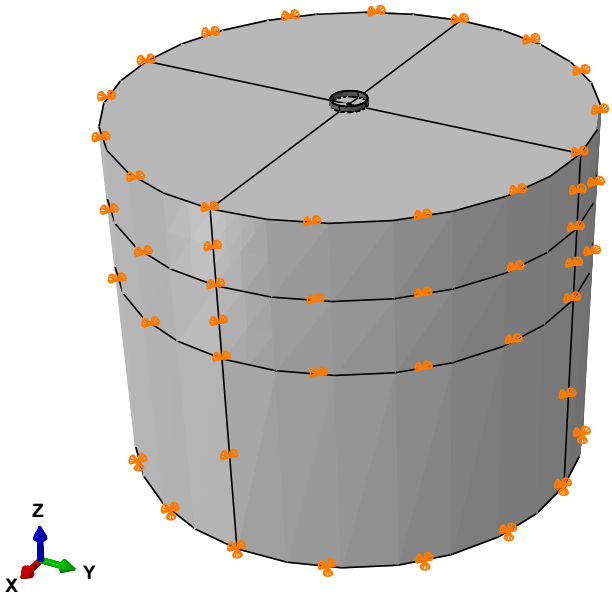

Fig. 15 Displacement constraints applied on the FE models.

The initial stress state of the soil was set as a user-subroutine-defined initial stress field through a SIGINI user-subroutine. The void ratio, pore water pressure and intergranular strain are defined as state variables. Their initial states were set as initial solution-dependent state variable fields through a SDVINI user-subroutine. Initial conditions for the stresses result from a geostatic K_0 condition, following the equation $\sigma_{11} = \sigma_{22} = K_0\sigma_{33}$. The lateral earth pressure coefficient was set to $K_0 = 1 - \sin\varphi_c$ according to the Jaky's equation, where φ_c is the critical state friction angle of the soil. The initial distribution for the vertical stresses was computed according to the corresponding saturated unit weight of the soil γ_{sat} for a given relative density D_r and assuming a gravity acceleration equal to $g = 10$ m/s^2. The initial distribution of the pore water pressure was computed considering an intrinsic unit weight of the water of $\gamma_w = 10$ kN/m^3 and a 20 m water column above the ground surface. An example of the initial stress field and pore water pressure distribution for a model with $D = 6$ m, $L = 25$ m and $D_r = 60\%$ is given in the following figures. Fig. 16 presents the initial distribution of the total vertical stress and Fig. 17 presents the initial pore water pressure distribution.

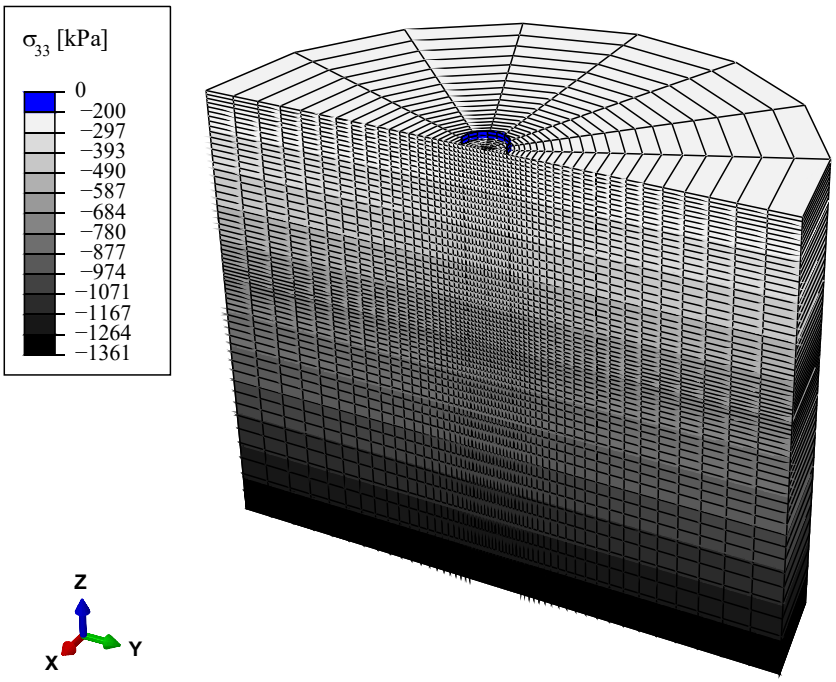

Fig. 16 Initial distribution of the total vertical stresses for a FE model with $D = 6$ m, $L = 25$ m and $D_r = 60\%$. Karlsruhe fine sand parameters from (Westermann et al., 2014a), see Table 3.

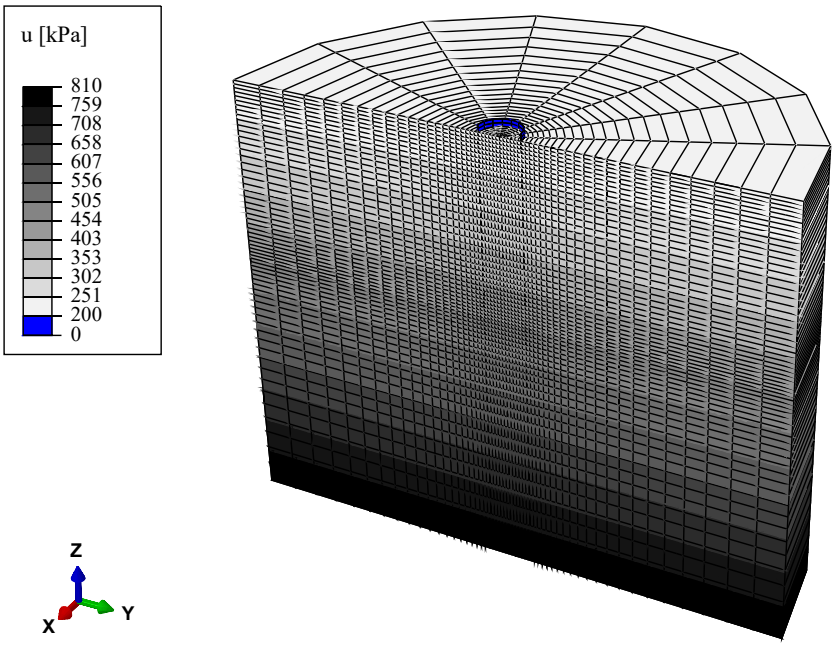

Fig. 17 Initial distribution of the pore water pressure for a FE model with $D = 6$ m, $L = 25$ m and $D_r = 60\%$. Karlsruhe fine sand parameters from (Westermann et al., 2014a), see Table 3.

The void ratio e was initialized according to the corresponding relative density D_r, as:

$$e = e_c - D_r(e_c - e_d) \tag{33}$$

where e_c and e_d are the pressure dependent critical and minimum void ratio, according to the Bauers equation (Bauer, 1992), which states that:

$$\frac{e_c}{e_{c0}} = \frac{e_d}{e_{d0}} = \exp\left(-\left(\frac{3\bar{\sigma}}{h_s}\right)^{n_B}\right) \tag{34}$$

where e_{c0} and e_{d0} are the critical and minimum void ratios for a mean (effective) stress $\bar{\sigma} = 0$ kPa respectively, and h_s and n_B are material parameters (Bauer, 1992; Niemunis, 2003). The void ratio e_{c0} can be obtained as the maximum void ratio $e_{c0} = e_{\max}$ according to the standard ASTM D4254-14 , while e_{d0} coincides with the minimum void ratio $e_{d0} = e_{\min}$ according to the standard ASTM D4253-16. Fig. 18 presents the initial distribution of the void ratio e_0 computed for a FE model with $D = 6$ m, $L = 25$ m, $D_r = 60\%$ and the parameters from the Karlsruhe fine sand parameters from Table 3. Finally, the intergranular strain was initialized as fully mobilized pointing in the vertical direction, as:

$$h_{33} = -1.00 \times R \tag{35}$$

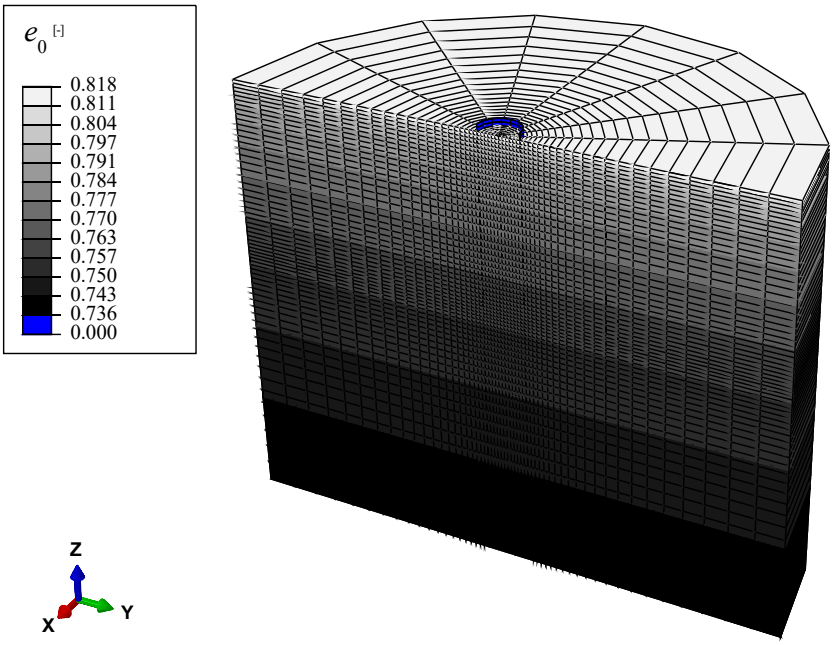

Fig. 18 Initial distribution of the void ratio for a FE model with $D = 6$ m, $L = 25$ m and $D_r = 60\%$. Karlsruhe fine sand parameters from (Westermann et al., 2014a), see Table 3.

4.2.5. Loading conditions

The monopile is subjected to the action of a vertical load Q and a horizontal load H. The vertical load includes the weights of the tower, substructure, nacelle and turbine rotor. The horizontal load represents the action of the environmental loading and is virtually located at a vertical distance h from the ground level, as shown in Fig. 19.a, generating a moment at ground level equal to $M = H \cdot h$.

For the estimation of the vertical forces, reference values for a 5-MW wind turbine were chosen. To do so, the weights of the nacelle and turbine rotor reported by (Jonkman et al., 2009) for a wind turbine of this type were considered. Along with the self weight of a 80-meter tower and a 30-meter substructure, the sum of these components was estimated to $Q = 8680$ kN. Note that according to (Arshad & O'Kelly, 2016), a typical gravitational loading acting on a monopile is expected to be in the range of $2000 - 8000$ kN. The vertical loads are applied on the FE models as a distributed surcharge load q acting on the top of the monopile (see Fig. 19.b, where only half of the model is shown). The horizontal load H was applied as two components $H/2$ acting on the monopile at ground level. The moment generated by the arm h was simulated as an equivalent pair of vertical forces V at the top of the monopile, as shown in Fig. 19.b, such that $V = M/D$ and $M = H \cdot h$ hold. Finally, the 20-meter water column above the ground surface was considered as an external pressure acting on the top of the soil, equal to $q_w = 20\ \text{m} \cdot \gamma_w$.

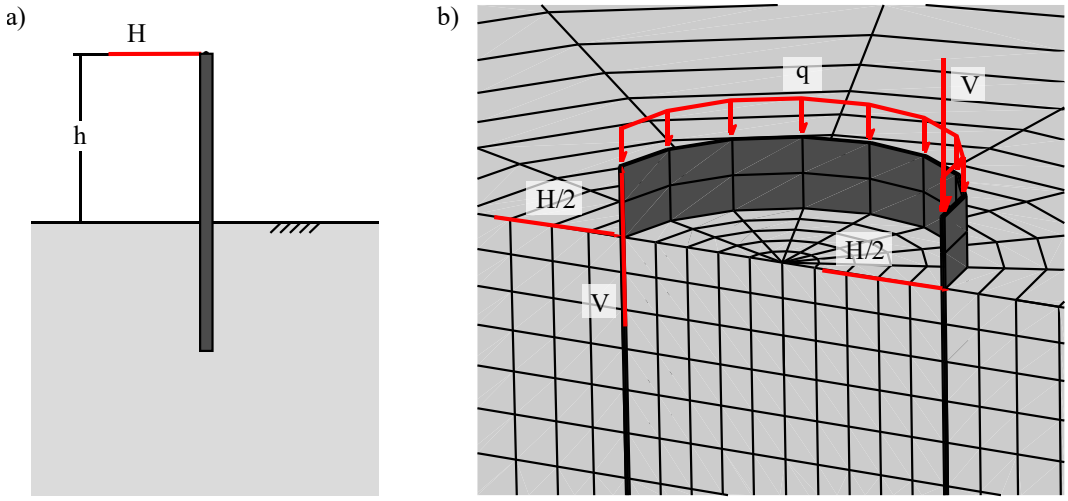

Fig. 19 Applied loads on monopile considered on the FE models.

4.2.6. Steps of analysis

The simulations were conducted in three analysis steps. For all simulation steps, static analysis was assumed and drained conditions without consolidation effects were considered for the soil. The steps of analysis were defined as follows:

i. **First analysis step**: A geostatic step is solved to establish an equilibrium state of stresses. Previous to this step, the geostatic stresses and state variables are initialized as described above. In this step, gravity load is applied to the entire model and equilibrium between the applied load, the initial stress field and the boundary conditions is checked. The total time of this step is $t = 1$ s.

ii. **Second analysis step:** In this step, the distributed load q is gradually applied to the monopile, as shown in Fig. 19.b. The step is solved as a static load step. The total time step is $t = 1$ s.

iii. **Third analysis step:** In this step, the horizontal concentrated forces $H/2$ and the equivalent pair of vertical forces V are gradually applied to the monopile, see Fig. 19.b. This step is also solved as a static load step. The total time step is $t = 1.5$ s.

The FE simulations were conducted assuming a simplified "wished-in-place" initial condition for the piles. This means that the evaluation of the installation processes and their corresponding effects on different variables, such as soil's density and distribution of stresses around the monopile, are not considered in the present study. Further analyses on the implications of this assumption on the results of this work is given in Section 4.3.

4.2.7. Lists of FE models and simulations

In total, a number of 42 different 3D FE models, combining the above mentioned variations of geometric configurations and soil conditions, were built. Different loading schemes were considered on the constructed FE models, resulting in 96 simulations. The simulations were run in a workstation with the following specifications: Memory $= 32$ Gb RAM, storage= 1 TB SSD. Table 4 provides a summary of the constructed FE models.

Table 4 Summary of the constructed FE-models

Sand	L [mm]	D [mm]	L/D	D_r[%]	Model
KFS	20	5	4.00	40	$M1$
				60	$M2$
				80	$M3$
		6	3.33	40	$M4$
				60	$M5$
				80	$M6$
		7	2.86	40	$M7$
				60	$M8$
				80	$M9$
	25	5	5.00	40	$M10$
				60	$M11$
				80	$M12$
		6	4.17	40	$M13$
				60	$M14$
				80	$M15$
		7	3.57	40	$M16$
				60	$M17$
				80	$M18$
	30	5	6.00	40	$M19$
				60	$M20$
				80	$M21$
		6	5.00	40	$M22$
				60	$M23$
				80	$M24$
		7	4.29	40	$M25$
				60	$M26$
				80	$M27$
HS	25	5	5.00	40	$M28$
				60	$M29$
				80	$M30$
		6	4.17	40	$M31$
				60	$M32$
				80	$M33$
TS	25	5	5.00	40	$M34$
				60	$M35$
				80	$M36$
		6	4.17	40	$M37$
				60	$M38$
				80	$M39$
BS	25	6	4.17	60	$M40$
KS	25	6	4.17	60	$M41$
S3	25	6	4.17	60	$M42$

Note: KFS = Karlsruhe fine sand, HS = Hochstetten sand, TS = Toyoura sand, BS = Berlin sand, KS = Komorany sand, S3 = Sand '3'.

The performed simulations were organized in three different sets. The first set of FE simulations was performed to analyze the effects of different pile geometries and loading cases on the behavior of the monopile embedded in a specific sand. Systematic variations of the monopile diameter $D = \{5;\ 6;\ 7\}$ m and embedment length $L = \{20;\ 25;\ 30\}$ m were studied. Two loading cases were evaluated by assessing two values of the load eccentricity $h = \{20;\ 40\}$ m. The first loading case (LC1) corresponds to $h = 20$ m, while the second loading case (LC2) corresponds to $h = 40$ m. Low magnitude environmental conditions were applied to the monopile, corresponding to the serviceability limit state (experienced frequently during the wind turbine's lifetime). To this end, force magnitudes $H \leq 2$ MN were considered (LeBlanc, Houlsby, et al., 2010). In all cases, the horizontal force H was applied till reaching a moment $M = H \cdot h$ equal to $M = 40$ MN·m. The latter corresponds to values of $H = \{2; 1\}$ MN for the loading cases LC1 and LC2 respectively. Regarding the soil material, the parameters of the Karslruhe fine sand were used for the IS-Hypoplastic model in the FE simulations. Three values of the relative density were evaluated as $D_r = \{40\%;\ 60\%;\ 80\%\}$. The above mentioned variations resulted in 54 simulations, which are summarized in Table 5.

In the second set of FE simulations, the response of monopiles under more severe loading conditions was studied, corresponding to the ultimate limit state (experienced once during the wind turbine's lifetime) (LeBlanc, Houlsby, et al., 2010). For this, horizontal forces up to $H = 6$ MN were applied to monopiles with different geometries embedded in a specific sand. In this case, only a distance h above the groundline equal to $h = 20$ m was evaluated. This loading case is hereafter referred to as the loading case LC3. As by the first set of FE simulations, the parameters of the Karlsruhe fine sand for the IS-Hypoplastic model and variations of $D = \{5;\ 6;\ 7\}$ m, $L = \{20;\ 25;\ 30\}$ m and $D_r = \{40\%;\ 60\%;\ 80\%\}$ were considered. The above mentioned variations resulted in 27 simulations, which are summarized in Table 6.

The third set of FE simulations was conducted to evaluate the monopile response embedded in different sands. For this analysis, the parameters of six different sands, including the Karlsruhe fine sand, were adopted for the FE simulations according to Table 3. In this case, the loading case LC3 was applied to the monopiles. Variations of $D = \{5;\ 6\}$ m and $D_r = \{40\%;\ 60\%;\ 80\%\}$ and a value of $L = 25$ m were considered on the simulations, as shown in Table 7.

Table 5 Summary of the first set of FE-simulations

Sand	L [mm]	D [mm]	L/D	D_r[%]	Model	Loading case	Simulation
KFS	20	5	4.00	40	$M1$	$LC1$	$S1$
						$LC2$	$S2$
				60	$M2$	$LC1$	$S3$
						$LC2$	$S4$
				80	$M3$	$LC1$	$S5$
						$LC2$	$S6$
		6	3.33	40	$M4$	$LC1$	$S7$
						$LC2$	$S8$
				60	$M5$	$LC1$	$S9$
						$LC2$	$S10$
				80	$M6$	$LC1$	$S11$
						$LC2$	$S12$
		7	2.86	40	$M7$	$LC1$	$S13$
						$LC2$	$S14$
				60	$M8$	$LC1$	$S15$
						$LC2$	$S16$
				80	$M9$	$LC1$	$S17$
						$LC2$	$S18$
	25	5	4.00	40	$M10$	$LC1$	$S19$
						$LC2$	$S20$
				60	$M11$	$LC1$	$S21$
						$LC2$	$S22$
				80	$M12$	$LC1$	$S23$
						$LC2$	$S24$
		6	3.33	40	$M13$	$LC1$	$S25$
						$LC2$	$S26$
				60	$M14$	$LC1$	$S27$
						$LC2$	$S28$
				80	$M15$	$LC1$	$S29$
						$LC2$	$S30$
		7	2.86	40	$M16$	$LC1$	$S31$
						$LC2$	$S32$
				60	$M17$	$LC1$	$S33$
						$LC2$	$S34$
				80	$M18$	$LC1$	$S35$
						$LC2$	$S36$
	30	5	4.00	40	$M19$	$LC1$	$S37$
						$LC2$	$S38$
				60	$M20$	$LC1$	$S39$
						$LC2$	$S40$
				80	$M21$	$LC1$	$S41$
						$LC2$	$S42$
		6	3.33	40	$M22$	$LC1$	$S43$
						$LC2$	$S44$
				60	$M23$	$LC1$	$S45$
						$LC2$	$S46$

			80	$M24$	$LC1$	$S47$
					$LC2$	$S48$
	7	2.86	40	$M25$	$LC1$	$S49$
					$LC2$	$S50$
			60	$M26$	$LC1$	$S51$
					$LC2$	$S52$
			80	$M27$	$LC1$	$S53$
					$LC2$	$S54$

Note
$LC1$: Loading case 1; Maximum applied force $H = 2$ MN at a height of $h = 20$ m.
$LC2$: Loading case 2; Maximum applied force $H = 1$ MN at a height of $h = 40$ m.

Table 6 Summary of the second set of FE-simulations

Sand	L [mm]	D [mm]	L/D	D_r[%]	Model	Loading case	Simulation
KFS	20	5	4.00	40	$M1$	$LC3$	$S55$
				60	$M2$	$LC3$	$S56$
				80	$M3$	$LC3$	$S57$
		6	3.33	40	$M4$	$LC3$	$S58$
				60	$M5$	$LC3$	$S59$
				80	$M6$	$LC3$	$S60$
		7	2.86	40	$M7$	$LC3$	$S61$
				60	$M8$	$LC3$	$S62$
				80	$M9$	$LC3$	$S63$
	25	5	4.00	40	$M10$	$LC3$	$S64$
				60	$M11$	$LC3$	$S65$
				80	$M12$	$LC3$	$S66$
		6	3.33	40	$M13$	$LC3$	$S67$
				60	$M14$	$LC3$	$S68$
				80	$M15$	$LC3$	$S69$
		7	2.86	40	$M16$	$LC3$	$S70$
				60	$M17$	$LC3$	$S71$
				80	$M18$	$LC3$	$S72$
	30	5	4.00	40	$M19$	$LC3$	$S73$
				60	$M20$	$LC3$	$S74$
				80	$M21$	$LC3$	$S75$
		6	3.33	40	$M22$	$LC3$	$S76$
				60	$M23$	$LC3$	$S77$
				80	$M24$	$LC3$	$S78$
		7	2.86	40	$M25$	$LC3$	$S79$
				60	$M26$	$LC3$	$S80$
				80	$M27$	$LC3$	$S81$

Note
$LC3$: Loading case 3; Maximum applied force $H = 6$ MN at a height of $h = 20$ m.

Table 7 Summary of the third set of FE-simulations

Sand	L [mm]	D [mm]	L/D	D_r[%]	Model	Loading case	Simulation
KFS	25	5	4.00	40	$M10$	$LC3$	$S64$
				60	$M11$	$LC3$	$S65$
				80	$M12$	$LC3$	$S66$
		6	3.33	40	$M13$	$LC3$	$S67$
				60	$M14$	$LC3$	$S68$
				80	$M15$	$LC3$	$S69$
HS	25	5	5.00	40	$M28$	$LC3$	$S82$
				60	$M29$	$LC3$	$S83$
				80	$M30$	$LC3$	$S84$
		6	4.17	40	$M31$	$LC3$	$S85$
				60	$M32$	$LC3$	$S86$
				80	$M33$	$LC3$	$S87$
TS	25	5	5.00	40	$M34$	$LC3$	$S88$
				60	$M35$	$LC3$	$S89$
				80	$M36$	$LC3$	$S90$
		6	4.17	40	$M37$	$LC3$	$S91$
				60	$M38$	$LC3$	$S92$
				80	$M39$	$LC3$	$S93$
BS	25	6	4.17	60	$M40$	$LC3$	$S94$
KS	25	6	4.17	60	$M41$	$LC3$	$S95$
S3	25	6	4.17	60	$M42$	$LC3$	$S96$

Note
$LC3$: Loading case 3; Maximum applied force $H = 6$ MN at a height of $h = 20$ m.

4.3. Description of the FE simulation results

4.3.1. First set of simulations

The response of monopiles considering low loading conditions and different pile geometries and loading cases was analyzed with the results from the first set of FE simulations. A typical contour of displacements for this set of simulations is shown in Fig. 20 for the case of a monopile with $L = 20$ m and $D = 6$ m embedded in Karlsruhe fine sand with $D_r = 60\%$ and under the action of the loading case LC1. The maximum total displacements are 0.030 m and the values of the maximum vertical and horizontal displacements are 0.021 m and 0.022 m respectively. In Fig. 20, displacements are observed along the entire length of the pile corresponding to the pile settlements caused by the action of the vertical loading and pile displacements caused by the action of the lateral loading. The largest displacements are located in the region near the pile head where the lateral loading is applied.

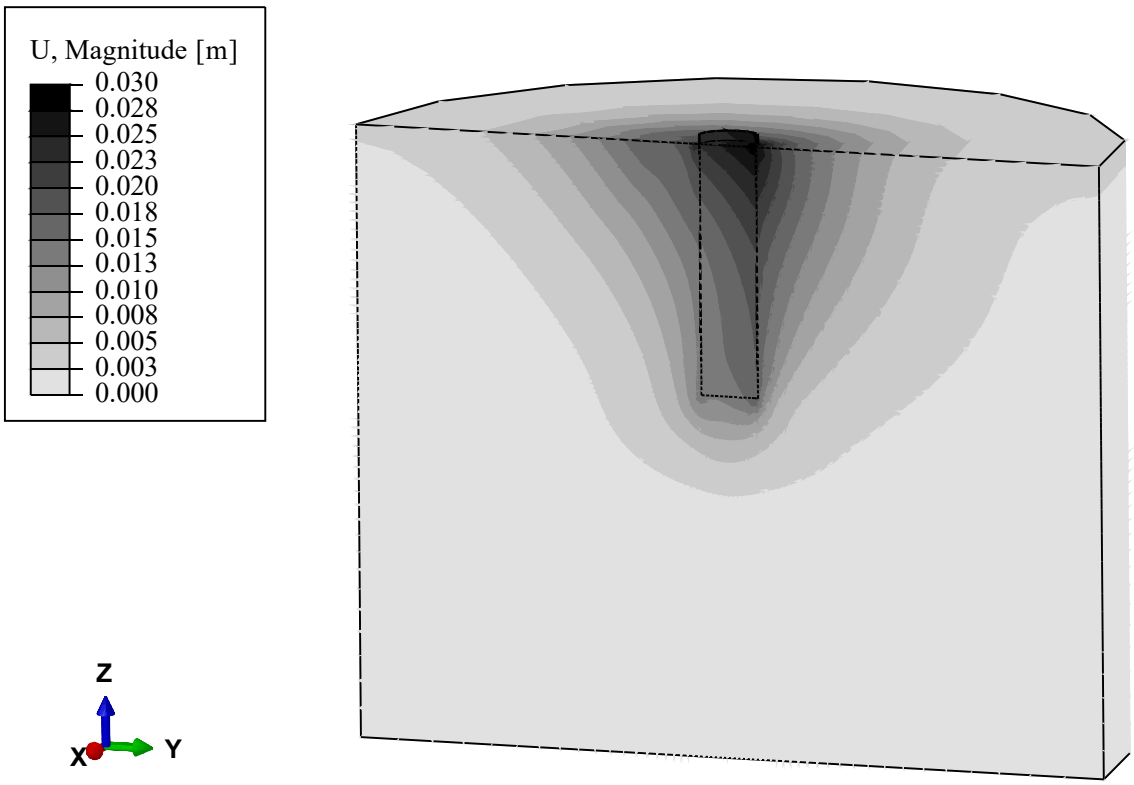

Fig. 20 Typical contour of displacements of the first set of simulations. Displacement units: meters. Pile length $L = 20$ m, pile diameter $D = 6$ m, relative density $D_r = 60\%$ and loading case LC1. Karlsruhe fine sand parameters from (Westermann et al., 2014a), see Table 3.

Deflection curves were obtained from the 54 simulations that conform the first set of FE simulations. The results are summarized in Fig. 21, Fig. 22 and Fig. 23 corresponding to the simulations with $L = \{20; 25; 30\}$ m respectively. The parametric study could capture different pile-soil flexural behavior varying from more rigid behavior in Fig. 21 ($L = 20$ m) to more flexible behavior in Fig. 23 ($L = 30$ m). Despite of the different flexural behaviors, all simulations presented rotational as well as flexural pile motion. Considering this, simplifications of the monopile motion as pure rigid or flexible behavior shall be avoided. Also, all simulations presented some mobilization of the pile base. This indicates that is quite possible that non-negligible shear reactions have been mobilized at the base of the piles. Section 4.3.4 will discuss this issue further.

As expected, the largest pile displacements are associated with lower relative densities and smaller pile diameters and embedment lengths. Also, for a given moment loading, a smaller load eccentricity h results in a larger force H, which generates more displacements. All the considered variations of pile geometry and loading cases appear to have a significant influence on the simulation results, as seen in Fig. 21 to Fig. 23.

The depth of the rotation point z_{rot} of the monopiles was also extracted from the FE simulations and analyzed. The simulations results suggest that the ratio z_{rot}/L is not significantly affected by changes in the pile diameter or relative density of the soil, and instead it seems to depend on the pile length and loading eccentricity. The average ratio z_{rot}/L for the models with $L = \{20;\ 25;\ 30\}$ m was estimated as $z_{rot}/L = \{0.75;\ 0.73;\ 0.70\}$. For increasing pile embedment length, the ratio z_{rot}/L seems to decrease. The average ratio z_{rot}/L for the models with $h = \{20;\ 40\}$ m was measured as $z_{rot}/L = \{0.75;\ 0.71\}$. The results suggest that for increasing load eccentricities, the ratio z_{rot}/L decreases. The maximum and minimum values of z_{rot}/L from all models were 0.78 and 0.61.

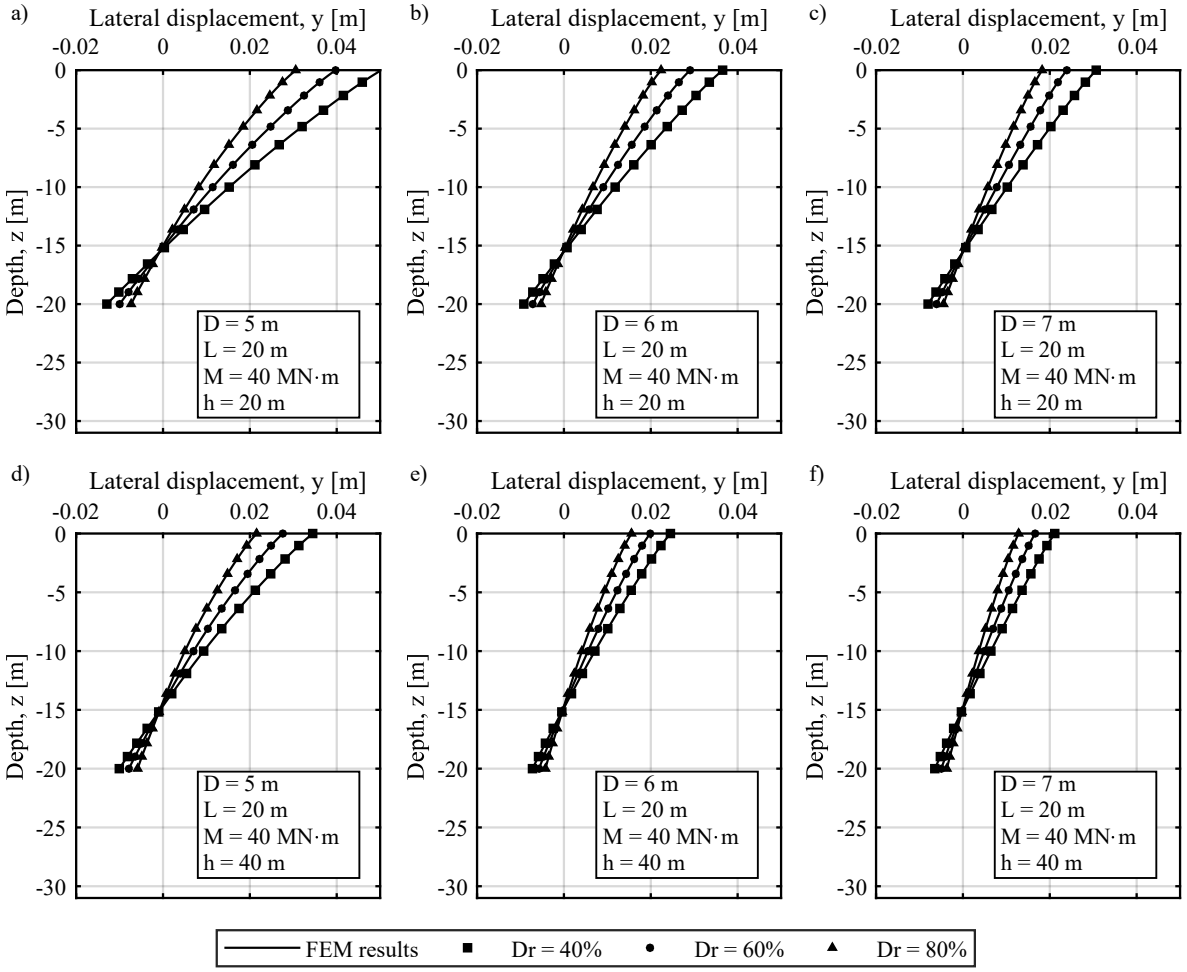

Fig. 21 FE simulation results of the first set of simulations. Pile deflection curves under static loading. Pile length $L = 20$ m, pile diameter $D = \{5;\ 6;\ 7\}$ m and relative densities $D_r = \{40\%;\ 60\%;\ 80\%\}$. Karlsruhe fine sand parameters from (Westermann et al., 2014a), see Table 3.

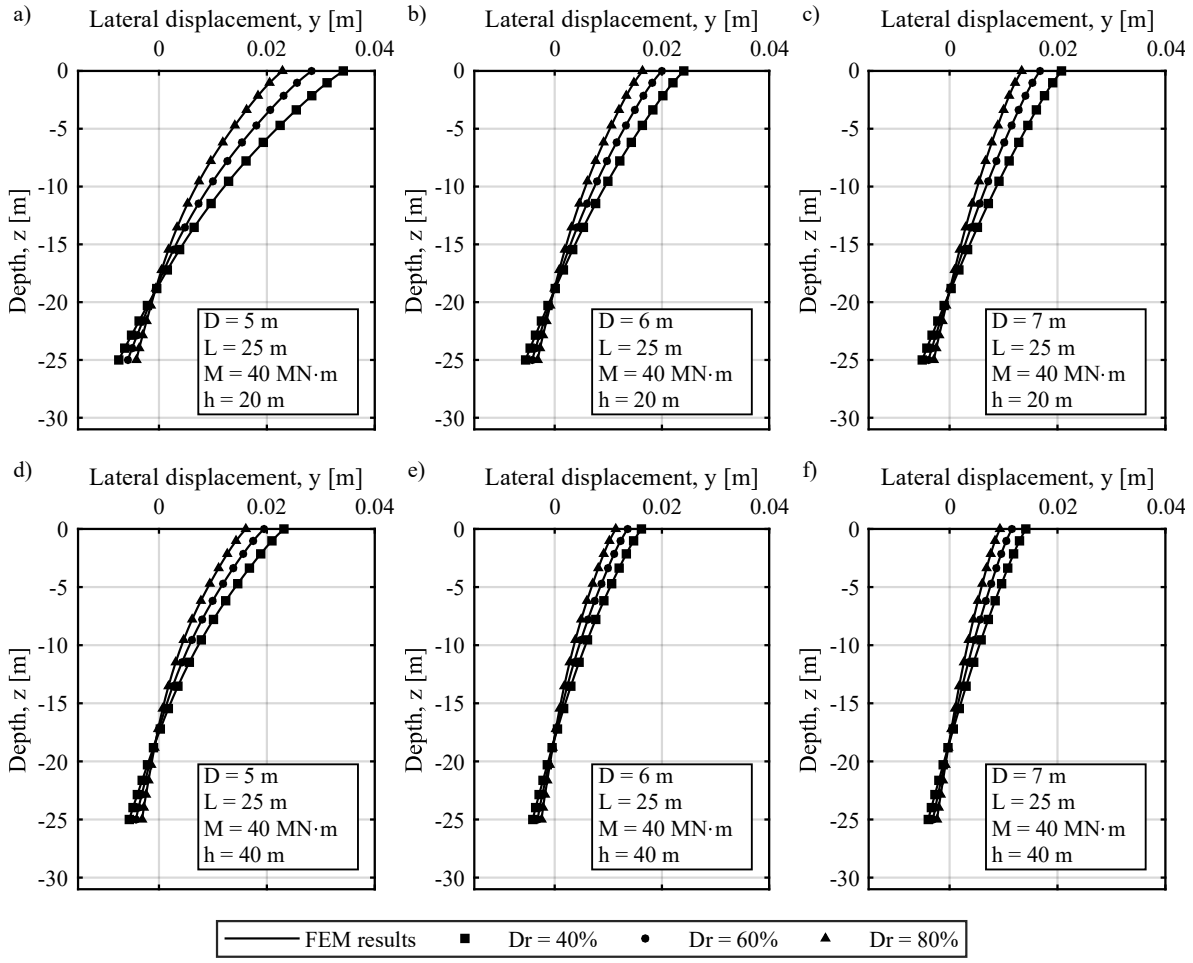

Fig. 22 FE simulation results of the first set of simulations. Pile deflection curves under static loading. Pile length $L = 25$ m, pile diameter $D = \{5;\ 6;\ 7\}$ m and relative densities $D_r = \{40\%;\ 60\%;\ 80\%\}$. Karlsruhe fine sand parameters from (Westermann et al., 2014a), see Table 3.

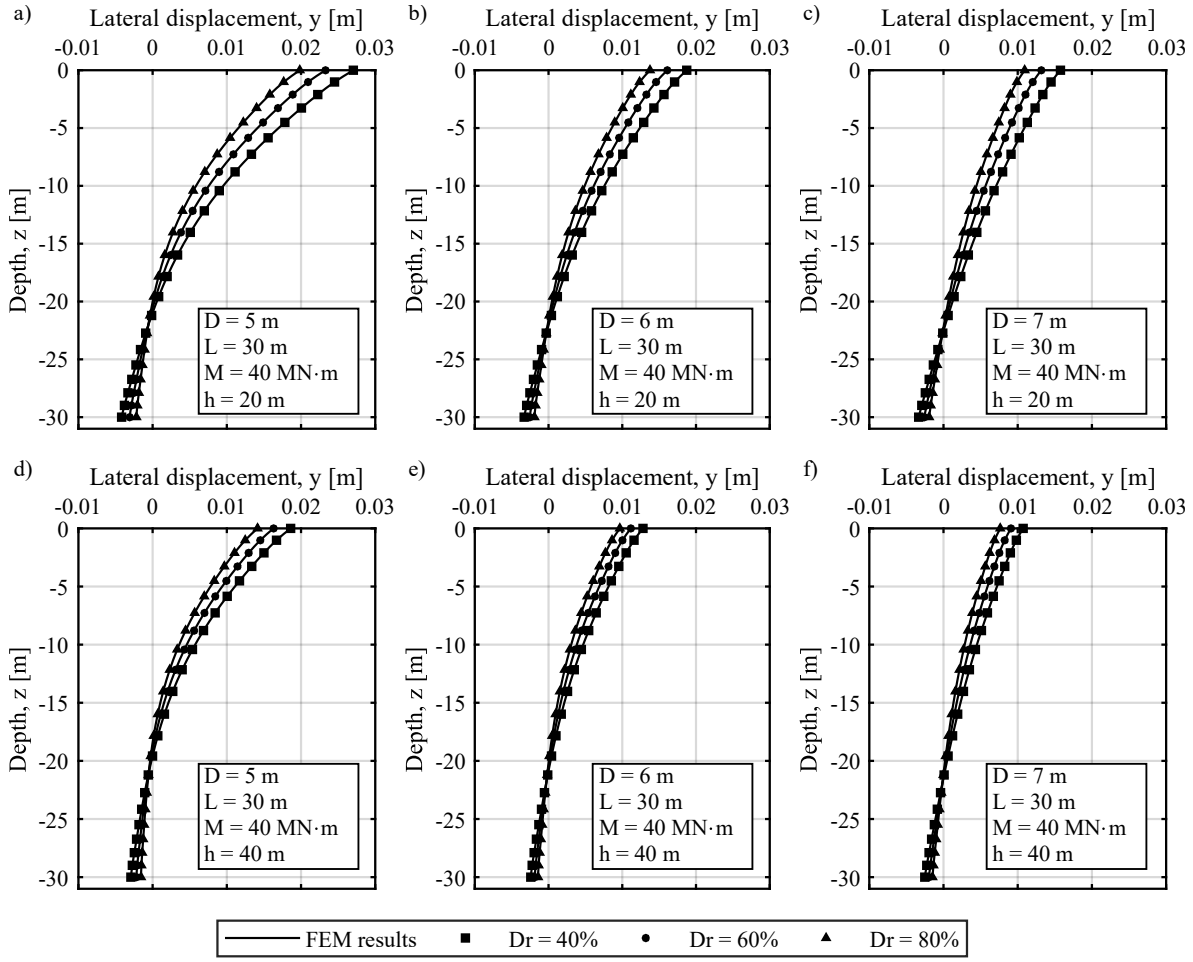

Fig. 23 FE simulation results of the first set of simulations. Pile deflection curves under static loading. Pile length $L = 30$ m, pile diameter $D = \{5;\ 6;\ 7\}$ m and relative densities $D_r = \{40\%;\ 60\%;\ 80\%\}$. Karlsruhe fine sand parameters from (Westermann et al., 2014a), see Table 3.

4.3.2. Second set of simulations

The response of monopiles considering more severe loading conditions and different pile geometries was analyzed with the results from the second set of FE simulations. A typical contour of displacements for this set of simulations is shown in Fig. 24 for the case of a monopile with $L = 20$ m and $D = 6$ m embedded in Karlsruhe fine sand with $D_r = 60\%$ and under the action of the loading case LC3. Compared to the first set of simulations, in this case the rotational motion of the monopile is more evident due to the higher lateral loads applied. The largest displacements are located in the regions near the pile's head and base, and a region with smaller displacements is observed above the pile base, which illustrates the tendency of the monopile to rotate around a rotation point.

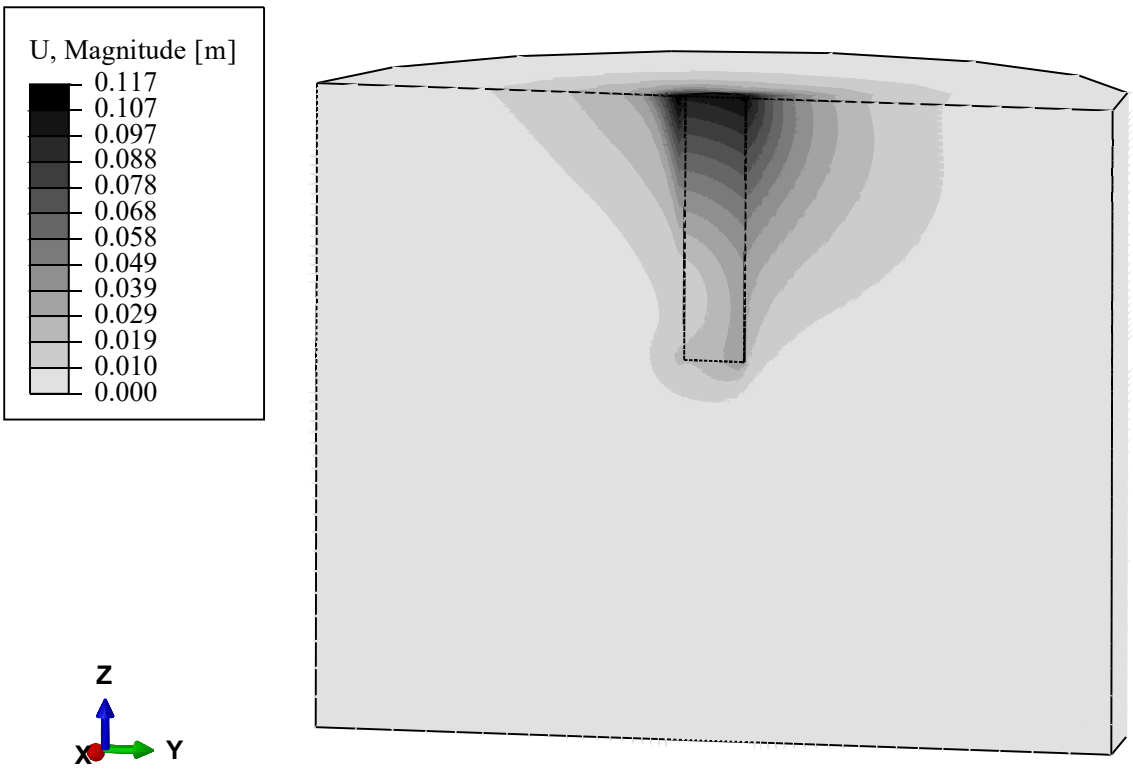

Fig. 24 Typical contour of displacements of the second set of simulations. Displacement units: meters. Pile length $L = 20$ m, pile diameter $D = 6$ m, relative density $D_r = 60\%$ and loading case LC3. Karlsruhe fine sand parameters from (Westermann et al., 2014a), see Table 3.

The evolution of the horizontal stresses on the soil domain is also analyzed with the FE simulations results. Fig. 25 presents the horizontal total stresses at different loading stages, namely, the initial condition, after the application of the vertical loading and after the application of the lateral loading. Considering the adopted "wished-in-place" modelling approach, only a negligible perturbance on the horizontal stresses is observed at the initial condition and due to the action of the vertical loading. After the application of the lateral loading, an increase of the horizontal stresses is observed on the front (right-hand) and upper side of the pile and on the back (left-hand) and bottom side of the pile. The effect is observed in a region within a distance of at least $2D$ around the monopile.

Load-displacement curves at ground level were obtained from the 27 simulations that conform the second set of FE simulations. For this, a coupled Abaqus/Python script was written to extract the pile displacements at ground level from the output files generated by the FE simulations. The resulting load-displacement curves are shown in Fig. 26. As by the first set of FE simulations, a strong influence of the pile geometry and soil relative density on the pile response is observed. The load-displacement curves show an non-linear behavior from the beginning and do not reach a plateau that indicates an ultimate pile resistance even when large loads are evaluated.

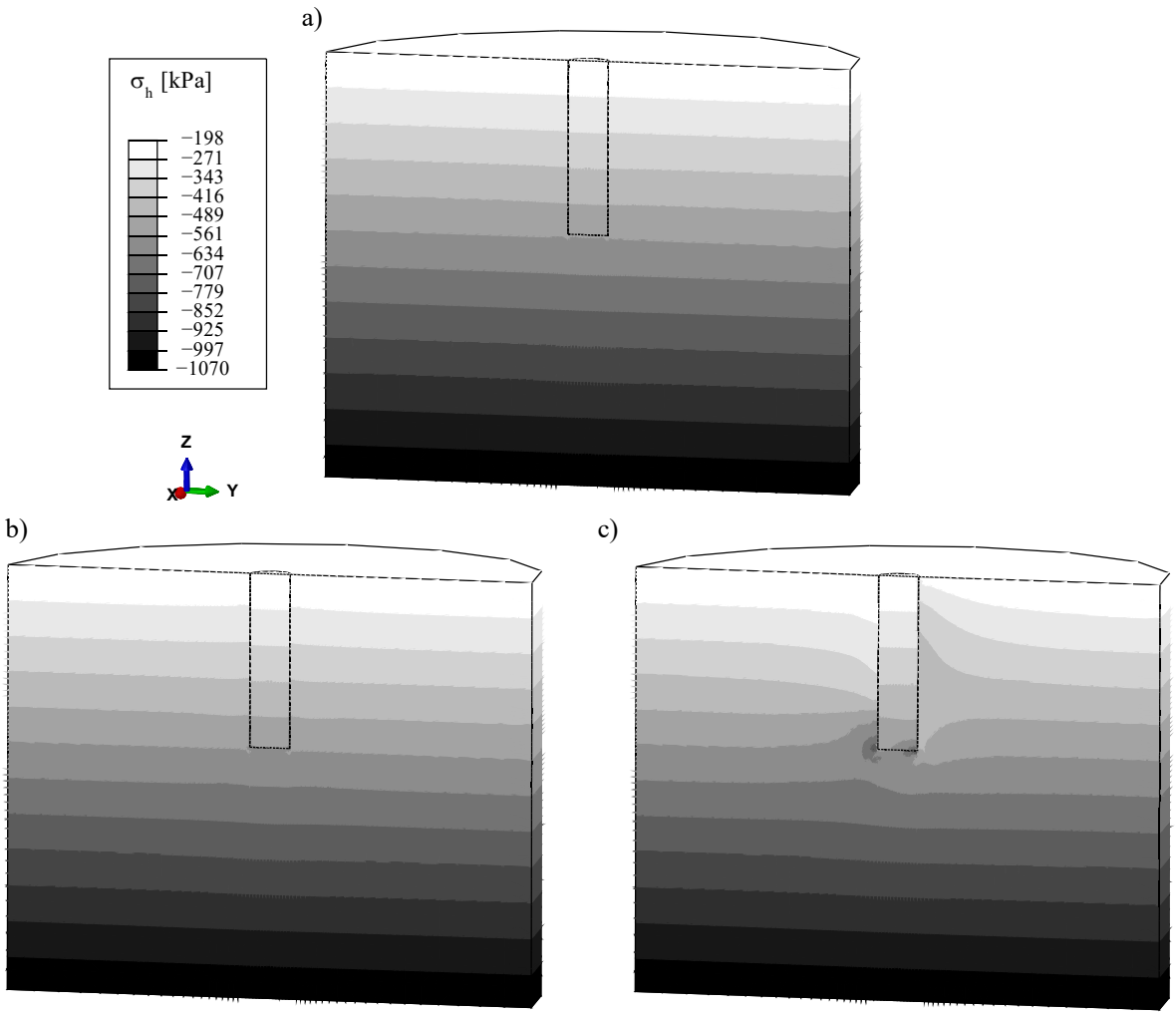

Fig. 25 Evolution of the horizontal stresses. Pile length $L = 20$ m, pile diameter $D = 6$ m, relative density $D_r = 60\%$ and loading case LC3. Karlsruhe fine sand parameters from (Westermann et al., 2014a), see Table 3.

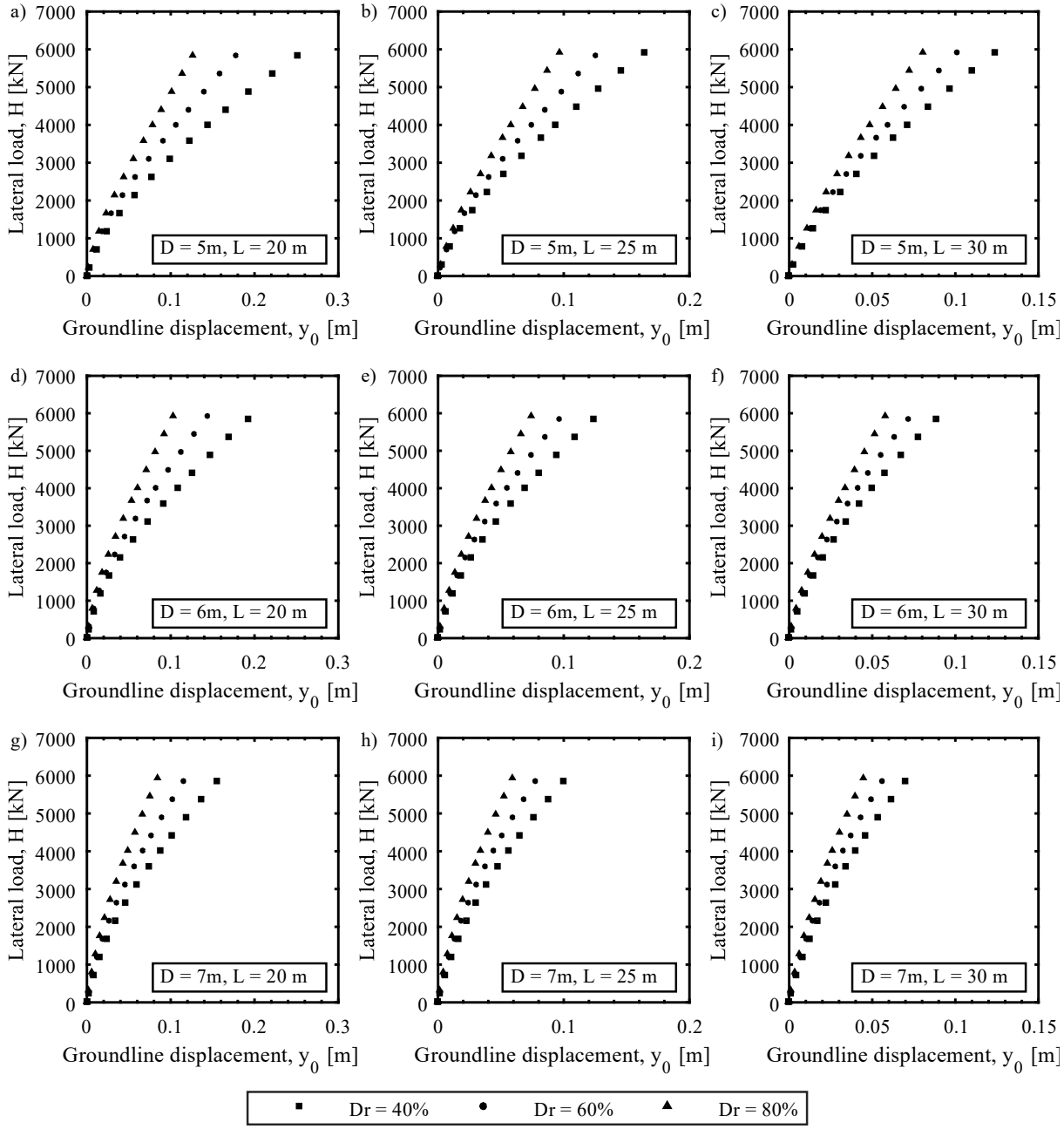

Fig. 26 FE simulation results of the second set of simulations. Load-deflection curves under static loading at ground level. Pile length $L = \{20; 25; 30\}$ m, pile diameter $D = \{5; 6; 7\}$ m and relative densities $D_r = \{40\%; 60\%; 80\%\}$. Karlsruhe fine sand parameters from (Westermann et al., 2014a), see Table 3.

4.3.3. Third set of simulations

The load-displacement curves from the third set of FE simulations are shown in Fig. 27 and Fig. 28. The same Abaqus/Python script described in the last section was used to extract the pile displacements at ground level. Fig. 27 presents the results of the simulations with three different fine sands, namely Karlsruhe fine sand, Hochstetten sand and Toyoura Sand, accounting for variations of the pile diameter $D = \{5;\ 6\}$ m and relative densities $D_r = \{40\%;\ 60\%;\ 80\%\}$ for a given length $L = 25$ m. Although the three sands are fine sands, there are notable differences between the pile load-displacement responses, specially when comparing the results for Toyoura sand with the results for the other sands. The largest groundline displacements, which are obtained on the simulation for Toyoura sand with $D_r = 40\%$, $D = 5$ m and $L = 25$ m, are in the range of $0.04\ D$. Even at that level of mobilization, load-displacement curves did not reach an evident ultimate pile resistance.

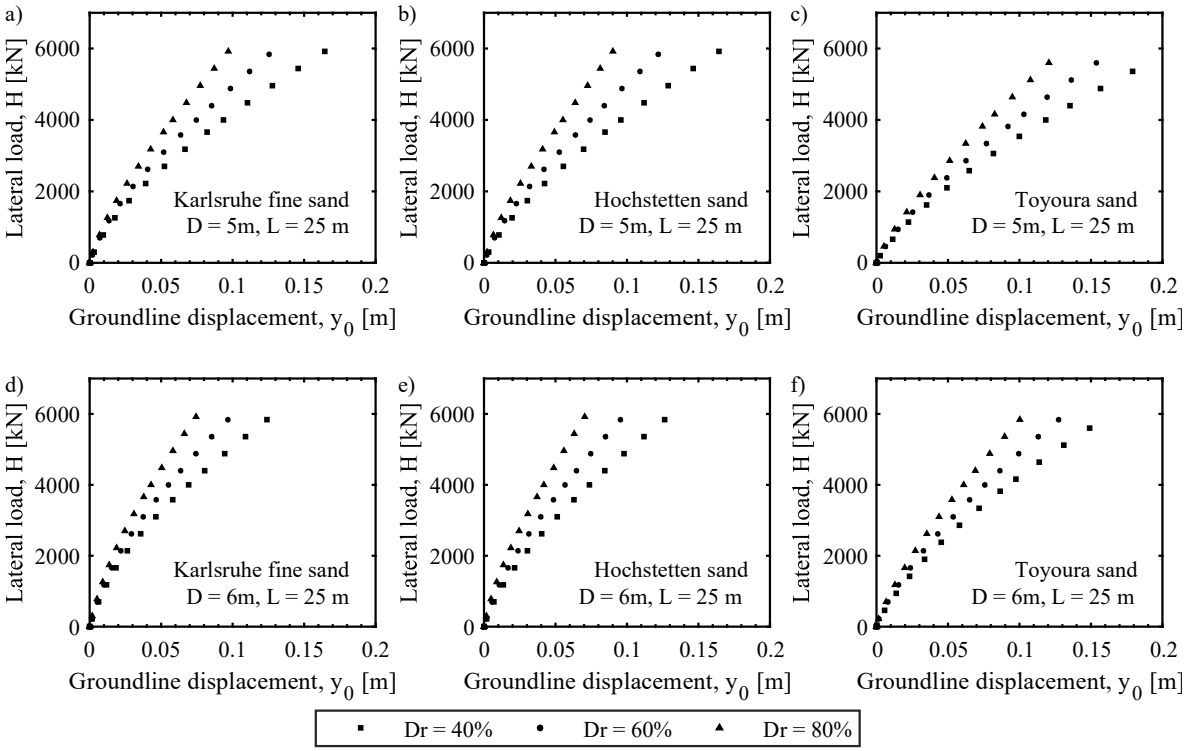

Fig. 27 FE simulation results of the third set of simulations. Load-deflection curves under static loading at ground level. Pile length $L = 25$ m, pile diameter $D = 6$ m and relative densities $D_r = \{40\%;\ 60\%;\ 80\%\}$. See Table 3 for material parameters.

Fig. 28 shows the load-displacement curves for six different sands considering a specific pile geometry, namely $D = 6$ m and $L = 25$ m, and a specific relative density of the soil $D_r = 60$ %. In this case, fine to coarse grained sands are considered. Very different pile responses were obtained for the same pile geometry and soil's relative density. The smallest pile displacements at ground level correspond to the model implementing the parameters of the

Komorany sand, whereas the largest displacements correspond to the model implementing the parameters of the Toyoura sand.

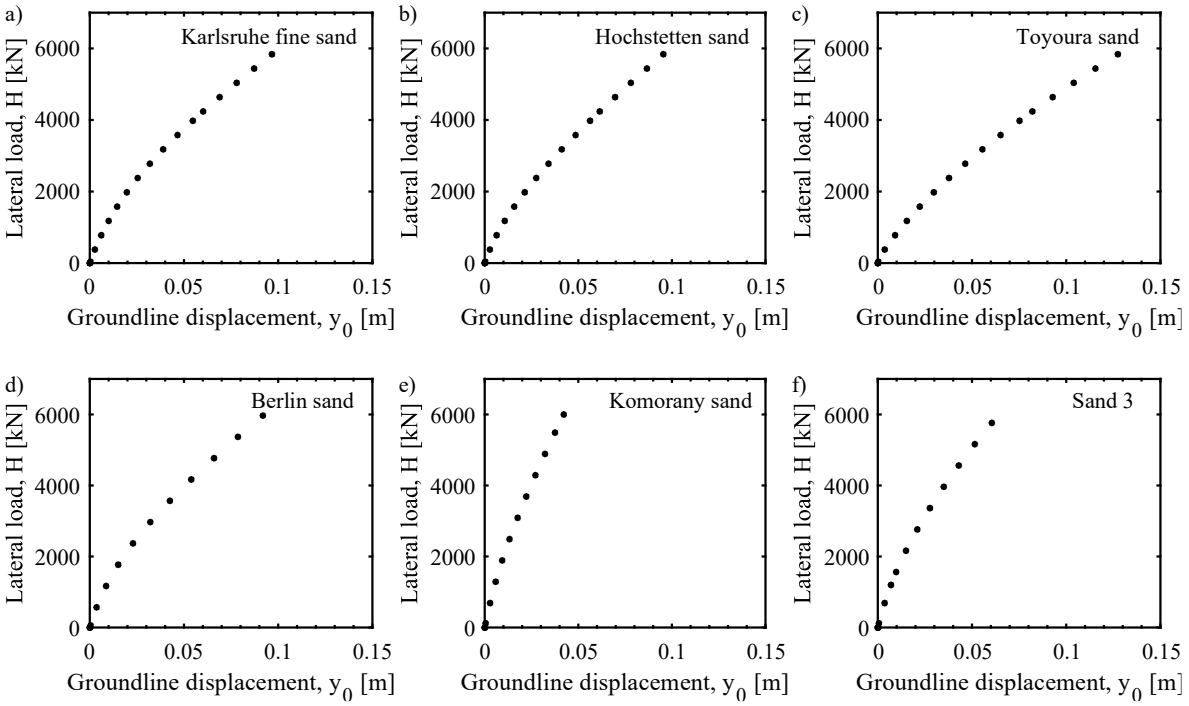

Fig. 28 FE simulation results of the third set of simulations. Load-deflection curves under static loading at ground level. Pile length $L = 25$ m, pile diameter $D = 6$ m and relative density $D_r = 60\%$. See Table 3 for material parameters.

4.3.4. Determination of the base shear reaction

In practice, there is little guidance on how to incorporate the base shear force into conventional p-y models, despite its proven importance. In fact, one of the main limitations of the conventional p-y method (e.g. (API, 2014b; DNV-GL-AS, 2016)) for its application on large diameter monopiles is the non-consideration of additional soil reactions as the base shear force ((Bouzid, 2018; Byrne et al., 2017). This work attempts to contribute to this issue with numerical measurements of this force.

The soil reactions acting on a laterally loaded monopile are represented as shear and normal stresses which are mobilized on the contact surfaces between the monopile and the surrounding soil. In accordance, the base shear force reaction S_B is generated by pile base displacements which are able to mobilize shear stresses at the base. This reaction is usually neglected on the analysis of flexible piles (L. C. Reese & Van Impe, 2011), since the latter do not present significant horizontal displacements at the base, and hence, their shear stresses are not mobilized. For piles with rigid or semi-rigid behavior, as the ones studied in the present work, the pile base usually presents non-negligible displacements even at low loading conditions, as seen in Fig. 21 to Fig. 23.

In this work, the base shear force was extracted from the FE simulation results as the integration of the shear stresses generated at the pile base which act on the loading direction. This was done for the 27 simulations that conform the second set of FE simulations. To that end, a coupled Abaqus/Python script was written to extract Abaqus output data concerning the shear stresses and pile displacements at the base. The shear stresses (in this case, values of S23) were extracted from the centroid of half of the finite elements located below the pile and the soil within the pile, taking advantage of the symmetry of the problem, see Fig. 29. The pile lateral displacements at the base (in this case, values of U2) were extracted from four representative nodes as shown in Fig. 30. For each element and node selected from each of the simulations, the script generated a file with the extracted data versus time.

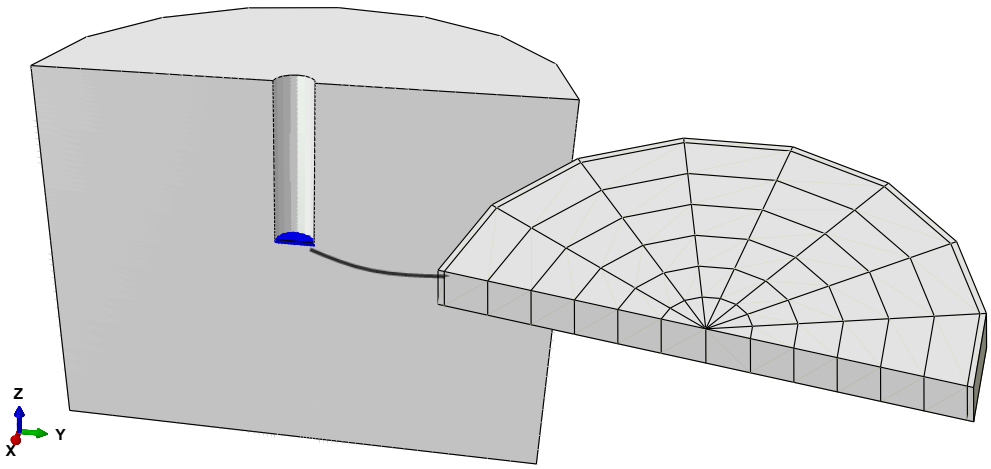

Fig. 29 Selected elements to extract the base shear reaction from the FE simulations.

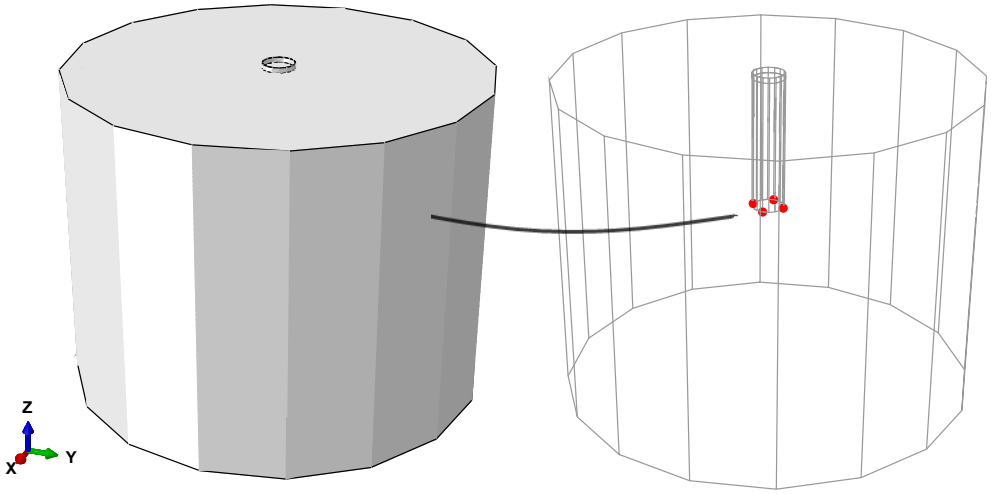

Fig. 30 Selected nodes to extract the pile base displacements from the FE simulations.

A Matlab code was written to process the data and to obtain the base shear force curves for each simulation. The pile displacements at the base y_B were computed as the average of the extracted nodal displacements. The base shear forces S_B were calculated as twice the sum of the individual shear forces mobilized on each of the considered finite elements ($F23_{EL}$) as:

$$S_B = 2 \sum F23_{EL} \tag{36}$$

The shear forces from each element $F23_{EL}$ were computed as:

$$F23_{EL} = S23_{EL}\, A_{EL} \tag{37}$$

where $S23_{EL}$ are the shear stresses extracted from each element and A_{EL} is the area of the face of the finite element located at the contact surface. The area A_{EL} was computed from the coordinates of the vertices of each element face. The results are shown in Fig. 31 and indicate that all models mobilized a non-negligible base shear reaction, which should not be ignored in the analysis and design of monopiles. According to the results, the base shear reaction shows a non-linear behavior with respect to the pile base displacements and shows a dependency on the soil's relative density as well as on the pile geometry.

For analysis purposes, Fig. 32 shows the base shear reaction curves from nine different models with different pile diameters $D = \{5; 6; 7\}$ m and embedment lengths $L = \{20; 25; 30\}$ m and an specific soil's relative density of $D_r = 60\%$. The results indicate that the base shear reaction is greater for the models that exhibit a more rigid behavior (models with lower aspect ratios L/D). For example, as previously seen in Fig. 21, the models with $L = 20$ m present a more rigid behavior. This behavior is also recognized in the results in Fig. 32, where the models with $L = 20$ m present the largest values of mobilized base shear forces.

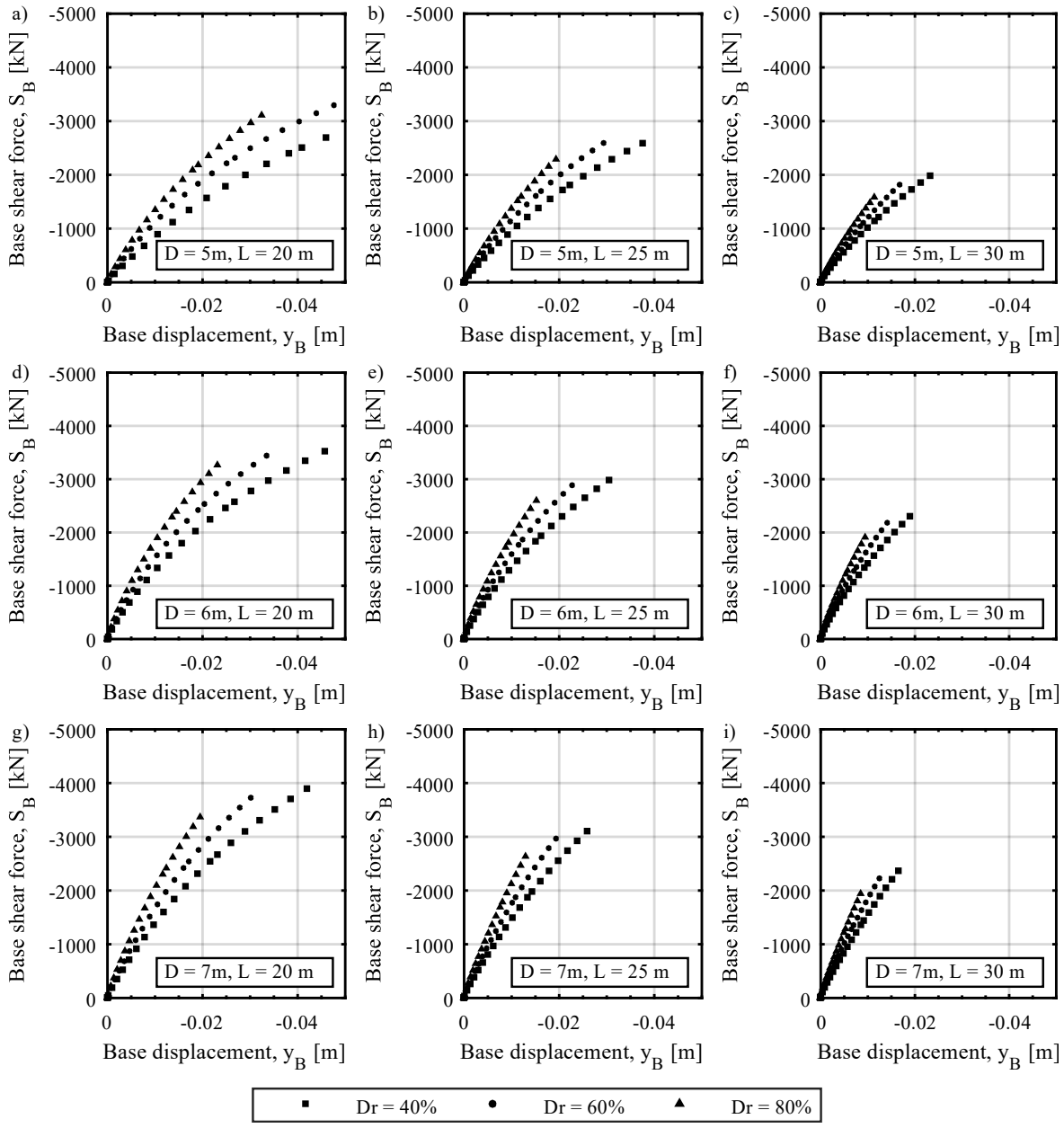

Fig. 31 Measured base shear reaction S_B from FE simulation results. Pile length $L = \{20;\ 25;\ 30\}$ m, pile diameter $D = \{5;\ 6;\ 7\}$ m and relative densities $D_r = \{40\%;\ 60\%;\ 80\%\}$. Karlsruhe fine sand parameters from (Westermann et al., 2014a), see Table 3.

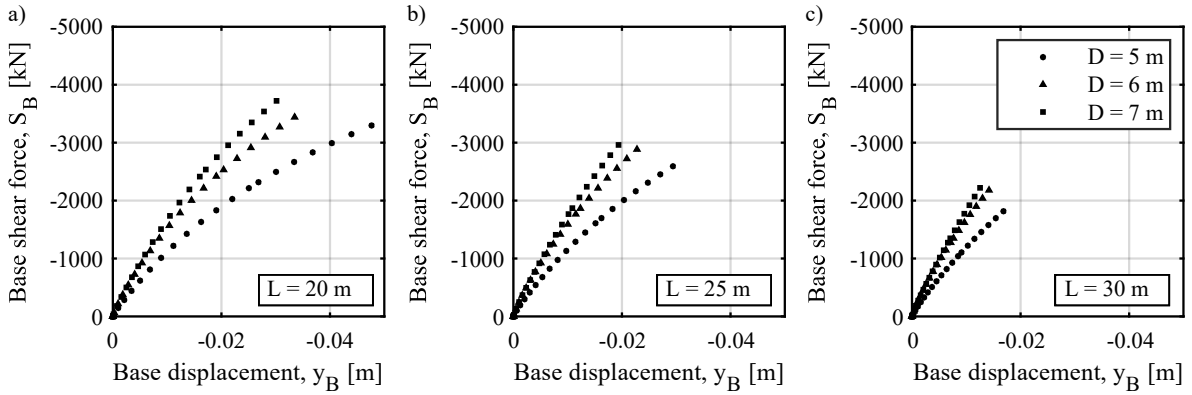

Fig. 32 Measured base shear reaction S_B from FE simulation results. Pile length $L = \{20;\ 25;\ 30\}$ m, pile diameter $D = \{5;\ 6;\ 7\}$ m and relative density $D_r = 60\%$. Karlsruhe fine sand parameters from (Westermann et al., 2014a), see Table 3.

4.3.5. Implications of the 'wished-in-place' approach

In the FE-modelling, the structure was considered as a "wished-in-place" pile. Therefore, from the beginning of the simulation, the pile's elements were introduced into the FE-model. The driving effect was not considered for sake of simplicity; however, it is important to remark how this assumption could affect the results. In the installation of displacement piles, the soil is not removed and is rather displaced vertically and radially while the pile is driven into the soil. This implies two principal consequences. First, the compaction process could increase the mechanical properties of the soil and second, a change of the small displacements field could occur, affecting consequently the stress-strain state.

When referring to the consequences mentioned above considering cohesionless soil compaction due to the pile's driving process, there is a reduction of the air voids between the package of particles composing the soil. The latter results in the increase of the soil's density, thus, the increase of the dry unit weight of the soil and changes in the shear strength. In the constructed FE models, by ignoring the driving effect, an increase of the shear strength of the soil was not considered. This could imply an underestimation of the skin resistance of the pile and lead to a predicted lower skin bearing capacity. However, this is not the topic of concern in this thesis. The concern is that, in the second stage, the stress state after imposing the gravity forces could be different from the one expected to be found in real field conditions due to the compacting process. This may result in overestimated displacements after applying the load, which may directly affect the performance of the p-y model to be proposed in this work, considering that the FE-simulations are used to calibrate the p-y model. Therefore, the predictions from the p-y model could overestimate the real in-situ conditions, due do the errors induced during the calibration process based on the FEM results.

Chapter 5: p-y model for large diameter monopiles in sands

5.1. Generalities

This section provides the formulation and evaluation of a novel p-y model for laterally loaded monopiles under the action of static and long-term cyclic loading. The proposed model considers the pile as a beam in contact with non-linear spring elements along its length, following the BNWF approach, and a spring element at the base to incorporate a base shear force S_B, see Fig. 33. The model considers non-linear relationships for the ultimate soil resistance p_u and the initial subgrade reaction modulus E_{py0} among depth, as well as a factor to account for long-term cyclic loading that depends on the soil's relative density and loading amplitude. The results from the FE simulations presented in the previous section were used to formulate and calibrate the model, along with the results from some FE simulations reported in the literature. Therefore, the proposed model is oriented for the analysis and design of monopiles with diameters between $D = \{5 - 7\}$ m and embedment lengths between $L = \{20 - 30\}$ m, founded in sands.

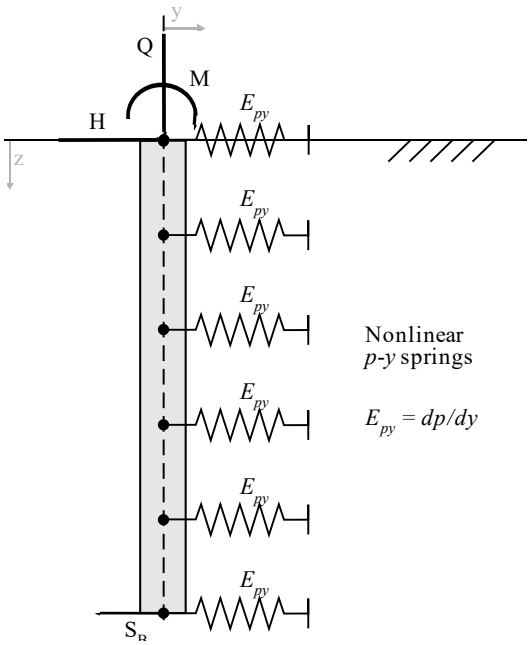

Fig. 33 Sketch of the adopted BNWF approach.

5.2. Formulation of the p-y model

5.2.1. Ultimate soil resistance

The conventional formulations for the ultimate soil resistance p_u exhibit some limitations when applied to large diameter monopiles. For instance, some authors (Bouzid, 2018; W. Li et al., 2017) have argued that the original formulation of p_u as proposed by (Lymon C. Reese et al., 1974), and later adopted with some modifications by (API, 2014a), was developed assuming an specific value of the earth pressure coefficient at rest K_0. The above is not convenient considering that an specific value of K_0 is intrinsically related to an specific state of the soil's relative density, friction angle and overconsolidation ratio. This leads to the conclusion that a formulation of p_u with an improved dependency on the soil's density state may be required.

In addition, the need for a new theoretical background for the formulation of p_u has been discussed by some authors (Bouzid, 2018; Choo & Kim, 2016). The original formulation of p_u by (Lymon C. Reese et al., 1974) assumes two soil failure models, namely a wedge type failure mechanism near the ground surface and a flow-around failure mechanism at greater depths. This concept is fundamentally related to the motion of flexible piles with small diameters, for which it was proposed. According to this formulation, two different equations are used to compute p_u depending on the depth. The particular depth at which the failure mechanisms shift is supposed to correspond to a depth along the pile at which the ultimate soil resistances provided by both equations are equal. However, (Bouzid, 2018) found that for large diameter monopiles, the theoretical shift in the failure concepts according to the

formulation of p_u by (Lymon C. Reese et al., 1974) always occurs well below the base of the pile. This means that when this formulation is applied, only the equation formulated for the wedge type failure mechanism is rendered. The question arises whether this resulting failure mechanism is applicable for large diameter monopiles.

The latter issue is related to the discrepancy between the actual monopile kinematics, and the pile kinematics observed on the experiments which were used to formulate the current p_u models, as discussed by (McGann et al., 2011). Based on their FE simulation analysis, it was concluded that there is a strong influence of the pile kinematics on the resulting p-y curves obtained from back-calculation of the pile deflection curves. Therefore, if one intended to obtain an adequate formulation of the p-y curves (and also, of the p_u distribution) for an specific pile kinematic case, the base data should correspond either to piles exhibiting the same kinematic case or a case in which the pile does not deform and hence does not influence the p-y behavior.

In this sense, some measurements of p_u from numerical and experimental studies that could be used as benchmark for large diameter monopiles are hereafter described. Choo and Kim (Choo & Kim, 2016) extracted experimental p-y curves from centrifuge tests on large diameter monopiles. Although the results did not reach a plateau indicating the values of the ultimate soil resistance p_u, the experimental p-y curves did exhibit a general lower resistance than the curves from API (API, 2014a) and Reese et al. (Lymon C. Reese et al., 1974), suggesting an overestimation of p_u. McGann et al. (McGann et al., 2011) obtained p_u distributions from FE simulations of a deep monopile with embedment length of $L = 30$ m and diameter of $D = 1.37$ m. The mentioned study concluded, that for deep zones $z > 10$ m, the equation by API (API, 2014a) overestimates p_u while other relationships such as the one by Barton (Barton, 1982) (see Eq. (38)) showed a better agreement. However, the p_u distribution presented a non-linear shape among depth, which was not reproduced by any of the studied relationships. Zhang et al. (Zhang et al., 2005) compared different p_u equations (Barton, 1982; J. B. Hansen, 1961; Lymon C. Reese et al., 1974) against measurements of the maximum pressure at the front of different short piles reported in the literature (Adams & Radhakrishna, 1973; Chari & Meyerhof, 1983; Joo, 1985; Meyerhof & Sastry, 1985; Prasad & Chari, 1999), and concluded, that Barton's equation (Barton, 1982) provides more accurate estimations.

Based on the above findings, a new relationship for p_u is presented on this work. To formulate the p_u equation, two main goals were set, namely, to obtain a p_u formulation that i) directly depends on the soil's relative density and ii) exhibits a non-linear distribution among depth. Most studies that have reported empirical relationships for p_u include in their formulations the soil effective stress σ' (or similarly, the depth z) and the pile diameter D (Barton, 1982; Broms, 1964; Fleming et al., 2009; J. B. Hansen, 1961; Lymon C. Reese et

al., 1974). In particular, Barton (Barton, 1982) proposed the following equation depending on the passive earth pressure coefficient K_p:

$$p_u = K_p^2 \sigma' D, \quad \text{with } K_p = \tan^2(45 + \varphi/2) \tag{38}$$

where φ is the peak friction angle which depends on the soil's density. As previously shown, Barton's equation showed a good agreement with FE simulations results (McGann et al., 2011) and experimental results (Zhang et al., 2005). Considering this, the proposed equation was set to adjust to Barton's equation at a particular depth $z = z'$. This allowed for accurate estimations of p_u in accordance to the values reported in (McGann et al., 2011) and showed a satisfactory performance for the FE simulations considered in this work. Moreover, to improve the p_u distribution among depth and enable a direct dependency on the soil's relative density, the proposed p_u was set as proportional to the oedometric (bulk) stiffness of the soil. This is obtained by the following equation:

$$p_u = c_{pu} k^{\text{bulk}} \tag{39}$$

where c_{pu} is a factor responsible to adjust the proposed p_u with Barton's equation at a particular depth $z = z'$, and k^{bulk} is the oedometric bulk stiffness obtained as $k^{\text{bulk}} = \partial \dot{\bar{\sigma}}' / \partial \dot{\varepsilon}_v$, with $\dot{\varepsilon}_v$ being the volumetric strain rate under oedometric conditions.

The oedometric bulk stiffness k^{bulk} is obtained as described below. Following Bauer's equation (Bauer, 1992), under isotropic and oedometric compression, the loosest, critical and densest void ratio curves of a sand are:

$$\frac{e_i}{e_{i0}} = \frac{e_c}{e_{c0}} = \frac{e_d}{e_{d0}} = \exp\left[-\left(\frac{3\,\bar{\sigma}'}{h_s}\right)^{n_B}\right] \tag{40}$$

Where $\bar{\sigma}' = (\sigma' + 2\sigma_x')/3$ is the mean stress, e_i, e_c, e_d denote the loosest ("i"), critical ("c") and densest void ratios ("d"), the constants e_{i0}, e_{c0}, e_{d0} are the loosest, densest and critical void ratios at $\bar{\sigma}' = 0$, and h_s and n_B are fitting parameters. Differentiation of Equation 40 for the loosest condition $e = e_i$ gives:

$$\dot{e} = e_{i0} \exp\left[-\left(\frac{3\,\bar{\sigma}'}{h_s}\right)^{n_B}\right] \left(-n_B \left(\frac{3\,\bar{\sigma}'}{h_s}\right)^{n_B - 1} \left(\frac{3\,\dot{\bar{\sigma}}'}{h_s}\right)\right) \tag{41}$$

Substitution of $e_i = e_{i0} \exp\left[-\left(\frac{3\,\bar{\sigma}'}{h_s}\right)^{n_B}\right]$ and reorganization of the equation gives:

$$\dot{e} = -e_i\, n_B \left(\frac{3\,\bar{\sigma}'}{h_s}\right)^{n_B - 1} \left(\frac{3\,\dot{\bar{\sigma}}'}{h_s}\right) \tag{42}$$

$$\dot{\bar{\sigma}}' = -\left(\frac{3\,\bar{\sigma}'}{h_s}\right)^{1 - n_B} \left(\frac{h_s}{3\, n_B\, e_i}\right) \dot{e} \qquad (\text{for } e = e_i) \tag{43}$$

The bulk modulus k^{bulk}, defined as $k^{\text{bulk}} = \partial\dot{\bar{\sigma}}'/\partial\dot{\varepsilon}_v$ with $\dot{\varepsilon}_v = \dot{e}/(1+e)$, can be deduced from Equation (43) for the condition $e = e_i$:

$$k^{\text{bulk}} = k_0^{\text{bulk}} = \left(\frac{3\,\bar{\sigma}'}{h_s}\right)^{1-n_B} \frac{h_s}{3\,n_B\,e_i}(1+e_i) \qquad (\text{for } e = e_i) \tag{44}$$

Note that $k^{\text{bulk}} = k_0^{\text{bulk}}$ for the state $e = e_i$. For other densities, Bauer (Bauer, 1996) proposed to introduce the density-dependent factor f_e, such that:

$$k^{\text{bulk}} = \frac{f_e}{f_{ei}}\left(\frac{3\,\bar{\sigma}'}{h_s}\right)^{1-n_B} \frac{h_s}{3\,n_B\,e_i}(1+e), \quad \text{with } f_e = \left(\frac{e_c}{e}\right)^{\beta} \text{ and } f_{ei} = \left(\frac{e_{c0}}{e_{i0}}\right)^{\beta} \tag{45}$$

where β is a parameter and f_{ei} has been introduced to keep consistency with $k^{\text{bulk}}|_{e=e_i} = k_0^{\text{bulk}}$. Substitutions of the equations for f_e and f_{ei} in the last equation gives:

$$k^{\text{bulk}} = \left(\frac{e_c \times e_{i0}}{e \times e_{c0}}\right)^{\beta}\left(\frac{3\,\bar{\sigma}'}{h_s}\right)^{1-n_B} \frac{h_s}{3\,n_B\,e_i}(1+e), \tag{46}$$

One may assume that the distribution of the void ratio e with depth is governed by a similar equation to Equation (40) as:

$$e = e_0 \exp\left[\left(\frac{3\,\bar{\sigma}'}{h_s}\right)^{n_B}\right] \tag{47}$$

where e_0 is the void ratio at $z = 0$. Substitution of Equation (47) in Equation (46) gives the resulting equation for the oedometric bulk stiffness:

$$k^{\text{bulk}} = \left(\frac{e_{i0}}{e_0}\right)^{\beta}\left(\frac{3\,\bar{\sigma}'}{h_s}\right)^{1-n_B} \frac{h_s}{3\,n_B\,e_i}(1+e), \tag{48}$$

According to Equation (39), the proposed p_u is adjusted to match Barton's equation (Equation (38)) at a certain depth $z = z'$ and under the loose state $e = e_i$, by means of the factor c_{pu}. Under the loose state $e = e_i$, the soil's friction angle is equal to the critical state friction angle $\varphi = \varphi_c$, and therefore $K_p = K_{p0} = \tan^2(45 + \varphi_c/2)$. Substitution of the aforementioned equations in Equation (39) and using Barton's equation (Equation (38)), gives:

$$c_{pu} = \frac{K_{p0}^2\,\sigma'_{z'}\,D}{k_0^{\text{bulk}}}, \quad \text{with } K_{p0} = \tan^2(45 + \varphi_c/2) \tag{49}$$

where $\sigma'_{z'}$ is the effective stress evaluated at $z = z'$. In this work, a value of $z' = 20$ m has been found to provide accurate estimations for p_u. Substitution of Equation (49) and (44) in Equation (39) gives:

$$p_u = K_{p0}^2 \sigma'_{z'} D \left(\frac{e_{i0}}{e_0}\right)^{\beta} \left(\frac{\bar{\sigma}'}{\bar{\sigma}'_{z'}}\right)^{1-n_B} \frac{(1+e)}{(1+e_i)} \tag{50}$$

Notice that p_u depends on the void ratio e. Considering that $(\bar{\sigma}'/\bar{\sigma}'_{z'}) = (\sigma'/\sigma'_{z'})$ and $(1+e)/(1+e_i) \approx (1+e_0)/(1+e_{i0})$, the following simplified version of Equation (50) is obtained:

$$p_u = K_{p0}^2 \sigma'_{z'} D \left(\frac{e_{i0}}{e_0}\right)^{\beta} \left(\frac{\sigma'}{\sigma'_{z'}}\right)^{1-n_B} \frac{(1+e_0)}{(1+e_{i0})} \tag{51}$$

The void ratio e_0 at $z = 0$ can be determined for a given relative density D_r as:

$$e_0 = e_{c0} - D_r(e_{c0} - e_{d0}) \tag{52}$$

Equations (51) and (52) require definition of the set of parameters $\{\varphi_c, e_{i0}, e_{d0}, n_B, \beta\}$ and the relative density D_r.

The proposed equation is plotted in Fig. 34 against the FE simulation results by McGann et al. (McGann et al., 2011) as well as the equations by Barton (Barton, 1982) and API (API, 2014a). In McGann et al. (McGann et al., 2011) a Mohr-Coulomb model with parameters describing a medium sand ($\varphi = 36°$, $\gamma = 17$ kN/m^3) was used. Considering $\varphi = 36°$ and $D_r = 50\%$, parameter $\beta = 1.24$ was computed as recommended in Section 5.4. Other parameters $\{\varphi_c, e_{i0}, e_{c0}, e_{d0}, n_B\} = \{33.1°,\ 1.212,\ 1.054,\ 0.677,\ 0.32\}$ are borrowed from the Karlsruhe fine sand as an approximation (see Table 3). Fig. 34 shows a satisfactory performance of the proposed p_u equation in comparison to the equations by Barton (Barton, 1982) and API (API, 2014a).

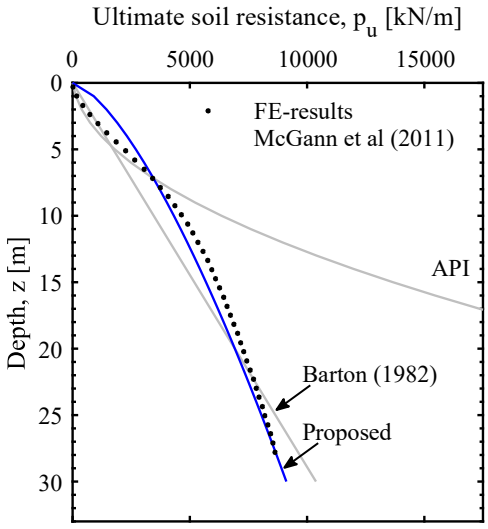

Fig. 34 Proposed ultimate soil resistance p_u against numerical measurements by McGann et al. (McGann et al., 2011) and the proposed equations by API (API, 2014a) and Barton (Barton, 1982).

Fig. 35 compares the proposed equation with Barton's equation for the loose state condition $e = e_i$ where $\varphi = \varphi_c$ and $K_p = K_{p0} = \tan^2(45 + \varphi_c/2)$. The results show that the proposed p_u equation coincides with Barton's equation at the depth $z = z' = 20$ m, as it was intended. For other densities, the p_u relationship varies according to Equation (51). This is shown in Fig. 36 where different D_r distributions are evaluated, namely increasing, decreasing and constant distributions. Note than an almost linear relationship for p_u with z is obtained only for increasing behavior of D_r with depth.

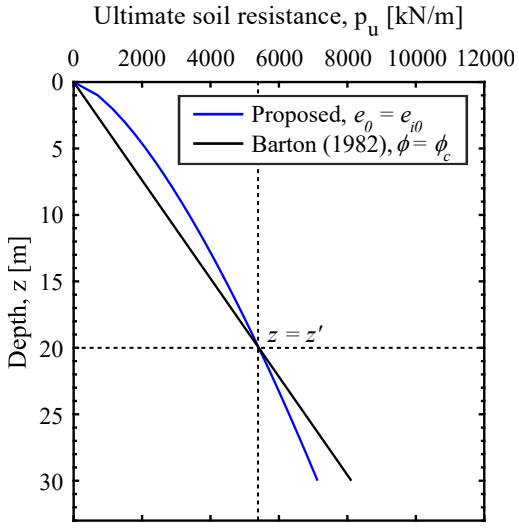

Fig. 35 Proposed ultimate soil resistance p_u against the equation by Barton (Barton, 1982) for the loose state condition $e = e_i$.

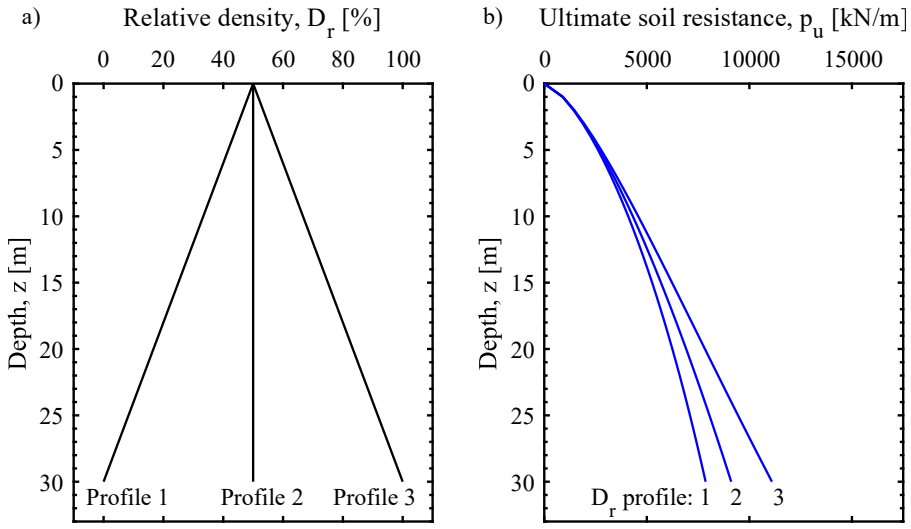

Fig. 36 Influence of the relative density D_r distribution on the proposed ultimate soil resistance p_u.

5.2.2. Soil reaction

As in the conventional p-y method by API (Equation (13) in Section 2.2.2), the lateral soil reaction p was set as proportional to the ultimate soil resistance p_u, a hyperbolic tangent factor and a function for cyclic loading f_A, see Equation (53). The proposed hyperbolic tangent factor is primarily a function of the pile displacement y. Thus, for increasing pile displacements y and under monotonic loading, the proposed soil reaction p reaches the value of p_u and remains unchanged, considering that by definition the hyperbolic tangent function continuously increases from 0 to 1.

However, unlike the API equation, the pile displacements in the proposed hyperbolic tangent argument are raised to an exponent n_y, which is not necessarily equal to 1. This was proposed in order to gain more control over the shape of the relationship between p and y by means of a parameter that could be fixed compared to the FE simulations, such as n_y. Furthermore, considering that p-y curves are related to both soil properties and pile geometry, the proposed hyperbolic tangent argument also includes the pile diameter D and the pile embedment length L. Two additional exponents n_D and n_L, as well as a factor c_p that multiplies the hyperbolic tangent argument, were considered in the formulation in order to allow the fitting of the results of the p-y model to the FE simulations results. Considering the above, the following generalized equation is suggested:

$$p = p_u \tanh[c_p\, |\bar{y}|^{n_y}\, D^{n_D} L^{n_L}]\, f_A\, \mathrm{sign}(\bar{y}), \quad \text{with } \bar{y} = y + y_0 \tag{53}$$

where f_A is a function for cyclic loading and the set $\{c_p, n_y, n_D, n_L, y_0\}$ are proposed parameters which ought to be adjusted using the results from the conducted FE simulations. The set of parameters $\{c_p, n_y, n_D, n_L, y_0\}$ are proposed as fixed parameters within the range of pile geometries and soil conditions considered in this study. For applications outside the studied range of pile geometries and soil conditions, recalibration of the parameters may be required. The operators $\tanh(\cup)$ and $\mathrm{sign}(\cup)$ extract the hyperbolic tangent and the sign of any arbitrary function $\cup$ respectively. Factor $\mathrm{sign}(\bar{y})$ has been introduced to simulate a similar "S-shape" behavior as by the hyperbolic tangent. The constant y_0 has been introduced to control the initial subgrade reaction modulus E_{py0}, as explained below in Section 5.3.3. Factors D^{n_D} and L^{n_L} allow to account for the influence of the pile geometry on the p-y curve.

5.2.3. Initial subgrade reaction modulus

The initial subgrade reaction modulus E_{py0} is obtained from Equation (53) as the differentiation $\partial p/\partial y$ evaluated at $y = 0$ and reads:

$$E_{py0} = \left.\frac{\partial p}{\partial y}\right|_{y=0} = c_p\, n_y\, f_A\, p_u\, D^{n_D} L^{n_L}\, f_{y0}, \quad \text{with } f_{y0} = y_0^{(n_y-1)}\, \mathrm{sech}^2[c_p y_0^{n_y}\, D^{n_D} L^{n_L}] \tag{54}$$

Substitution of Equation (51) in Equation (54) results in:

$$E_{py0} = c_p\, n_y\, f_A \left(K_{p0}^2\, \sigma'_{z'} D \left(\frac{e_{i0}}{e_0}\right)^{\beta} \left(\frac{\sigma'}{\sigma'_{z'}}\right)^{1-n_B} \frac{(1+e_0)}{(1+e_{i0})} \right) D^{(n_D+1)} L^{n_L}\, f_{y0} \tag{55}$$

Note that the proposed initial subgrade reaction modulus E_{py0} directly depends on the p_u profile, see Equation (54). Consequently, the proposed initial subgrade reaction modulus also depends on the soil's relative density and is proportional to the soil's oedometric stiffness k^{bulk} (Equation (48)). This is in accordance with some authors (Kézdi, 1970; Wiemann et al., 2004) that have also related the initial subgrade reaction modulus E_{py0} to the oedometric stiffness k^{bulk}. Moreover, the proposed E_{py0} also depends on the pile diameter D, which has been also confirmed by other works (D. Kallehave et al., 2012; Sørensen et al., 2010; Wiemann et al., 2004).

5.2.4. Base shear reaction

From the analysis of the FE simulations results in Section 4.3, it was concluded that the incorporation of a base shear reaction S_B is necessary for the considered range of pile geometries. In this work, a model is proposed for this reaction and its formulation is presented in this section. Calibration of the proposed mathematical expression using direct measurements from the conducted FE simulations and its comparison with the extracted numerical data is given in Section 5.3 (see Fig. 40).

Some works have proposed S_B formulations in which the base shear reaction is proportional to the self-weight (LeBlanc, Houlsby, et al., 2010), the pile displacement at the base (Burd et al., 2019) and the pile rotation at the base (Gupta & Basu, 2016). In this work, the following relationship is proposed:

$$S_B = S_{B,\max} \tanh(c_s y_B) \tag{56}$$

Where $S_{B,\max}$ is the maximum value for S_B, y_B is the pile lateral displacement at the base and c_s is a constant adjusted to the conducted FE simulations. Similar to (LeBlanc, Houlsby, et al., 2010), $S_{B,\max}$ is computed from the Coulomb theory as:

$$S_{B,\max} = W_t \tan(\varphi_B) \tag{57}$$

where W_t is the resulting vertical force acting at the pile base and φ_B is the peak friction angle at the pile base. The resulting force W_t is obtained as:

$$W_t = \left(Q + W_p - U_L\right) r_s + W_s \tag{58}$$

where Q is the weight of the tower, substructure and nacelle/rotor assembly, W_p is the weight of the pile, W_s is the weight of the soil within the pile, U_L is the resulting hydrostatic force

acting on the pile-soil interface at the pile base and r_s is a load transfer factor defined as the ratio between the sum of vertical forces acting on the pile (including self-weight) and the resulting vertical force transferred to the base of the pile. The forces W_p, W_s and U_L are computed as:

$$W_p = \frac{\pi}{4}\left(D^2 - D_i^2\right) L\, \gamma_p \tag{59}$$

$$W_s = \frac{\pi}{4}\, D_i^2\, L\, \gamma' \tag{60}$$

$$U_L = \frac{\pi}{4}\left(D^2 - D_i^2\right) L\, \gamma_w \tag{61}$$

where D_i is the internal pile diameter and $\gamma' = \gamma_{\text{sat}} - \gamma_w$ is the effective unit weight of the soil within the pile.

The load transfer factor r_s was estimated based on the FE simulations results. To do so, the average effective vertical stress $\sigma_{33_{\text{ave}}}$ acting on the soil elements below the pile and the soil within the pile was obtained. This term could be understood as the resulting vertical force acting at the pile base W_t divided by the cross-sectional area $A = \pi\, D^2/4$. This is expressed by the following equation:

$$\sigma_{33_{ave}} = \frac{W_t}{A} = \frac{\left(Q + W_p - U_L\right) r_s + W_s}{\pi\, D^2/4} \tag{62}$$

Substitutions of Equation 59 in Equation 62 and rearrangement of the latter gives the following equation for the load transfer factor r_s:

$$r_s = \frac{\left(\sigma_{33_{\text{ave}}} - \gamma' L\, D_i^2/D^2\right)\pi\, D^2/4}{Q + W_p - U_L} \tag{63}$$

The values of $\sigma_{33_{\text{ave}}}$ were computed following a similar methodology as the one adopted in Section 4.3.4. First, a coupled Abaqus/Python script was written to extract the vertical stresses at the base of the pile. For this, the total vertical stresses (in this case, values of S33) were extracted at the centroid of half of the finite elements located below the pile and the soil within the pile, taking advantage of the symmetry of the problem. This was done for the 27 simulations from the second set of FE simulations. A file was obtained for each considered element, from each of the simulations, containing the vertical stresses extracted from the element, denoted as $S33_{EL}$. Afterwards, a Matlab code was used to process the data. First, the individual vertical forces acting on each of the considered finite elements, denoted as $F33_{EL}$, were computed as:

$$F33_{EL} = \left(S33_{EL} - U_{z=L}\right) A_{EL} \tag{64}$$

where $U_{z=L}$ is the pore water pressure at a depth of $z = L$ and A_{EL} is the area of the face of the finite element located at the contact surface. Then, the values of $\sigma_{33_{\text{ave}}}$ were obtained as:

$$\sigma_{33_{\text{ave}}} = \frac{2 \sum F33_{EL}}{\pi D^2/4} \tag{65}$$

Finally, the load transfer factor r_s was evaluated following Equation 63. The results are shown in Fig. 37 for the time interval $t = [1 - 3.5]$ s. Fig. 37.a shows the computed values of $\sigma_{33_{\text{ave}}}$ and Fig. 37.b presents the computed values of r_s. The results show that a factor r_s could be assumed constant among the different pile geometries studied (D = $\{5 - 7\}$ m, L = $\{20 - 30\}$ m) with a value of $r_s \approx 0.3$.

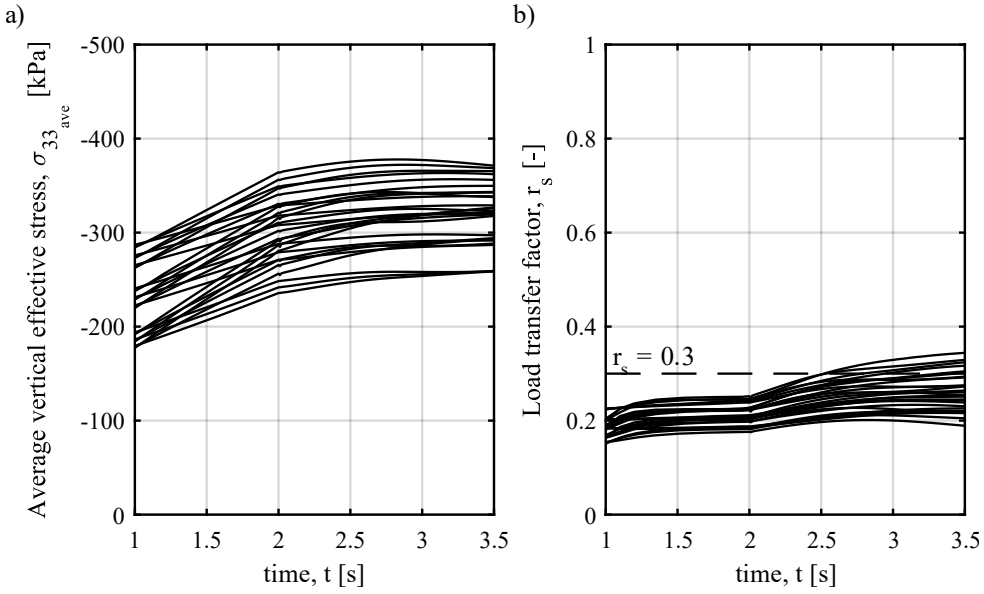

Fig. 37 Computed average vertical effective stress $\sigma_{33_{\text{ave}}}$ and load transfer factor r_s FE simulations results.

5.2.5. Cyclic loading factor

A cyclic loading factor f_A is proposed in this work to account for the effect of long-term cyclic loading on the monopile displacement, see Equation (53). To propose a relationship for f_A, a simplification of the complex offshore environmental loading conditions is adopted. As commonly done, the cyclic loading is simplified as representative load parcels with a constant amplitude and an average value. This is schematized in Fig. 38, where M_{ave} and H_{ave} are the average values for the moment and lateral loading and M_{amp} and H_{amp} are their corresponding amplitudes. As also shown in Fig. 38, for the adopted convention, $N = 1$ means monotonic loading while $N > 1$ means cyclic loading.

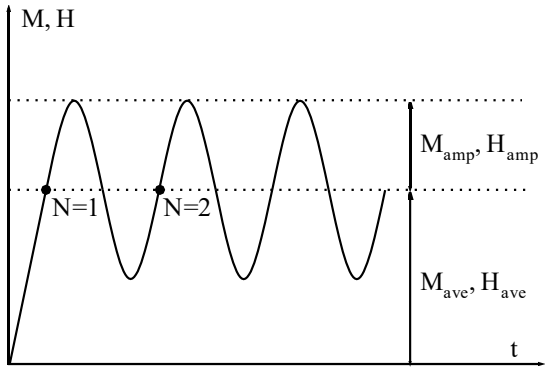

Fig. 38 Sketch of average values and amplitudes of the moment M and horizontal force H.

In this work, a Soil Resistance Degradation (SRD) approach was adopted. To do so, factor f_A is included on the formulation of the p-y curve for cyclic loading to reduce the soil resistance p as the number of loading cycles N increases. This allows to simulate a degradation of the p-y stiffness due to cyclic loading, by means of which the accumulated response is obtained. For monotonic loading, factor f_A is set to $f_A = 1$. Therefore, factor f_A is bounded between 0 and 1, where $f_A = 1$ indicates no accumulation of displacements (monotonic loading) and $f_A = 0$ indicates the maximum degradation state caused by cyclic loading.

Factor f_A is introduced in order to account for the effects of the different variables that influence the accumulation of displacements of monopiles under cyclic loading. For this, a useful theoretical framework is the conclusions by Wichtmann (Wichtmann, 2005), which indicate that the accumulated strains of a soil under cyclic loading depend on the number of cycles N, the stress/strain amplitude, density, stress ratio $\eta = q/\bar{\sigma}$, where q and $\bar{\sigma}$ are the deviator and mean effective stress respectively, load polarization and others. The proposed relationship for f_A intended to incorporate some of those effects while still keeping some level of simplicity for the model. To do so, six principal variables affecting the accumulation response of monopiles were selected to be included in the f_A equation, namely i) the number of loading cycles N, ii) the average moment M_{ave} and moment amplitude M_{amp}, to account for the effects of the stress/strain amplitude, iii) the soil relative density D_r, to account for density effects, iv) the ultimate soil resistance ratio ($\xi \approx p/p_u$), to account for the effects of the stress ratio, and v) the depth z, to account for the effects of confinement.

A general mathematical expression is proposed to satisfy the established constraints for f_A ($f_A \in [0, 1]$) and to consider the variables of interest. An expression of the type $f(x) = 1 - e^{-x}$ is suitable for this purpose considering that the negative exponential function $f(x) = e^{-x}$ takes values between 1 and 0 in the positive range of x. Considering this, the proposed general expression for f_A reads:

$$f_A = 1 - \exp\left[-\frac{c_N f_z f_M}{f_{D_r} f_\xi}\right] f_N \tag{66}$$

Where f_z, f_M, f_{D_r}, f_ξ and f_N are functions of the considered variables of interest and c_N is a model parameter. Function f_z accounts for the effects of confinement by means of a normalized depth, as:

$$f_z = \left(\frac{z}{D}\right) \tag{67}$$

Note that for increasing depths, function f_z gives larger values which translates into a larger f_A factor and less accumulation of displacements at these depths.

Function f_M incorporates the ratio between the average moment M_{ave} and the moment amplitude M_{amp} as:

$$f_M = \left(\frac{M_{\text{ave}}}{M_{\text{amp}}}\right)^{n_M} \tag{68}$$

where n_M is a model parameter. Note that for a given average moment, function f_M gives smaller values for increasing moment amplitudes, which translates into a smaller f_A factor and larger accumulation of displacements for larger moment amplitudes.

Function f_{D_r} is proposed as a density dependent function as:

$$f_{D_r} = (1.15 - D_r)^{n_{D_r}} \tag{69}$$

where n_{D_r} is a model parameter and D_r is the soil's relative density. Following the proposed expression, greater soil densities result in smaller values of f_{D_r} which translates into a larger f_A factor and less accumulation of displacements for these densities. Note that even for very dense soils with $D_r \approx 1.00$, there is still an accumulation of displacements due to cyclic loading, as previously shown in the field tests by (W. Li et al., 2015).

Function f_ξ addresses the effects of the stress ratio $\eta = q/\bar{\sigma}$ by incorporating a similar ultimate soil resistance ratio ($\xi \approx p/p_u$) as:

$$f_\xi = \left(1 + \alpha_p \xi\right)^{n_\xi} \tag{70}$$

where $\xi = \tanh[c_p\, |\bar{y}|^{n_y}\, D^{n_D} L^{n_L}]$ is the ultimate soil resistance ratio ($\approx p/p_u$) assuming monotonic loading conditions, see Equation (53), and α_p and n_ξ are model parameters. Following the proposed expression, larger accumulation of displacements is expected for greater values of the ultimate soil resistance ratio.

Finally, function f_N accounts for a logarithmic trend of the relation between the displacements accumulation and the loading cycles N. The proposed function reads:

$$f_N = \left[\frac{\log N}{\log \widehat{N}}\right]^{n_N} \tag{71}$$

where $\widehat{N}$ is the number of cycles needed to reach the maximum degradation state $f_A = 0$ at the groundline. For monotonic loading ($N = 1$), function $f_N = 0$ which results in factor $f_A = 1$ and no accumulation of pile displacements. For increasing values of N until reaching the maximum value $\widehat{N}$, function f_N increases from 0 to 1, resulting in a continuous increase of the accumulation of displacements with N.

Taking into consideration the above mentioned functions, the following equation is proposed for f_A:

$$f_A = \begin{cases} 1 & \text{, monotonic loading} \\ 1 - \exp\left[\dfrac{-c_N(z/D)\left(M_{\text{ave}}/M_{\text{amp}}\right)^{n_M}}{f_{D_r}\left(1+\alpha_p\xi\right)^{n_\xi}}\right]\left[\dfrac{\log N}{\log \widehat{N}}\right]^{n_N} & \text{, cyclic loading with } N \le \widehat{N} \\ 0 & \text{, cyclic loading with } N > \widehat{N} \end{cases} \tag{72}$$

where the set $\{c_N, \alpha_p, n_N, n_M, n_\xi, \widehat{N}\}$ are proposed parameters which ought to be adjusted. Fig. 39 presents the proposed cyclic factor for a 6-m diameter monopile embedded in fine sand (parameters in Table 3), assuming $M_{\text{ave}} = 30$ MPa, $M_{\text{amp}} = 10$ MPa, $D_r = 60\%$,and $y = 0$, i.e., $\xi = 0$.

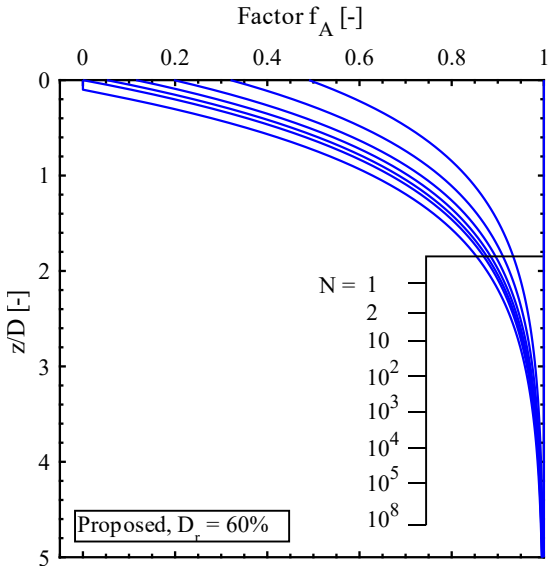

Fig. 39 Proposed cyclic loading factor. For this example, $D_r = 60\%$ and $M_{\text{ave}}/M_{\text{amp}} = 3$.

5.3. Calibration and evaluation of the p-y model

5.3.1. Methodology

The required parameters are divided into the following groups: for static analysis $\{c_p, c_s, n_y, n_D, n_L, y_0, r_s, \varphi_c, e_{d0}, e_{c0}, e_{i0}, D_r, \beta, n_B\}$ and for long-term cyclic loading conditions $\{c_N, \alpha_p, n_N, n_M, n_{D_r}, n_\xi, \widehat{N}\}$. From the group for static analysis, the set of parameters $\{\varphi_c, e_{d0}, e_{c0}, e_{i0}, D_r, \beta, n_B\}$ depend on the particular site conditions and can be found in Table 3 for the considered sands in this work. The rest of parameters, which are the set $\{c_p, c_s, n_y, n_D, n_L, y_0, r_s\}$ for static analysis and the set $\{c_N, \alpha_p, n_N, n_M, n_{D_r}, n_\xi, \widehat{N}\}$ for cyclic loading conditions are proposed as fixed values or functions which are calibrated to provide the best accuracy within the range of studied pile geometries and soils. The set of "fixed" parameters were calibrated using the results from the conducted FE simulations (See Section 4.3), as well as the results from some works in the literature. Systematic variations of each of these parameter were performed to obtain an accurate response as shown below.

5.3.2. Base shear reaction

Two parameters are used on the proposed relationship for the base shear reaction S_B (Equations (56)-(58)), namely parameters r_s and c_s. As shown in Section 5.2.4, based on numerical measurements from the conducted FE simulations, it was found that an appropriate value for the load transfer factor r_s was $r_s = 0.3$. On the other hand, measurements of the base shear reaction (see Section 4.3.4) from the conducted FE simulations were used to calibrate parameter c_s using the proposed equation from Equation (56). To do so, the peak friction angle at the base φ_B was computed by equaling Equations (38) and (51), and assuming $\sigma' = \sigma'_{z'}$, as:

$$\varphi_B = 2\arctan\left[\left(\left(\frac{e_{i0}}{e_0}\right)^{\beta}\frac{1+e_0}{1+e_{i0}}K_{p0}^2\right)^{1/4}\right] - 90° \tag{73}$$

Evaluating different values for c_s, it was found that a value of $c_s = 19$ provided an accurate estimation of S_B, as shown in Fig. 40.

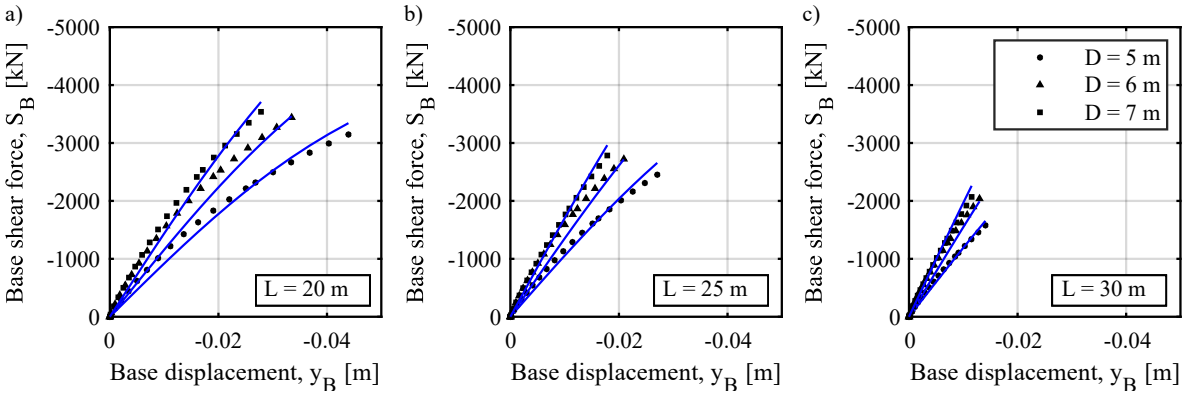

Fig. 40 Base shear reaction predicted by the proposed model and compared to FE simulations. Pile length $L = \{20; 25;\ 30\}$ m, pile diameter $D = \{5;\ 6;\ 7\}$ m and relative density $D_r = 60\%$. Karlsruhe fine sand parameters from (Westermann et al., 2014a), see Table 3.

5.3.3. Static analysis

The deflection curves and load-displacement curves obtained from the FE simulations results (see Section 4.3), were used to calibrate parameters $\{c_p, n_y, n_D, n_L\}$ for the considered range of studied pile geometries and soils. Systematic variations of each of the parameters were performed to optimize the model performance. Satisfactory results were obtained when setting parameters $\{n_y, n_D, n_L\}$ as $\{0.68, -0.35, -0.60\}$, and incorporating the influence of the soil material by setting parameter c_p as a function of β through the equation $c_p = 22.4/\beta^{1.2}$. Parameter y_0 was set to a very small value of $y_0 = 8 \times 10^{-7}$ to provide good estimations of E_{py0}, as explained later.

Simulations were conducted with the proposed model for the cases considered on the FE simulations in Section 4.3. Parameters $\{\varphi_c, e_{d0}, e_{c0}, e_{i0}, D_r, \beta, n_B\}$ used in the proposed model were defined according to Table 3. The deflection curves obtained from the first set of FE simulations results are compared to the ones predicted by the proposed model in Fig. 41 to Fig. 43. The load deflection curves from the second and third set of FE simulations are compared to the ones predicted by the proposed model in Fig. 44 and Fig. 45 respectively. In all cases, the simulations with the proposed model show a satisfactory agreement with the FE simulations results.

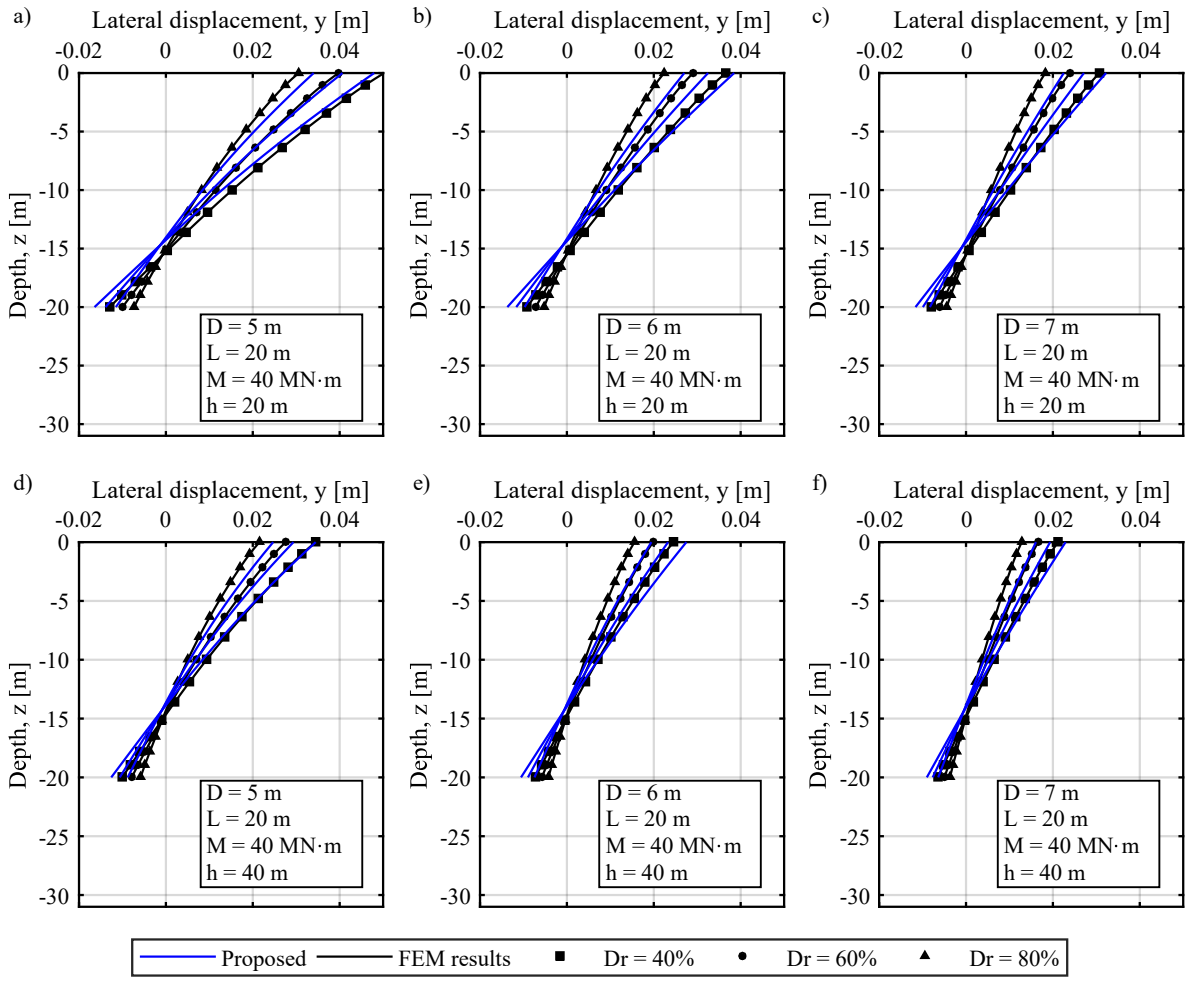

Fig. 41 Pile deflection curves under static loading predicted by the proposed model and compared to FE simulations. Pile length $L = 20$ m, pile diameter $D = \{5;\ 6;\ 7\}$ m and relative densities $D_r = \{40\%;\ 60\%;\ 80\%\}$. Karlsruhe fine sand parameters from (Westermann et al., 2014a)Fig. 40, see Table 3.

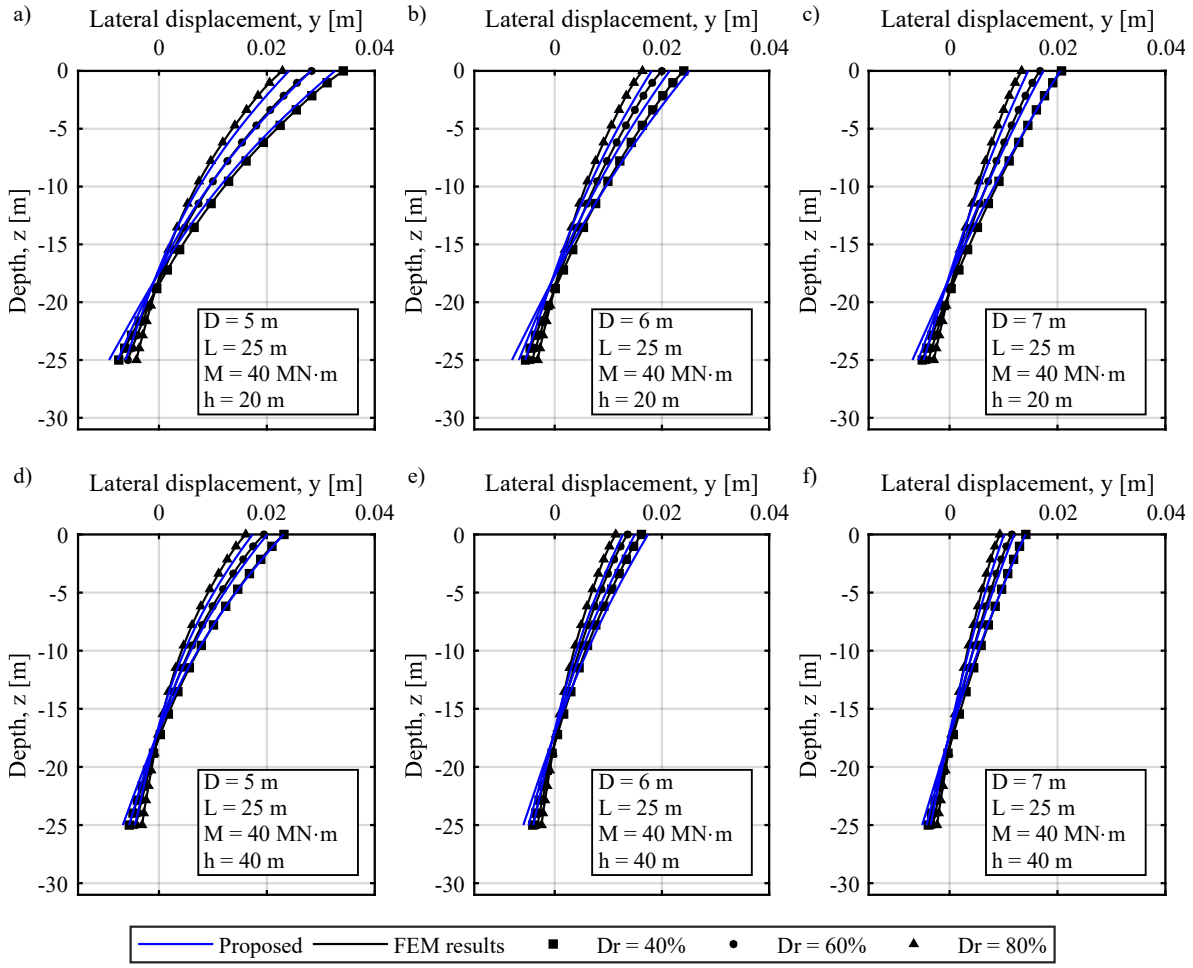

Fig. 42 Pile deflection curves under static loading predicted by the proposed model and compared to FE simulations. Pile length $L = 25$ m, pile diameter $D = \{5;\ 6;\ 7\}$ m and relative densities $D_r = \{40\%;\ 60\%;\ 80\%\}$. Karlsruhe fine sand parameters from (Westermann et al., 2014a), see Table 3.

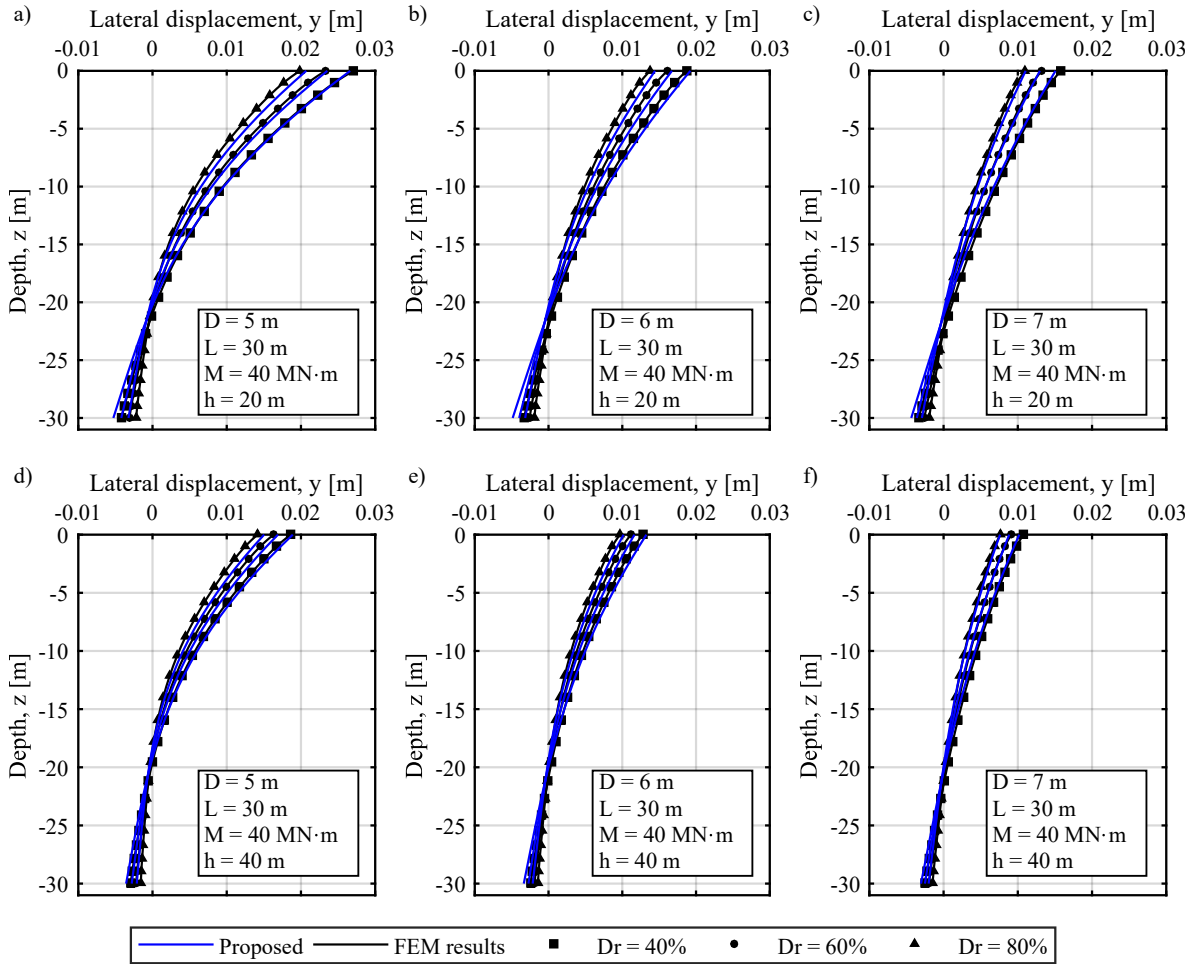

Fig. 43 Pile deflection curves under static loading predicted by the proposed model and compared to FE simulations. Pile length $L = 30$ m, pile diameter $D = \{5;\ 6;\ 7\}$ m and relative densities $D_r = \{40\%;\ 60\%;\ 80\%\}$. Karlsruhe fine sand parameters from (Westermann et al., 2014a), see Table 3.

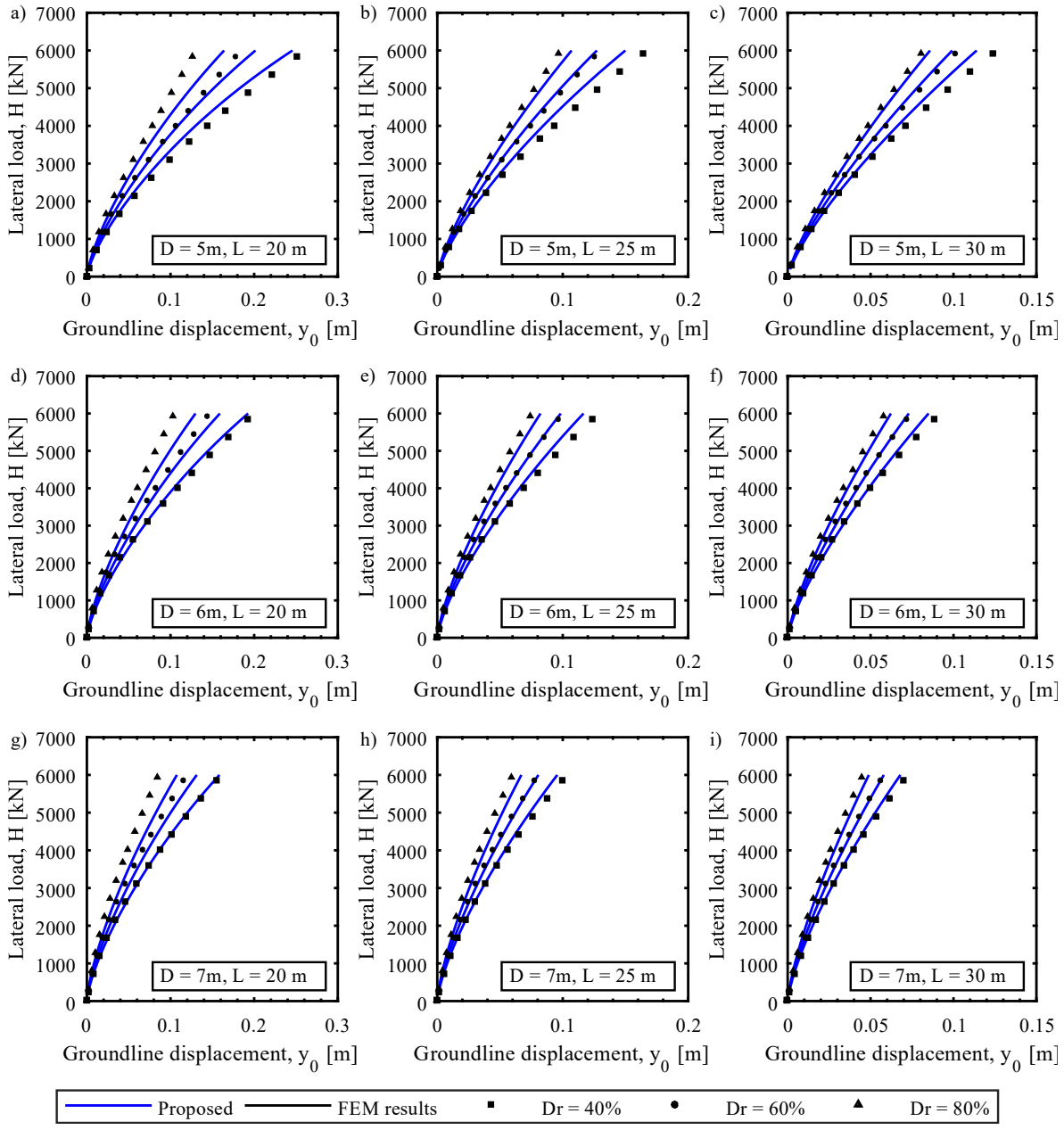

Fig. 44 Load-deflection curves under static loading at ground level predicted by the proposed model and compared to FE simulations. Pile length $L = \{20; 25;\ 30\}$ m, pile diameter $D = \{5;\ 6;\ 7\}$ m and relative densities $D_r = \{40\%;\ 60\%;\ 80\%\}$. Karlsruhe fine sand parameters from (Westermann et al., 2014a), see Table 3.

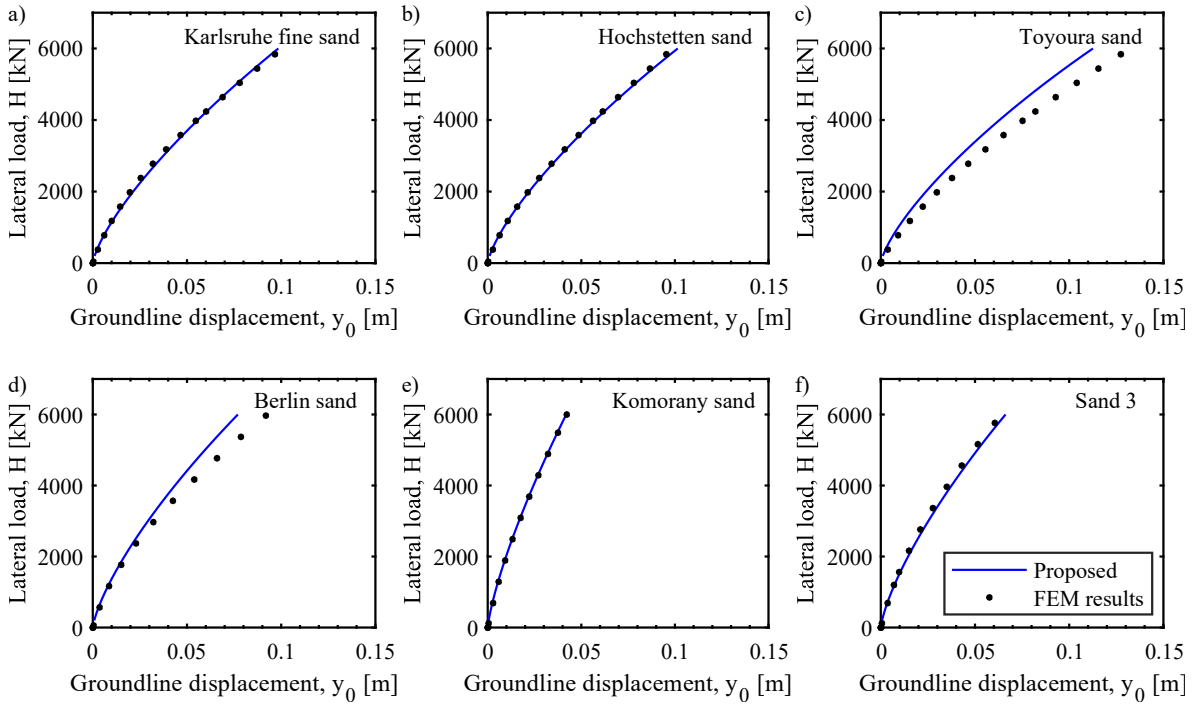

Fig. 45 Load-deflection curves under static loading at ground level for different sands predicted by the proposed model and compared to FE simulations. Pile length $L = 25$ m, pile diameter $D = 6$ m and relative density $D_r = 60\%$. See Table 3 for material parameters.

Setting parameter $y_0 = 8 \times 10^{-7}$ provides estimations of the initial subgrade reaction modulus E_{py0} in the range of proposed relationships in the literature as the one by Kallehave et al. (D. Kallehave et al., 2012). The latter has been proven as a suitable relationship for large diameter monopiles (Martin Achmus et al., 2019). This is shown in Fig. 46, where the resulting E_{py0} from Equation (55) is compared with the one by Kallehave et al. (D. Kallehave et al., 2012) and API (API, 2014a). For this example, parameters of the Karlsruhe fine sand were adopted considering a relative density of $D_r = 60\%$, see Section 4.2.2, and two pile diameters were considered, namely $D = \{1; 6\}$ m. The results indicate that, unlike the API equation, the proposed equation presents a non-linear distribution among depth as the one by Kallehave (D. Kallehave et al., 2012). A dependency on the pile diameter is also shown in Fig. 46. The proposed equation and the one by Kallehave (D. Kallehave et al., 2012) show different values depending on the pile diameter, which is not the case with the equation by API. Following Equation (55), the proposed E_{py0} depends on the pile diameter due to factor $D^{(n_D+1)} = D^{0.65}$. The term $\text{sech}^2[c_p y_0^{n_y} D^{n_D} L^{n_L}]$ includes also D. However, this term is approximately one due to $y_0 \approx 0$. This factor can be compared to the relationships reported by Kallehave et al. (D. Kallehave et al., 2012) or Sørensen et al. (Sørensen et al., 2010), whereby $E_{py0} \sim D^{0.5}$.

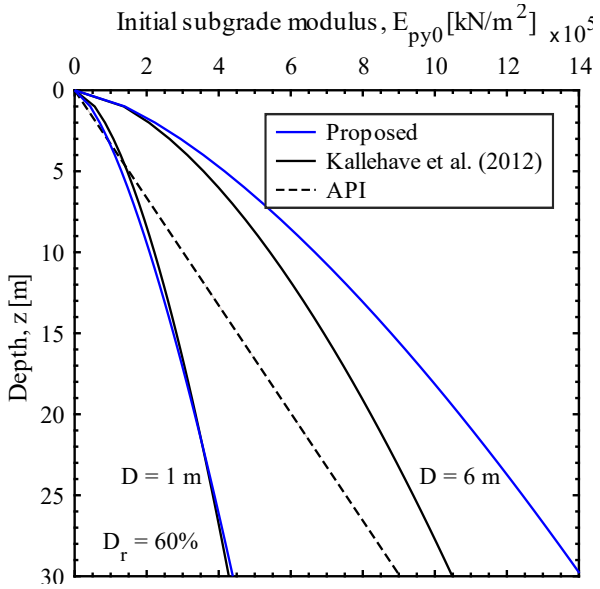

Fig. 46 Proposed initial subgrade reaction modulus E_{py0} against the proposed relationships by (API, 2014a) and (D. Kallehave et al., 2012).

5.3.4. Cyclic behavior

The set of parameters for long-term cyclic lateral loading conditions $\{c_N, \alpha_p, n_N, n_M, n_{D_r}, n_\xi, \widehat{N}\}$ was defined as follows. The number of loading cycles needed to reach the maximum degradation state $\widehat{N}$ was set as $\widehat{N} = 10^5$ following the conclusions from (Dührkop, 2009). Considering that simulation of long-term cyclic loading conditions was outside of the scope of this study, the set of parameters $\{c_N, \alpha_p, n_N, n_M, n_{D_r}, n_\xi\}$ was calibrated using the results from different FE problems found in the literature, namely (Wichtmann et al., 2008), (Westermann et al., 2014b) and (Staubach & Wichtmann, 2020). The selected studies performed FE simulations of monopiles subjected to long-term loading conditions with a large number of cycles and considered variations of the moment amplitude M_{amp}, average moment M_{ave} and relative density D_r. To simulate the long-term response of the soil, the High Cycle Accumulation (HCA) model (Niemunis et al., 2005) was employed by the mentioned studies, as well as a careful calibration of the HCA model with a set of cyclic triaxial tests results (Wichtmann, 2005).

Simulations with the proposed model were conducted and compared to the FE simulations results from the mentioned studies while considering variations of parameters $\{c_N, \alpha_p, n_N, n_M, n_{D_r}, n_\xi\}$. To do so, the set of model parameters for static loading $\{c_p, n_y, n_D, n_L, y_0\}$ was set as defined above and parameters $\{\varphi_c, e_{d0}, e_{c0}, e_{i0}, D_r, \beta, n_B\}$ used in the proposed model were directly taken from the mentioned studies. Note that the HCA model selected for the FE simulations in (Wichtmann et al., 2008), (Westermann et al., 2014b) and (Staubach & Wichtmann, 2020) incorporates the IS-Hypoplastic model and

therefore parameters $\{\varphi_c, e_{d0}, e_{c0}, e_{i0}, D_r, \beta, n_B\}$ are given. After the calibration process, the set of model parameters for cyclic loading was set as $\{c_N, \alpha_p, n_N, n_M, n_{D_r}, n_\xi, \widehat{N}\} = \{0.33, 23, 0.24, 0.88, 0.40, 0.68\}$ with satisfactory results. The description of each of the mentioned studies and comparison with the proposed model are given below.

Wichtmann et al. (Wichtmann et al., 2008) conducted FE calculations of a monopile with a diameter of $D = 5.09$ m and an embedment length of $L = 29.65$ m embedded in a fine sand. The deflection curves of the monopile due to different cyclic loading conditions were evaluated. Fig. 47 and Fig. 48 show the reported FE simulations results considered in this study. Fig. 47 shows the deflection curves for several values of N and Fig. 48 shows the groundline displacements against values of N. As shown, different average moments $M_{\text{ave}} = \{20;\ 30;\ 40\}$ MN·m, moment amplitudes $M_{\text{amp}} = \{10;\ 15;\ 20\}$ MN·m and number of loading cycles up to $N = 10^6$ were analyzed. The material constants for the fine sand are found in (Wichtmann, 2005), under the name of 'CFS sand (OV)'. The pile wall thickness and Young's modulus of the pile material were reported as $t_p = 0.045$ m and $E = 210$ GPa. A single load eccentricity was considered by keeping the ratio H/M as $H/M = 0.027\ 1/\text{m}$ for all simulations. Additionally, a vertical load $Q = 9247$ kN was applied at the top of the monopile.

For the proposed model, the set of parameters $\{\varphi_c, e_{d0}, e_{c0}, e_{i0}, \beta, n_B\}$ for the 'CFS sand (OV)' were set as $\{32.8, 0.575, 0.908, 1.044, 1.6, 0.30\}$ according to (Wichtmann, 2005). The relative density D_r increased linearly with depth from 50% at the groundline to 90% at $z = 30$ m according to (Wichtmann et al., 2008) (see Fig. 47.f). The effective unit weight of the soil was evaluated at a depth of $z = L/2$ and gave $\gamma' = 9.9$ kN/m^3. The predictions of the proposed model are shown along the reported FE simulations results in Fig. 47 and Fig. 48. The performance of the proposed model is satisfactory. The dependence on the average moments and moment amplitudes could be addressed by the proposed f_A equation (Equation (72)). However, the accumulation of displacements for a number of loading cycles greater than $N > 10^5$ was not captured by the proposed model. The FE simulations results show an acceleration of the displacements accumulation after such number of load cycles. In contrast, the proposed model was developed to display a decreasing rate of displacement accumulation as the number of loading cycles increases.

Westermann et al. (Westermann et al., 2014a) conducted FE calculations of a monopile with a diameter of $D = 5$ m, an embedment length of $L = 30$ m under cyclic loading with $N = 10^5$. The monopile was embedded in a fine sand. The reported numerical results considered on this study are shown in Fig. 49. Different average moments $M_{\text{ave}} = \{10; 20;\ 30;\ 50\}$ MN·m, moment amplitudes $M_{\text{amp}} = \{10; 20; 30\}$ MN·m and loading eccentricities $h = \{20; 40\}$ m were evaluated. The material constants for the fine sand are found in (Westermann et al., 2014a). The pile wall thickness and Young's modulus of the pile material

were reported as $E = 210$ GPa and $t_p = 0.06$ m respectively. A vertical load was applied at the top of the monopile representing the weight of the OWT. A value of $Q = 8680$ kN was assumed as representative of the weight of the OWT, as used in Section 4.2.5. Simulations with the proposed model were performed with $\{\varphi_c, e_{d0}, e_{c0}, e_{i0}, \beta, n_B\} = \{33.1°, 0.677, 1.054, \ 1.212, 2.5, 0.27\}$ and $\gamma' = 9.03$ kN/m^3 as reported by (Westermann et al., 2014a). The results are compared to the reported FE simulations results in Fig. 49, where a satisfactory agreement is observed. The dependence on the average moments, moment amplitudes and load eccentricities could be simulated by the proposed model.

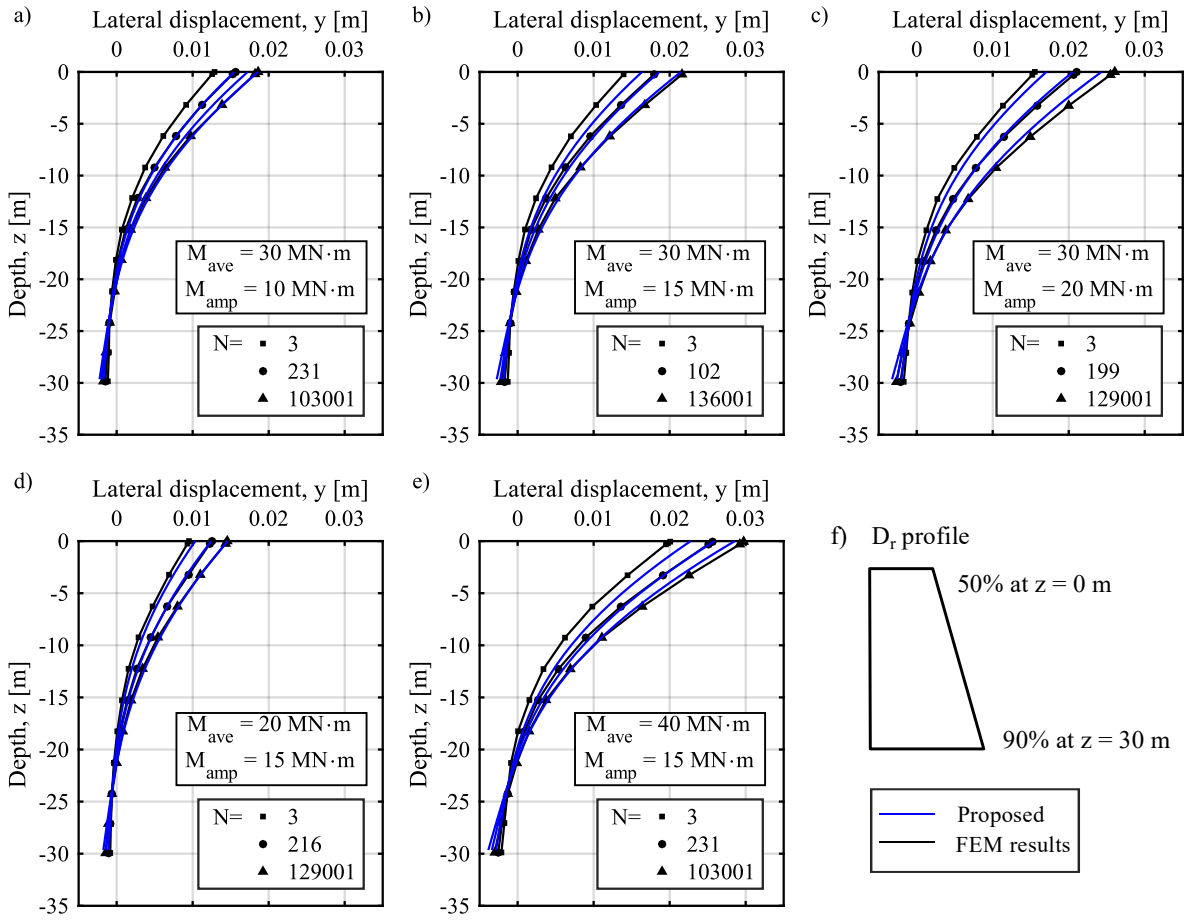

Fig. 47 Long-term pile deflection curves under cyclic loading for different number of loading cycles N predicted by the proposed model and compared to FE simulations by (Wichtmann et al., 2008). Pile length $L = 29.65$ m, pile diameter $D = 5.09$ m and relative density linearly variable with depth.

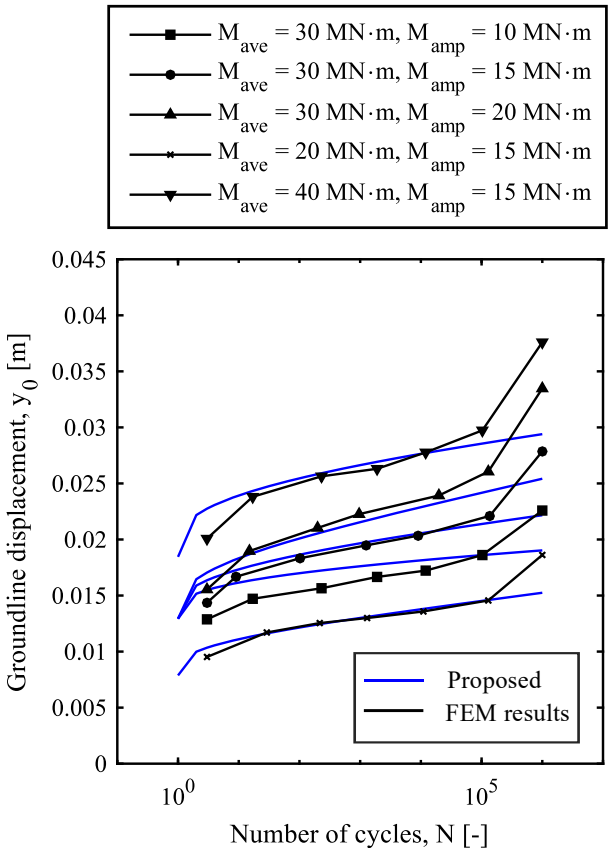

Fig. 48 Pile deflection at ground level against number of loading cycles N predicted by the proposed model and compared to FE simulations by (Wichtmann et al., 2008). Pile length $L = 29.65$ m, pile diameter $D = 5.09$ m and relative density linearly variable with depth.

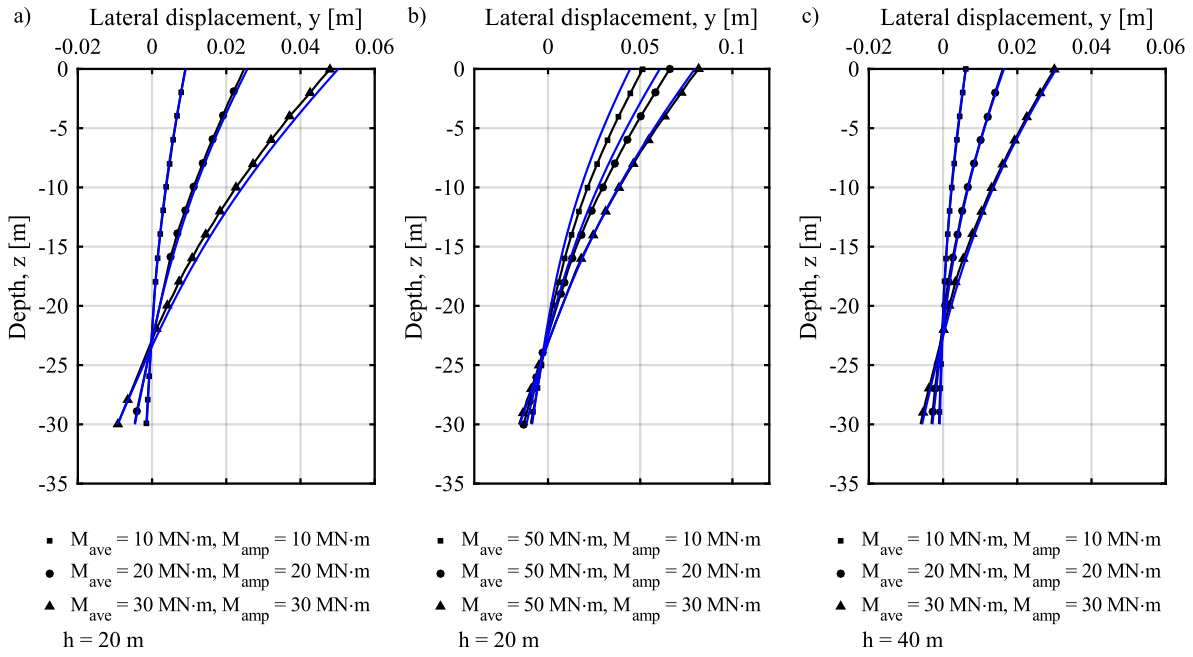

Fig. 49 Pile deflection curves under cyclic loading for a number of loading cycles of $N = 10^5$ predicted by the proposed model and compared to FE simulations by (Westermann et al., 2014b). Pile length $L = 30$ m, pile diameter $D = 5$ m and relative density $D_r = 60\%$.

Staubach and Wichtmann (Staubach & Wichtmann, 2020) evaluated the influence of different packages of load cycles on the pile response. For this, simulations of a steel monopile with $D = 5$ m and $L = 30$ m subjected to three different loading histories (see Fig. 51.a) with multi-amplitude cyclic loading were reported. In this case, multi-amplitude cyclic loading consists of the application of successive packages of load cycles with a constant load amplitude within each package. The monopile was embedded in a fine sand with a relative density of $D_r = 60\%$. The pile wall thickness was $t_p = 0.08$ m.

Four load packages were considered in this study. Each load package has a constant moment amplitude $M_{\mathrm{amp}} = \{40; 50; 60; 30\}$ MN·m. All load packages had the same average moment $M_{\mathrm{ave}} = 30$ MN·m, number of load cycles $N = 25000$ and height of the load application point above the groundline $h = 30$ m. Three different loading histories were evaluated by arranging the mentioned packages in different sequences, as shown in Fig. 51.a. In the first loading history, the moment amplitudes were arranged as $M_{\mathrm{amp}} = \{30; 40; 50; 60\}$ MN·m. In the second loading history, the sequence was set as $M_{\mathrm{amp}} = \{40; 50; 60; 30\}$ MN·m. Finally, in the third loading history, the sequence $M_{\mathrm{amp}} = \{60; 50; 40; 30\}$ MN·m was considered. A vertical load Q was applied at the top of the monopile to account for the weight of the OWT. As previously done, the load was assumed as $Q = 8680$ kN, which is a representative value of the weight of the OWT.

To simulate multi-amplitude cyclic loading using the proposed model, the Miner's rule approach was adopted (LeBlanc, Byrne, et al., 2010; W. Li et al., 2015; Miner & others, 1945). According to this method, the pile displacement (or rotation) after a sequence of load packages with different amplitude is independent of the loading sequence. Therefore, the pile accumulated displacement due to a first load package A with N_A cycles can be represented by $N_{B.eq.A}$ cycles of a subsequent load package B. Thus, the pile displacement after the load packages A and B, with N_A and N_B cycles respectively, can be calculated as the one resulting from the load package B with $N_{A,B} = N_{B.eq.A} + N_B$ cycles. This is illustrated in Fig. 50.

Accordingly, the following procedure was followed for the application of the proposed model. Initially, the first load package A with N_A cycles is evaluated and the corresponding pile displacement $y_{A(N_A)}$ at ground level is obtained. Then, an equivalent number of load cycles $N_{B.eq.A}$ with the amplitude of the second load package B resulting in the same pile displacements $y_{A(N_A)}$ needs to be determined. Therefore, the relationship $y_{A(N_A)} = y_{B(N_{B.eq.A})}$ must be fulfilled. Finally, the cumulative pile displacements $y|_{A(N_A)+B(N_B)}$ caused by both load packages is computed as the pile displacements caused by a single load package with amplitude B and a number of load cycles equal to $N_{B.eq.A} + N_B$.

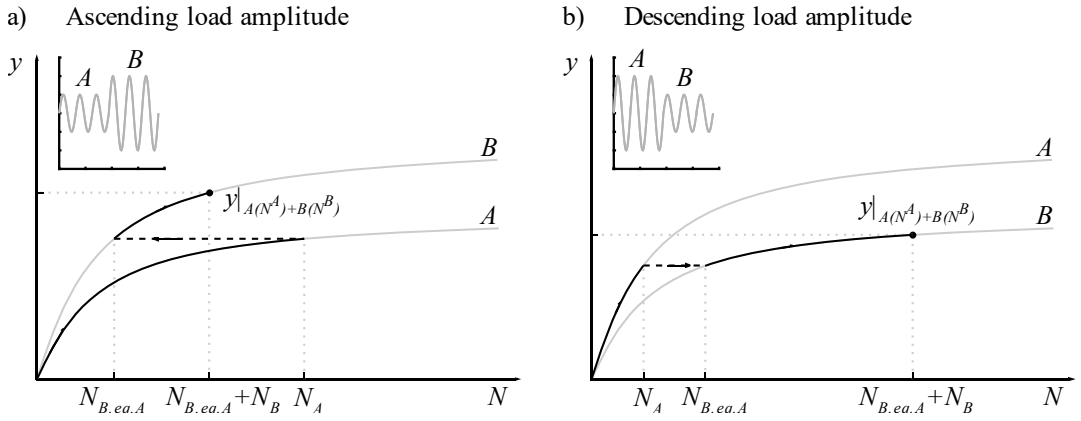

Fig. 50 Sketch of the superposition method following the Miner's rule for pile displacements after multi-amplitude cyclic loading.

Simulations were performed with the proposed model employing the Miner's rule based superposition method and setting parameters $\{\varphi_c, e_{d0}, e_{c0}, e_{i0}, \beta, n_B\} = \{33.1°, 0.677, 1.054, 1.212, 2.5, 0.27\}$ and $D_r = 60\%$ reported by (Staubach & Wichtmann, 2020). The effective unit weight was assumed as $\gamma' = 9.6$ kN/m^3 in accordance with the reported distribution of horizontal effective stress in (Staubach & Wichtmann, 2020). The results are shown in Fig. 51.b. The predicted deflection curves are in agreement with the numerical results. The Miner's rule approach was satisfactorily applied with the proposed model to account for multi-amplitude cyclic horizontal loading.

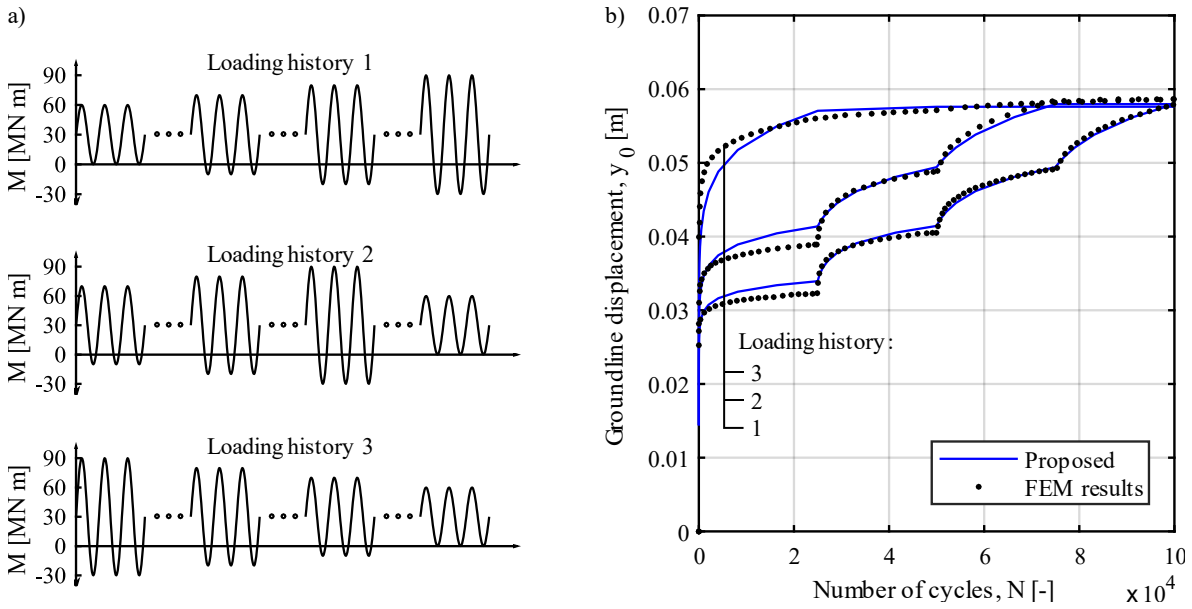

Fig. 51 Evaluation of multi-amplitude cyclic loading. Pile deflection at ground level against number of loading cycles N predicted by the proposed model and compared to FE simulations by (Staubach & Wichtmann, 2020). Pile length $L = 30$ m, pile diameter $D = 5$ m.

5.4. Evaluation of model performance with field and centrifuge tests

The performance of the proposed model is evaluated by comparison with the results from a centrifuge test performed by (Choo & Kim, 2016) and two field tests reported by (W. Li et al., 2017) and (W. Li et al., 2015).

5.4.1. Simulation of a Centrifuge test

Choo and Kim (Choo & Kim, 2016) performed a series of centrifuge tests to simulate large diameter steel monopiles embedded in dense sands. The tests were conducted at the centrifuge facility from the Korea Advanced Institute of Science and Technology (KAIST), which operates a geotechnical beam centrifuge with a platform radius of 5 m, a maximum capacity of $240g$-tons and a maximum centrifugal acceleration of $130g$ (D.-S. Kim et al., 2013). The platform dimensions of the centrifuge are 1.2 m × 1.2 m × 1.2 m. Fig. 52 presents the geotechnical centrifuge at KAIST as reported by (D.-S. Kim et al., 2013).

According to (Choo & Kim, 2016), four different tests (M1 to M4) were performed with the aim to evaluate the effect of different pile flexural rigidities, length to diameter ratios and a rock bearing layer at the tip of a monopile (see Fig. 53). The tests were conducted at centrifugal accelerations of $60g$ and $75g$, and were set up in a cylindrical container made of steel. The internal dimensions of the container in model scale were 0.9 m in diameter and 0.7 m in height.

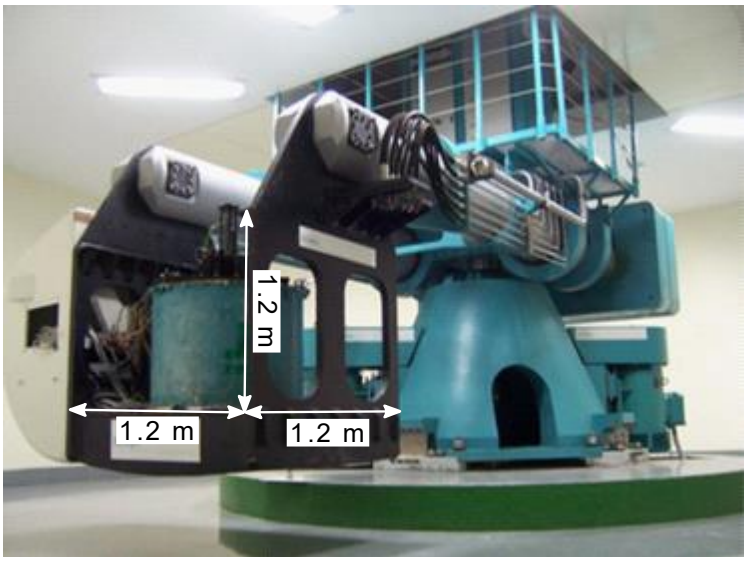

Fig. 52 Geotechnical centrifuge at the Korea Advanced Institute of Science and Technology (KAIST). Taken from (D.-S. Kim et al., 2013).

In all cases, model piles were subjected to a horizontal loading applied at a distance h above the ground surface. The loading was applied using a linear actuator (see Fig. 54). The pile deflection curves were measured by specialized instrumentation and reported at different stages of the horizontal load. The specialized instrumentation included strain gauges along the piles that allowed to measure the distribution of moments at different depths and stages of loading. The distributions of lateral displacements (deflection curves) were calculated from the bending moment distributions. For the present analysis, test M1 was selected to be simulated with the proposed model.

Test M1 was performed at a centrifugal acceleration of $75g$ and considered a model pile made of copper with a unit weight of $\gamma_{co} = 87.6$ kN/m^3 and a Young modulus of $E_{co} = 117$ GPa. A single layer of dense sand was constructed for this test (see Fig. 53). The diameter, wall thickness and embedment length of the model pile were $D_{m,co} = 79.4$ mm, $t_{m,co} = 1.2$ mm and $L_{m,co} = 413.3$ mm respectively. Considering a scale ratio of 1:75, the latter correspond to a prototype pile made of copper with $D_{p,co} = 6.0$ m, $t_{p,co} = 0.09$ m and $L_{p,co} = 31$ m. The moment of inertia for the prototype pile made of copper is obtained as:

$$I_{p,co} = \frac{\pi}{4}\left[\left(\frac{D_{p,co}}{2}\right)^4 - \left(\frac{D_{p,co} - 2\,t_{p,co}}{2}\right)^4\right] \tag{74}$$

which gives $I_{p,co} = 7.13$ m^4. Thus, the flexural rigidity for the prototype pile made of copper is obtained as $E_{co}\,I_{p,co} = 8.34 \times 10^8$ kN·m^2. If the prototype pile is considered as made of steel with a diameter of $D_{p,st} = 6.0$ m, its equivalent thickness $t_{p,st}$ can be obtained using the relationship:

$$E_{co}\, I_{p,co} = E_{st}\, I_{p,st} = E_{st}\, \frac{\pi}{4}\left[\left(\frac{D_{p,st}}{2}\right)^4 - \left(\frac{D_{p,st} - 2\, t_{p,st}}{2}\right)^4\right] \tag{75}$$

where E_{st} is the Young modulus of the steel and $I_{p,st}$ is the moment of inertia for the prototype pile made of steel. Considering $E_{st} = 199$ GPa, an equivalent thickness of $t_{p,st} = 0.052$ m for the prototype pile made of steel is obtained. To apply the proposed model, the geometric and material properties of the prototype pile made of copper were considered.

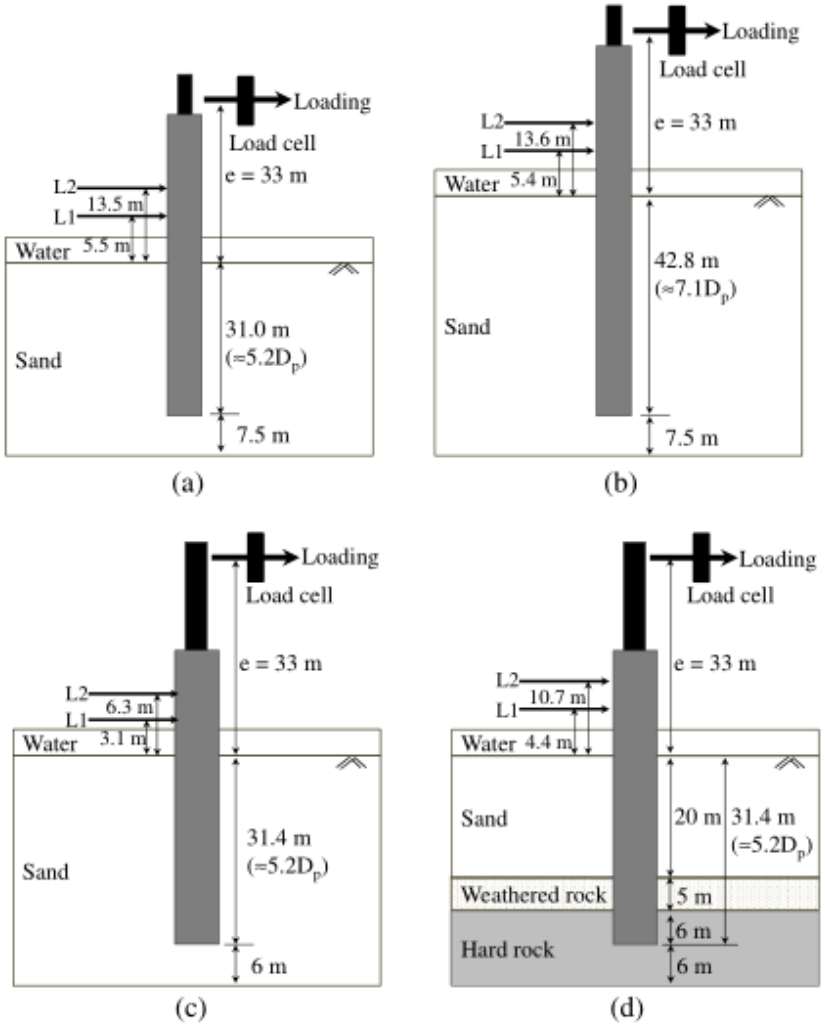

Fig. 53 Arrangement of centrifuge tests conducted at the Korea Advanced Institute of Science and Technology (KAIST): Tests (a) M1; (b) M2; (c) M3; (d) M4. Units are in prototype scale. Taken from (Choo & Kim, 2016).

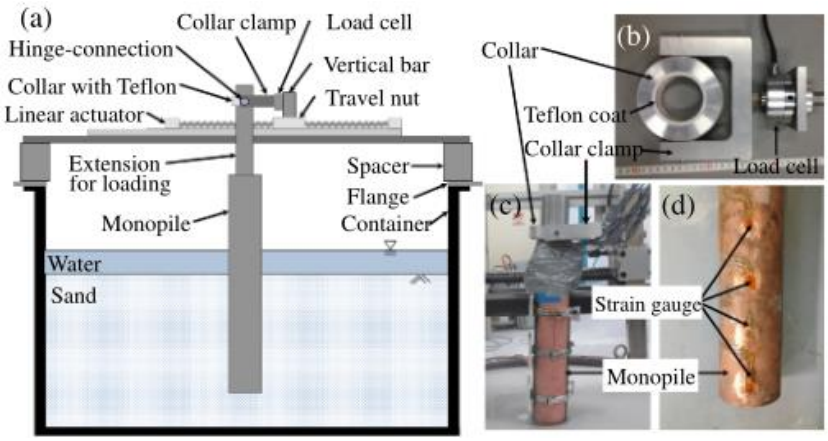

Fig. 54 Assembly of centrifuge tests conducted at the Korea Advanced Institute of Science and Technology (KAIST). Taken from (Choo & Kim, 2016).

The pile was embedded in a dense silica sand with $D_r = 86\%$. The sand was artificially created from quartzite which was crushed with a hammer crusher. Initially, the sand was pluviated with a sand-raining device into the centrifuge container to form a bearing base layer, in which the base of the monopile was jacked. Then, the sand was pluviated around the pile until the desired embedded pile length was reached. Finally, the model was submerged in water. Considering the preparation method adopted for the sand layers, pile installation effects are not expected to play a significant role on the pile response. This is because the sample preparation is the one of a non-displacement pile. Some index properties of the sand, as the specific gravity, maximum and minimum dry densities, main grain size and coefficient of uniformity were reported as $G_s = 2.63$, $\gamma_{d,\max} = 16.09$ kN/m^3, $\gamma_{d,\min} = 12.16$ kN/m^3, $D_{50} = 0.237$ mm and $c_u = 1.60$ respectively. The effective unit weight of the soil was evaluated at $z = L/2$ and gave $\gamma' = 9.9$ kN/m^3.

To apply the proposed model, the set of parameters $\{\varphi_c, e_{d0}, e_{c0}, e_{i0}, D_r, \beta, n_B\}$ for the silica sand was defined as follows: The critical state friction angle was set to $\varphi_c = 36.6°$. This value was obtained from triaxial compression tests on samples of a very similar silica sand, which was prepared following the same procedure and in the same laboratory facilities as by the centrifuge soil model in study (J. H. Kim et al., 2016). The minimum and critical void ratios were computed with $e_{d0} = \gamma_s/\gamma_{d,\max} - 1 = 0.604$ and $e_{c0} = \gamma_s/\gamma_{d,\min} - 1 = 1.122$, considering the unit weight of solids as $\gamma_s = G_s\,\gamma_w = 25.8$ kN/m^3 and the values of $\gamma_{d,\max}$ and $\gamma_{d,\min}$ as given above. The loosest void ratio e_{i0} can be approximated as $e_{i0} \approx 1.2e_{c0} = 1.346$. The relative density was taken as $D_r = 86\%$. To obtain parameter β, the following equation was found by equaling Equations (38) and (51) and assuming that $\sigma' = \sigma'_{z'}$:

$$\beta = \frac{\ln\left[\frac{K_p^2}{K_{p0}^2}\frac{1+e_{i0}}{1+e_0}\right]}{\ln\left[\frac{e_{i0}}{e_0}\right]} \tag{76}$$

where $K_p = \tan^2(45 + \varphi/2)$, $K_{p0} = \tan^2(45 + \varphi_c/2)$ and $e_0 = e_{c0} - D_r(e_{c0} - e_{d0})$. A value of $\beta = 1.69$ was computed from the last equation using values of $\varphi = 45.2°$ and $D_r = 83\%$, which were reported by a drained triaxial compression test performed on an specimen of the silica sand under an initial confining pressure of $\bar{\sigma}' = 100$ kPa (Choo & Kim, 2016). The latter test was chosen considering that the mean effective pressure at the middle of the embedded pile depth was computed as $\bar{\sigma}' = 92.3$ kPa. Finally, a typical value of $n_B = 0.30$ was adopted as by some fine sands.

In prototype scale, a horizontal load was gradually applied to the pile at a distance of $h = 33$ m above the ground surface. The deflection curves predicted by the proposed model are compared to the experimental results in Fig. 55. The evolution of the deflection curves was simulated in a satisfactory manner by the proposed model, specially for the cases with $H = \{2.5; 5.0; 10\}$ MN. For the case with $H = 15$ MN, a discrepancy of about 0.02 m was obtained. Note that, the rotation point at z ≈ 20 m was also captured by the proposed model.

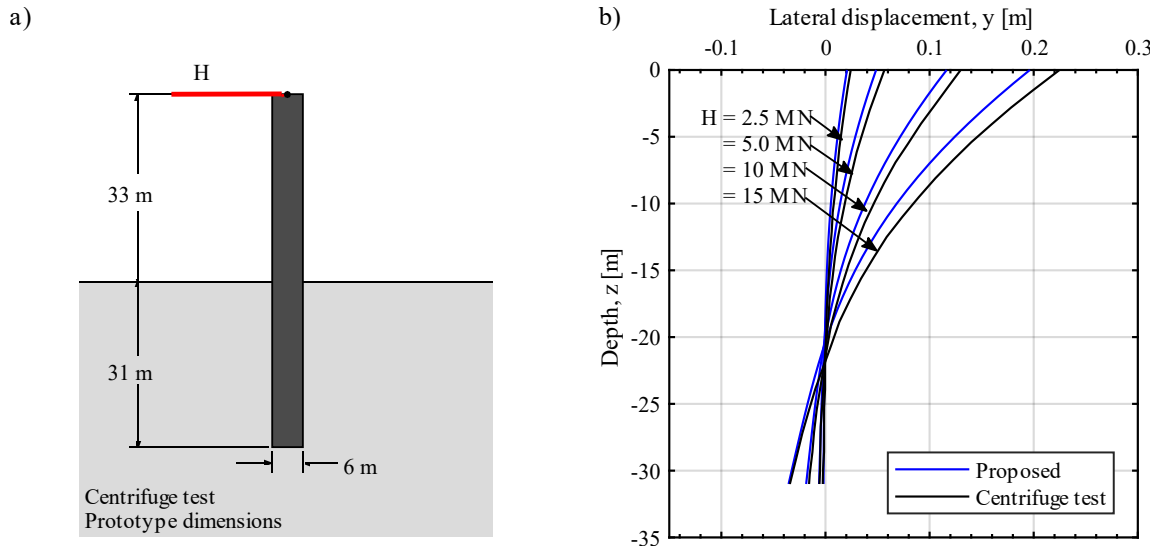

Fig. 55 Evaluation of the performance of the proposed model against centrifuge tests results by (Choo & Kim, 2016).

5.4.2. Simulation of Field tests

Li et al. (W. Li et al., 2017) and Li et al. (W. Li et al., 2015) conducted a series of field tests on reduced-scale steel monopiles in a dense siliceous sand. The tests were conducted at the pile testing research site from the University College Dublin (UCD) at Blessington, Co. Wicklow. The testing program incorporated monotonic and cyclic horizontal loading. For this analysis, the static lateral loading test denoted as PS2 in (W. Li et al., 2017) and the cyclic lateral loading test denoted as PC2 in (W. Li et al., 2015) were simulated with the proposed model. Fig. 56 and Fig. 57 present the set-up for the field tests PS2 and PC2 respectively, as reported by the mentioned studies. The tested piles had a diameter of $D =$

0.34 m, a total length of $L_{tot} = 3$ m, an embedment length of $L = 2.2$ m and a pile wall thickness of $t_p = 14$ mm. The Young modulus for the pile material was assumed as E = 210 GPa. Although the dimensions are very small in comparison with real scale monopiles, similar length to diameter ratios were used to simulate the rigid behavior of large diameter monopiles.

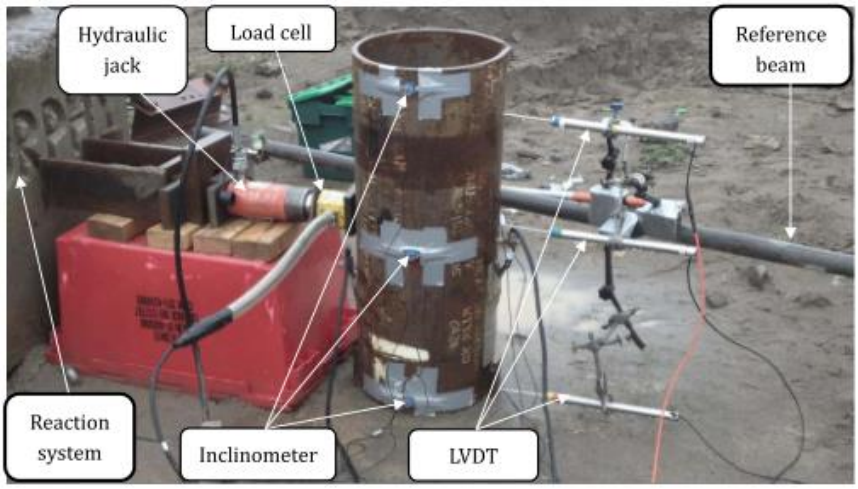

Fig. 56 Assembly of static field test PS2. Taken from (W. Li et al., 2017).

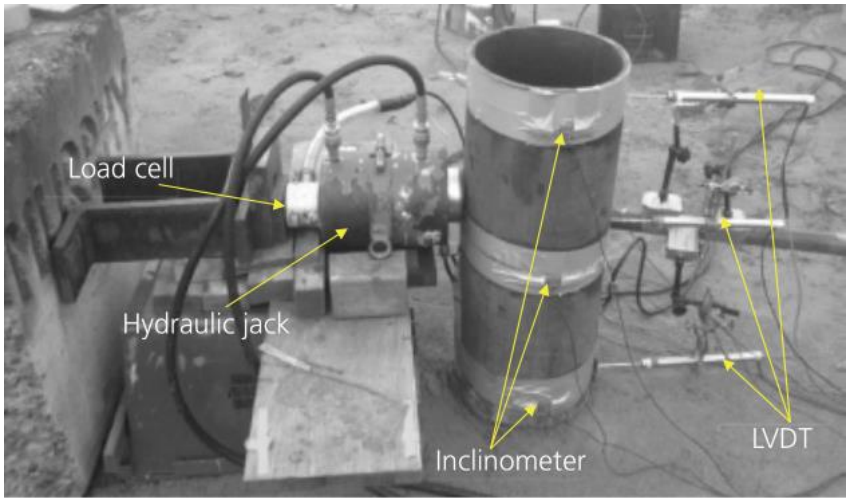

Fig. 57 Assembly of cyclic field test PC2. Taken from (W. Li et al., 2015).

The test site at Blessington, Co. Wicklow has been extensively investigated with field and laboratory testing studies, as reported in (K. Gavin et al., 2014; K. G. Gavin & O'Kelly, 2007; Igoe et al., 2011; Tolooiyan & Gavin, 2011). The soil at the site corresponds to an uniform over-consolidated dense sand. The depth of the groundwater table is about 15 m below the groundline and the unit weight of the soil has been estimated as $\gamma = 20$ kN/m^3. As concluded by (W. Li et al., 2017), considering the location of the groundwater table, the effects of the pore water pressure is expected to be negligible. The average main grain size and the

coefficient of uniformity were specified in (Le, 2015) as $D_{50} = 0.13$ mm and $c_u = 2.50$ respectively. The sand has been explored through a series of Cone Penetration Tests (CPT). The authors (W. Li et al., 2015, 2017) reported the maximum, averaged and minimum values of the cone tip resistance q_c. Fig. 58.a shows the reported maximum and minimum limits. As determined in (W. Li et al., 2017), the measured profile of q_c can be fitted to the power function q_c [MPa] $= 10.9\left(z/z_{ref}\right)^{0.35}$ where $z_{ref} = 1$ m. This is also shown in Fig. 58.a.

To apply the proposed model, the set of parameters $\{\varphi_c, e_{d0}, e_{c0}, e_{i0}, D_r, \beta, n_B\}$ was defined as follows. The critical state friction was set as $\varphi_c = 37°$, as reported in (W. Li et al., 2017). The minimum and critical state void ratios were computed from the correlations proposed by Duque et al. (Duque et al., 2020) with the mean particle size (D_{50}) as $e_{d0} = 0.4291\, D_{50}^{-0.189} = 0.631$ and $e_{c0} = 0.6729\, D_{50}^{-0.166} = 0.944$. Note that similar values of $e_{d0} = 0.57$ and $e_{c0} = 0.91$ were experimentally obtained in (Doherty et al., 2020) for a Blessington silica sand in other location. The loosest void ratio e_{i0} was approximated as $e_{i0} \approx 1.2e_{c0} = 1.133$. The relative density profile D_r was obtained from the CPT results following the correlation $D_r = 0.268 \ln(q_{t1}) - b_x$ with $q_{t1} = (q_c/p_a)/(\sigma'/p_a)^{0.5}$ by Jamiolkowski et al. (Jamiolkowski et al., 2003), with $b_x = 0.675$ (see Fig. 58.c). Parameter β was defined following equation (76). To do so, the peak friction angle φ was computed based on the CPT results. The correlation $\tan\varphi = 1/2.68\,(\log(q_c/\sigma') + 0.29)$ by Robertson and Campanella (Robertson & Campanella, 1983) was used for that purpose (see Fig. 58.c). The β profile was then computed using the values of the φ profile and D_r profile. Parameter n_B was calibrated to provide the best response under monotonic loading. Hence, the resulting calibration value for n_B, also accounts for installation effects. It was found that a value of $n_B = 0.3$ provided an accurate simulation of the pile response with the proposed model.

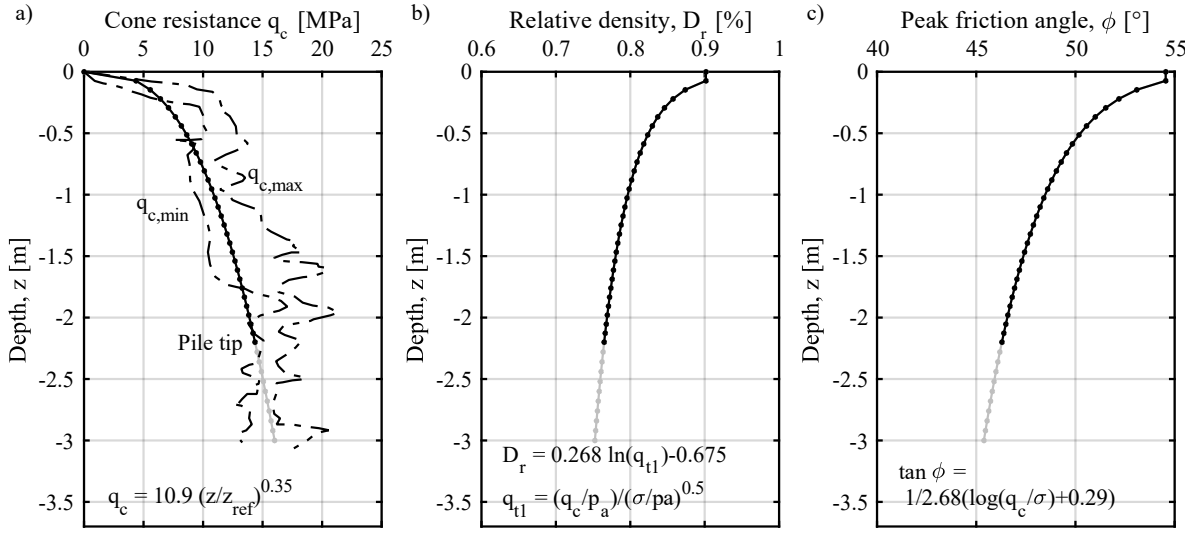

Fig. 58 Site exploration reported by (W. Li et al., 2015, 2017). a) CPT (q_c). b) D_r computed from CPT results. c) φ computed from CPT results.

In the static lateral loading test PS2, a horizontal force was applied to the monopile at increments of 10 kN until reaching a value of $H = 110$ kN. A hydraulic jack was used for this purpose. The load eccentricity was $h = 0.4$ m. The test was instrumented with Linear Variable Differential Transformers (LVDTs) above the ground surface to obtain the pile lateral displacements. The measured load-displacement curve at ground level is shown in Fig. 59.a along with the predicted curve by the proposed model. Despite that a good agreement is in general observed, some discrepancies are shown for loads greater than 50 kN. In the cyclic lateral loading test PC2, the monopile was subjected to multi-amplitude lateral cyclic loading. The load was applied at a distance above the ground level of $h = 0.4$ m using a hydraulic jack and the pile head displacements were measured using a series of LVDTs. One-way cyclic loading was considered, which means that the minimum and maximum values of applied force were zero and $H = H_{\max} = 2\,H_{\text{amp}}$. Three sequential loading series with $H_{\max} = \{33; 44; 77\}$ kN were applied to the test pile. The number of loading cycles for each loading series was $N = \{1054; 1305; 814\}$ respectively, which results in a total number of loading cycles of $N = 3173$. As previously done in Section 5.3.4, the Miner's rule based superposition method was employed with the proposed model to obtain the accumulated pile displacement due to cyclic loading. The results are compared to the experimental measurements in Fig. 59.b, which shows the increase of pile displacements at ground level due to cyclic loading Δy_N. The later was computed as $\Delta y_N = y_{acc} - y_{sta}$, where y_{acc} is the accumulated displacement at ground level due to N loading cycles and y_{sta} is the pile displacement at $z = 0$ m for $N = 1$ where $H = H_{ave} = H_{amp}$ (see Fig. 38). For the field test, y_{acc} was computed from the accumulated displacement produced by the maximum force at each cycle. In general, a congruent prediction is obtained, although a small underestimation of Δy_N for the first two load packages is noted.

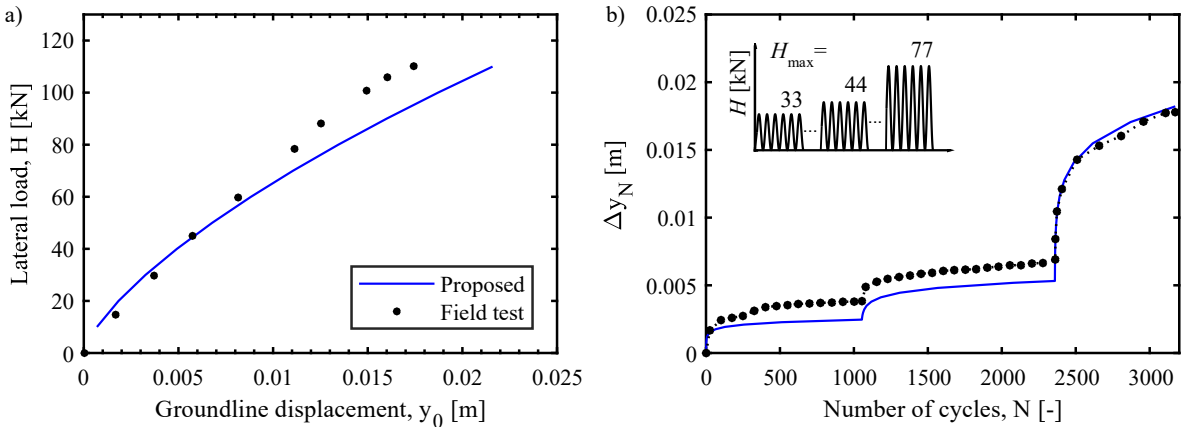

Fig. 59 Evaluation of the performance of the proposed model against field tests results by (W. Li et al., 2017) and (W. Li et al., 2015).

Chapter 6: Conclusions and Outlook

6.1. Summary of conclusions

This research project analyzed the behavior of laterally loaded monopiles in sands using three-dimensional finite element modelling and one-dimensional finite difference modelling techniques. First, a comprehensive parametric study was conducted in which the pile response under monotonic lateral loading was evaluated through 3D FE simulations considering different pile geometries, soil materials and loading cases. The analysis was oriented for laterally loaded monopiles embedded in sands with diameters between $D = \{5 - 7\}$ m and embedment lengths between $L = \{20 - 30\}$ m and for soil's relative densities between $D_r = \{40\% - 80\%\}$. Advanced constitutive models for the soil were implemented, namely the hypoplastic model for sands by von Wolfersdorff (von Wolffersdorff, 1996) extended with the intergranular strain concept by Niemunis and Herle (Niemunis & Herle, 1997), which allowed for accurate estimations of the soil behavior.

Based on the FE simulation results, it was concluded that a simplification of the pile behavior as purely rigid or flexible is not suitable for large diameter monopiles. This is because all monopiles within the studied range of pile geometries presented rotational as well as flexural motion. The FE simulations also showed that non-negligible displacements at the pile base were generated even at low loading conditions. This led to further analysis of the base shear reaction which was extracted from the FE simulations and carefully examined. It was found that this reaction has a non-linear relationship with the base pile displacements and depends not only on the pile geometry but also on the soil's relative density. Different aspects of the pile response were also studied using the FE simulations results such as the resulting deflection curves, load-displacements curves, depth of the pile rotation point and evolution of the horizontal stresses in the regions near the pile.

Subsequently, a 1D model based on the Beam on a Non-Linear Winkler Foundation approach was proposed as a simplified practical tool to improve the modelling and design of monopiles

under monotonic and long-term cyclic lateral loading conditions. The proposed model considered new relationships for the ultimate soil resistance p_u and soil reaction p, and introduced an equation for the base shear reaction S_B. These relationships were calibrated using the results from the conducted FE simulations. The equation for p_u allowed for a direct dependency on the soil's relative density and presents a non-linear distribution with depth. The equation for S_B allowed for an acceptable prediction of the measurements from the FE simulations. In addition, a cyclic factor f_A was proposed to simulate the response of monopiles under long-term cyclic lateral loading conditions. The proposed factor considers the effect of the soil's relative density and some loading characteristics such as number of loading cycles and the amplitude and average values of the applied cyclic loading. FE simulations results of monopiles under cyclic loading reported in the literature were used to calibrate the equation for f_A. The proposed model showed a good performance when compared to results from FE simulations as well as to results from field and centrifuge tests. However, further development of the proposed model may be achieved by considering a wider range of pile geometries and soil conditions.

6.2. Outlook

This section presents some suggestions for further research related to the topics of this work. First, regarding the numerical modelling of monopiles, there is still a potential for improvement of the modelling techniques. When modelling displacement piles, such as offshore wind turbine monopiles, the effects of pile installation may play a significant role on the initial stress and density fields around the monopile. This work adopted a simplified "wished-in-place" approach which does not simulate the effects caused by the pile installation. Therefore, the incorporation of such effects in the FE simulations and the corresponding recalibration of the proposed p-y model are topics that could constitute the basis for a new stage of this work. This, however, is a challenging task given the complex nature of the pipe pile installation process. During the latter, the soil undergoes large deformations which can not be numerically simulated using common approaches based on the Lagrangian formulation, such as the one adopted for this work. Instead, alternative sophisticated numerical approaches that allow the simulation of large soil deformations may be adopted.

Moreover, a worthy extension of this work would be to incorporate additional experimental data from large scale field testing or laboratory studies that allow to evaluate and compare the performance of different modelling techniques, and hence, to upgrade the state-of-the-art knowledge about the numerical modelling of these problems. Specifically, given the complex behavior of the soil under long-term cyclic loading, additional experimental studies on this topic considering a larger number of cycles $N > 10^6$ are required. Also, a sensitivity analysis on the size of the soil elements near the pile base and the effects on the extracted FE simulation results may be also valuable to further understand the stress-strain behavior near

the base of the pile and to validate the obtained results in this work. In addition, this work may be extended by evaluating different types of soil or pile geometries outside of the studied range. Precisely, the analysis of monopiles with larger diameters and embedded in layered soils may be considered as valuable topics of research by the industry. In case of evaluating cohesive soils, the simulation of consolidation effects may be a particular topic for further research. The adopted modelling technique in this work can not simulate such effects, and therefore a different technique should be adopted to simulate important aspects such as the accumulation of excess pore pressure during load application and its dissipation over time.

Regarding the development of the simplified design tool for large diameter monopiles, a new stage to continue this work may be based on two essential aspects. The first aspect is to incorporate additional and improved finite element simulation results that serve as a basis for recalibration and evaluation of the p-y model. The proposed model was calibrated for a certain range of pile geometries and granular soils. Its verification and the extension of its range of applicability may be a subject for further research. The second aspect is to adopt more advanced calibration methods for the p-y model, such as Bayesian analysis, that allows to make statistical inferences concerning the different parameters of the model.

Bibliography

Abadie, C. N., Byrne, B. W., & Levy-Paing, S. (2015). *Model pile response to multi-amplitude cyclic lateral loading in cohesionless soils*. *1*, 681–686. https://doi.org/10.17863/CAM.40861

ABAQUS, Inc. (2006). *ABAQUS Online Documentation: ABAQUS/Standard User's Manual, Version 6.6*. Dassault Systèmes Simulia Corp.

Achmus, M., Abdel-Rahman, K., & Kuo, Y. S. (2007). Numerical modelling of large diameter steel piles under monotonic and cyclic horizontal loading. *Proceedings of the 10th International Symposium on Numerical Models in Geomechanics NUMOG 10*, 453–459.

Achmus, M., Kuo, Y. S., & Abdel-Rahman, K. (2009). Behavior of monopile foundations under cyclic lateral load. *Computers and Geotechnics*, *36*(5), 725–735. https://doi.org/10.1016/j.compgeo.2008.12.003

Achmus, Martin, Thieken, K., Saathoff, J.-E., Terceros, M., & Albiker, J. (2019). Un- and reloading stiffness of monopile foundations in sand. *Applied Ocean Research*, *84*, 62–73. https://doi.org/10.1016/j.apor.2019.01.001

Adams, J. I., & Radhakrishna, H. S. (1973). The Lateral Capacity of Deep Augured Footings. *Proceedings of the 8th International Conference on Soil Mechanics and Foundation Engineering*.

Ahmed, S. S., & Hawlader, B. (2016). Numerical Analysis of Large-Diameter Monopiles in Dense Sand Supporting Offshore Wind Turbines. *International Journal of Geomechanics*, *16*(5), 04016018. https://doi.org/10.1061/(ASCE)GM.1943-5622.0000633

API. (2014a). *API RP 2A-WSD: Planning, Designing and Constructing Fixed Offshore Platforms—Working Stress Design* (22nd ed.). American Petroleum Institute.

API. (2014b). *API RP 2GEO: Geotechnical and Foundation Design Considerations* (1st ed.). American Petroleum Institute.

Arany, L., Bhattacharya, S., Macdonald, J., & Hogan, S. J. (2017). Design of monopiles for offshore wind turbines in 10 steps. *Soil Dynamics and Earthquake Engineering*, *92*, 126–152. https://doi.org/10.1016/j.soildyn.2016.09.024

Arshad, M., & O'Kelly, B. C. (2016). Analysis and Design of Monopile Foundations for Offshore Wind-Turbine Structures. *Marine Georesources & Geotechnology*, *34*(6), 503–525. https://doi.org/10.1080/1064119X.2015.1033070

Barton, Y. O. (1982). *Laterally loaded model piles in sand: Centrifuge tests and finite element analyses* [PhD Thesis]. University of Cambridge.

Bauer, E. (1992). *Zum mechanischen Verhalten granularer Stoffe unter vorwiegend ödometrischer Beanspruchung* [PhD Thesis]. Veröffentlichungen des Institutes für Bodenmechanik und Felsmechanik der Universität Fridericiana in Karlsruhe. 130. Graz, Tech. Univ., Diss. v. 24.7.1992.

Bauer, E. (1996). Calibration of a Comprehensive Hypoplastic Model for Granular Materials. *Soils and Foundations*, *36*(1), 13–26. https://doi.org/10.3208/sandf.36.13

Bienen, B., Dührkop, J., Grabe, J., Randolph, M. F., & White, D. J. (2012). Response of Piles with Wings to Monotonic and Cyclic Lateral Loading in Sand. *Journal of Geotechnical and Geoenvironmental Engineering*, *138*(3), 364–375. https://doi.org/10.1061/(ASCE)GT.1943-5606.0000592

Bouzid, D. A. (2018). Numerical Investigation of Large-Diameter Monopiles in Sands: Critical Review and Evaluation of Both API and Newly Proposed p-y Curves. *International Journal of Geomechanics*, *18*(11), 04018141. https://doi.org/10.1061/(ASCE)GM.1943-5622.0001204

Brødbæk, K. T., Møller, M., Sørensen, S. P. H., & Augustesen, A. H. (2009). *Review of p-y relationships in cohesionless soil* (DCE Technical Reports No. 57). Department of Civil Engineering, Aalborg University.

Broms, B. B. (1964). Lateral Resistance of Piles in Cohesionless Soils. *Journal of the Soil Mechanics and Foundations Division*, *90*(3), 123–156.

Burd, H. J., Taborda, D. M. G., Zdravković, L., Abadie, C. N., Byrne, B. W., Houlsby, G. T., Gavin, K. G., Igoe, D. J. P., Jardine, R. J., Martin, C. M., McAdam, R. A., Pedro, A. M. G., & Potts, D. M. (2019). PISA design model for monopiles for offshore wind turbines: Application to a marine sand. *Géotechnique*, 1–19. https://doi.org/10.1680/jgeot.18.P.277

Byrne, B. W., McAdam, R. A., Burd, H. J., Houlsby, G. T., Martin, C. M., Beuckelaers, W. J. A. P., Zdravković, L., Taborda, D. M. G., Potts, D. M., Jardine, R. J., Ushev, E., Liu, T., Abadias Gomez, D., Gavin, K., Igoe, D., Doherty, P., Skov Gretlund, J.,

Pacheco Andrade, M., Muir Wood, A., … Plummer, M. A. L. (2017). PISA: New design methods for offshore wind turbine monopiles. *Proceedings of the Society for Underwater Technology Offshore Site Investigation and Geotechnics 8th International Conference on "Smarter Solutions for Future Offshore Developments"*, 142–161.

Carvajal-Romo, G., Valderrama-Mendoza, M., Rodríguez-Urrego, D., & Rodríguez-Urrego, L. (2019). Assessment of solar and wind energy potential in La Guajira, Colombia: Current status, and future prospects. *Sustainable Energy Technologies and Assessments*, *36*, 100531. https://doi.org/10.1016/j.seta.2019.100531

Chari, T. R., & Meyerhof, G. G. (1983). Ultimate capacity of rigid single piles under inclined loads in sand. *Canadian Geotechnical Journal*, *20*(4), 849–854. https://doi.org/10.1139/t83-091

Choo, Y. W., & Kim, D. (2016). Experimental Development of the p-y Relationship for Large-Diameter Offshore Monopiles in Sands: Centrifuge Tests. *Journal of Geotechnical and Geoenvironmental Engineering*, *142*(1), 04015058. https://doi.org/10.1061/(ASCE)GT.1943-5606.0001373

Collins, I. F., & Houlsby, G. T. (1997). Application of thermomechanical principles to the modelling of geotechnical materials. *Proceedings of the Royal Society of London. Series A: Mathematical, Physical and Engineering Sciences*, *453*(1964), 1975–2001. https://doi.org/10.1098/rspa.1997.0107

Cox, W. R., Reese, L. C., & Grubbs, B. R. (1974, January 1). *Field Testing of Laterally Loaded Piles In Sand*. Offshore Technology Conference. https://doi.org/10.4043/2079-MS

Dafalias, Y. F. (1986). Bounding Surface Plasticity. I: Mathematical Foundation and Hypoplasticity. *Journal of Engineering Mechanics*, *112*(9), 966–987. https://doi.org/10.1061/(ASCE)0733-9399(1986)112:9(966)

Dafalias, Y. F., & Herrmann, L. R. (1986). Bounding Surface Plasticity. II: Application to Isotropic Cohesive Soils. *Journal of Engineering Mechanics*, *112*(12), 1263–1291. https://doi.org/10.1061/(ASCE)0733-9399(1986)112:12(1263)

Damgaard, M., Bayat, M., Andersen, L. V., & Ibsen, L. B. (2014). Assessment of the Dynamic Behaviour of Saturated Soil Subjected to Cyclic Loading from Offshore Monopile Wind Turbine Foundations. *Computers and Geotechnics*, *61*, 116–126. https://doi.org/10.1016/j.compgeo.2014.05.008

Depina, I., Hue Le, T. M., Eiksund, G., & Benz, T. (2015). Behavior of cyclically loaded monopile foundations for offshore wind turbines in heterogeneous sands. *Computers and Geotechnics*, *65*, 266–277. https://doi.org/10.1016/j.compgeo.2014.12.015

DNV-GL-AS. (2016). *DNVGL-ST-0126: Support structures for wind turbines*. Det Norske Veritas group.

Doherty, P., Spagnoli, G., & Doherty, M. (2020). Laboratory investigations to assess the feasibility of employing a novel mixed-in-place offshore pile in calcareous deposits. *Ships and Offshore Structures*, *15*(1), 29–38. https://doi.org/10.1080/17445302.2015.1056579

Dührkop, J. (2009). *Zum Einfluss von Aufweitungen und zyklischen Lasten auf das Verformungsverhalten lateral beanspruchter Pfähle in Sand* [PhD Thesis]. Institut für Geotechnik und Baubetrieb, Technische Universität Hamburg-Harburg.

Duque, J., Fuentes, W., & Barros, J. (2020). Effect of grain size distribution on maximum and minimum void ratios of granular soils. *Accepted for Publication in Acta Geotechnica Slovenica*.

Dyson, G. J., & Randolph, M. F. (2001). Monotonic Lateral Loading of Piles in Calcareous Sand. *Journal of Geotechnical and Geoenvironmental Engineering*, *127*(4), 346–352. https://doi.org/10.1061/(ASCE)1090-0241(2001)127:4(346)

Ellison, K. c., Soga, K., & Simpson, B. (2012). A strain space soil model with evolving stiffness anisotropy. *Géotechnique*, *62*(7), 627–641. https://doi.org/10.1680/geot.10.P.095

Fleming, K., Weltman, A., Randolph, Mark., & Elson, K. (2009). *Piling Engineering*. Taylor and Francis.

Fuentes, W., Triantafyllidis, T., & Lascarro, C. (2017). Evaluating the Performance of an ISA-Hypoplasticity Constitutive Model on Problems with Repetitive Loading. In T. Triantafyllidis (Ed.), *Holistic Simulation of Geotechnical Installation Processes: Theoretical Results and Applications* (Vol. 82, pp. 341–362). Springer International Publishing.

Gavin, K., Doherty, P., & Tolooiyan, A. (2014). Field investigation of the axial resistance of helical piles in dense sand. *Canadian Geotechnical Journal*. https://doi.org/10.1139/cgj-2012-0463

Gavin, K. G., & O'Kelly, B. C. (2007). Effect of Friction Fatigue on Pile Capacity in Dense Sand. *Journal of Geotechnical and Geoenvironmental Engineering*, *133*(1), 63–71. https://doi.org/10.1061/(ASCE)1090-0241(2007)133:1(63)

Gupta, B. K., & Basu, D. (2016). Response of laterally loaded rigid monopiles and poles in multi-layered elastic soil. *Canadian Geotechnical Journal*, *53*(8), 1281–1292. https://doi.org/10.1139/cgj-2015-0520

GWEC. (2020). *Global Wind Report 2019*. Global Wind Energy Council.

Hansen, J. B. (1961). The ultimate resistance of rigid piles against transversal forces. *Bulletin 12, Danish Geotechnical Institute*, 5–9.

Hansen, M., Wolf, T. K., Rasmussen, K. L., Roesen, H. R., & Ibsen, L. B. (2013). *Physical Modelling of Cyclic Laterally Loaded Pile in Cohesionless Soil* (DCE Technical Memorandum No. 026). Department of Civil Engineering, Aalborg University.

Hashiguchi, K. (1989). Subloading surface model in unconventional plasticity. *International Journal of Solids and Structures*, *25*(8), 917–945. https://doi.org/10.1016/0020-7683(89)90038-3

Hashiguchi, K., & Chen, Z.-P. (1998). Elastoplastic constitutive equation of soils with the subloading surface and the rotational hardening. *International Journal for Numerical and Analytical Methods in Geomechanics*, *22*(3), 197–227. https://doi.org/10.1002/(SICI)1096-9853(199803)22:3<197::AID-NAG914>3.0.CO;2-T

Hearn, E. N., & Edgers, L. (2010). Finite Element Analysis of an Offshore Wind Turbine Monopile. In *GeoFlorida 2010* (pp. 1857–1865).

Herle, I., & Gudehus, G. (1999). Determination of parameters of a hypoplastic constitutive model from properties of grain assemblies. *Mechanics of Cohesive-Frictional Materials*, *4*(5), 461–486. https://doi.org/10.1002/(SICI)1099-1484(199909)4:5<461::AID-CFM71>3.0.CO;2-P

Hetenyi, M. (1946). *Beams On Elastic Foundation: Theory With Applications In The Fields Of Civil And Mechanical Engineering*. Ann Arbor, University of Michigan Press.

Houlsby, G. T., & Puzrin, A. M. (2000). A thermomechanical framework for constitutive models for rate-independent dissipative materials. *International Journal of Plasticity*, *16*(9), 1017–1047. https://doi.org/10.1016/S0749-6419(99)00073-X

IDEAM. (2015). *Atlas Interactivo de Viento en Colombia.* Velocidad del viento a 80 metros de altura (m/s). Anual. http://atlas.ideam.gov.co/visorAtlasVientos.html

IEA. (2019a). *Offshore Wind Outlook 2019* [World Energy Outlook Special Report]. International Energy Agency. www.iea.org

IEA. (2019b). *World Energy Outlook 2019*. International Energy Agency. www.iea.org

Igoe, D. J. P., Gavin, K. G., & O'Kelly, B. C. (2011). Shaft Capacity of Open-Ended Piles in Sand. *Journal of Geotechnical and Geoenvironmental Engineering*, *137*(10), 903–913. https://doi.org/10.1061/(ASCE)GT.1943-5606.0000511

IRENA. (2019). *Future of Wind: Deployment, investment, technology, grid integration and socio-economic aspects (Global Energy Transformation paper)*. International Renewable Energy Agency. www.irena.org

IRENA. (2020). *Global Renewables Outlook: Energy transformation 2050*. International Renewable Energy Agency. www.irena.org/publications

ISO. (2013). *ISO 19902:2007/Amd 1:2013: Petroleum and natural gas industries—Fixed steel offshore structures—Amendment 1*.

ISO. (2016). *ISO 19901-4:2016: Petroleum and natural gas industries—Specific requirements for offshore structures—Part 4: Geotechnical and foundation design considerations*.

Jamiolkowski, M., Lo Presti, D. C. F., & Manassero, M. (2003). Evaluation of Relative Density and Shear Strength of Sands from CPT and DMT. *Soil Behavior and Soft Ground Construction*, 201–238.

Jonkman, J., Butterfield, S., Musial, W., & Scott, G. (2009). *Definition of a 5-MW Reference Wind Turbine for Offshore System Development*. National Renewable Energy Laboratory (NREL).

Joo, J. S. (1985). *Behaviour of large scale rigid model piles under inclined loads in sand* [Master's Thesis]. Memorial University of Newfoundland.

Kallehave, D., Thilsted, C. L., & Liingaard, M. A. (2012). Modification of the API p-y Formulation of Initial Stiffness of Sand. *SUT-OSIG-12-50*.

Kallehave, Dan, Byrne, B. W., LeBlanc Thilsted, C., & Mikkelsen, K. K. (2015). Optimization of monopiles for offshore wind turbines. *Philosophical Transactions of the Royal Society A: Mathematical, Physical and Engineering Sciences*, *373*(2035), 20140100. https://doi.org/10.1098/rsta.2014.0100

Kézdi, Á. (1970). *Handbuch der Bodenmechanik: Bodenmechanik im Erd-, Grund- und Strassenbau*. VEB Verlag für Bauwesen.

Kim, D.-S., Kim, N.-R., Choo, Y. W., & Cho, G.-C. (2013). A newly developed state-of-the-art geotechnical centrifuge in Korea. *KSCE Journal of Civil Engineering*, *17*(1), 77–84. https://doi.org/10.1007/s12205-013-1350-5

Kim, J. H., Choo, Y. W., Kim, D. J., & Kim, D. S. (2016). Miniature Cone Tip Resistance on Sand in a Centrifuge. *Journal of Geotechnical and Geoenvironmental Engineering*, *142*(3), 04015090. https://doi.org/10.1061/(ASCE)GT.1943-5606.0001425

Klinkvort, R. T., & Hededal, O. (2013). Lateral response of monopile supporting an offshore wind turbine. *Proceedings of the Institution of Civil Engineers - Geotechnical Engineering*, *166*(2), 147–158. https://doi.org/10.1680/geng.12.00033

Le, V. H. (2015). *Zum Verhalten von Sand unter zyklischer Beanspruchung mit Polarisationswechsel im Einfachscherversuch* [PhD Thesis]. Technische Universität Berlin.

LeBlanc, C., Byrne, B. W., & Houlsby, G. T. (2010). Response of stiff piles to random two-way lateral loading. *Géotechnique*, *60*(9), 715–721. https://doi.org/10.1680/geot.09.T.011

LeBlanc, C., Houlsby, G. T., & Byrne, B. W. (2010). Response of stiff piles in sand to long-term cyclic lateral loading. *Géotechnique*, *60*(2), 79–90. https://doi.org/10.1680/geot.7.00196

Li, S., Zhang, Y., & Jostad, H. P. (2019). Drainage conditions around monopiles in sand. *Applied Ocean Research*, *86*, 111–116. https://doi.org/10.1016/j.apor.2019.01.024

Li, W., Igoe, D., & Gavin, K. (2015). Field tests to investigate the cyclic response of monopiles in sand. *Proceedings of the Institution of Civil Engineers - Geotechnical Engineering*, *168*(5), 407–421. https://doi.org/10.1680/jgeen.14.00104

Li, W., Zhu, B., & Yang, M. (2017). Static Response of Monopile to Lateral Load in Overconsolidated Dense Sand. *Journal of Geotechnical and Geoenvironmental Engineering*, *143*(7), 04017026. https://doi.org/10.1061/(ASCE)GT.1943-5606.0001698

Li, Z., Haigh, S. K., & Bolton, M. D. (2010). *Centrifuge modelling of mono-pile under cyclic lateral loads*. Proceedings of the 7th International Conference on Physical Modelling in Geotechnics (ICPMG 2010), Zurich, Switzerland. https://doi.org/10.1201/b10554

Lin, S.-S., & Liao, J.-C. (1999). Permanent Strains of Piles in Sand due to Cyclic Lateral Loads. *Journal of Geotechnical and Geoenvironmental Engineering*, *125*(9), 798–802. https://doi.org/10.1061/(ASCE)1090-0241(1999)125:9(798)

Little, R. L., & Briaud, J. L. (1988). *Full Scale Cyclic Lateral Load Tests on Six Single Piles in Sands*. Texas A&M University, College Station.

Long, J. H., & Vanneste, G. (1994). Effects of Cyclic Lateral Loads on Piles in Sand. *Journal of Geotechnical Engineering*, *120*(1), 225–244. https://doi.org/10.1061/(ASCE)0733-9410(1994)120:1(225)

Lu, W., & Zhang, G. (2020). New p-y curve model considering vertical loading for piles of offshore wind turbine in sand. *Ocean Engineering*, *203*, 107228. https://doi.org/10.1016/j.oceaneng.2020.107228

Ma, H., Yang, J., & Chen, L. (2017). Numerical analysis of the long-term performance of offshore wind turbines supported by monopiles. *Ocean Engineering*, *136*, 94–105. https://doi.org/10.1016/j.oceaneng.2017.03.019

Mašín, D. (2019). *Modelling of Soil Behaviour with Hypoplasticity: Another Approach to Soil Constitutive Modelling*. Springer International Publishing. https://doi.org/10.1007/978-3-030-03976-9

McAdam, R. A., Byrne, B. W., Houlsby, G. T., Beuckelaers, W. J. A. P., Burd, H. J., Gavin, K., Igoe, D., Jardine, R. J., Martin, C. M., Muir Wood, A., Potts, D. M., Skov Gretlund, J., Taborda, D. M. G., & Zdravković, L. (2019). Monotonic laterally loaded

pile testing in a dense marine sand at Dunkirk. *Géotechnique*, 1–13. https://doi.org/10.1680/jgeot.18.PISA.004

McClelland, B., & Focht, J. (1956). Soil Modulus for Laterally Loaded Piles. *Journal of the Soil Mechanics and Foundations Division*, *82*(4), 1–22.

McGann, C. R., Arduino, P., & Mackenzie-Helnwein, P. (2011). Applicability of Conventional p-y Relations to the Analysis of Piles in Laterally Spreading Soil. *Journal of Geotechnical and Geoenvironmental Engineering*, *137*(6), 557–567. https://doi.org/10.1061/(ASCE)GT.1943-5606.0000468

Meyerhof, G. G., & Sastry, V. V. R. N. (1985). Bearing capacity of rigid piles under eccentric and inclined loads. *Canadian Geotechnical Journal*, *22*(3), 267–276.

Miner, M., & others. (1945). Cumulative fatigue damage. *Journal of Applied Mechanics*, *12*(3), A159–A164.

Mrŏz, Z. (1967). On the description of anisotropic workhardening. *Journal of the Mechanics and Physics of Solids*, *15*(3), 163–175. https://doi.org/10.1016/0022-5096(67)90030-0

Mrŏz, Z., Norris, V. A., & Zienkiewicz, O. C. (1978). An anisotropic hardening model for soils and its application to cyclic loading. *International Journal for Numerical and Analytical Methods in Geomechanics*, *2*(3), 203–221. https://doi.org/10.1002/nag.1610020303

Murchison, J. M., & O'Neill, M. W. (1984). Evaluation of p-y Relationships in Cohesionless Soils: Analysis and design of pile foundations. *Proceedings of Symposium in Conjunction with the ASCE National Convention, San Francisco, CA. ASCE*, 174–191.

Murphy, G., Igoe, D., Doherty, P., & Gavin, K. (2018). 3D FEM approach for laterally loaded monopile design. *Computers and Geotechnics*, *100*, 76–83. https://doi.org/10.1016/j.compgeo.2018.03.013

Niemunis, A. (2003). *Extended Hypoplastic Models for Soils* [Habilitation]. Schriftenreihe des Institutes für Grundbau und Bodenmechanik der Ruhr-Universität Bochum.

Niemunis, A., & Herle, I. (1997). Hypoplastic model for cohesionless soils with elastic strain range. *Mechanics of Cohesive-Frictional Materials*, *2*(4), 279–299.

Niemunis, A., Wichtmann, T., & Triantafyllidis, Th. (2005). A high-cycle accumulation model for sand. *Computers and Geotechnics*, *32*(4), 245–263. https://doi.org/10.1016/j.compgeo.2005.03.002

Pastor, M., Zienkiewicz, O. C., & Chan, A. H. C. (1990). Generalized plasticity and the modelling of soil behaviour. *International Journal for Numerical and Analytical Methods in Geomechanics*, *14*(3), 151–190. https://doi.org/10.1002/nag.1610140302

Peralta, P. (2010). *Investigations on the behavior of large diameter piles under long-term lateral cyclic loading in cohesionless soil* [PhD]. Leibniz University.

Pérez Bedoya, E., & Osorio Osorio, J. A. (2002). *Energía, pobreza y deterioro ecológico en Colombia: Introducción a las energías alternativas*. Todográficas.

Poblete, M., Fuentes, W., & Triantafyllidis, Th. (2016). On the simulation of multidimensional cyclic loading with intergranular strain. *Acta Geotechnica*, *11*(6), 1263–1285. https://doi.org/10.1007/s11440-016-0492-2

Prasad, Y. V. S. N., & Chari, T. R. (1999). Lateral capacity of model rigid piles in cohesionless soils. *Soils and Foundations*, *39*(2), 21–29.

Reese, L. C., & Van Impe, W. (2011). *Single Piles and Pile Groups Under Lateral Loading*. Taylor and Francis.

Reese, Lymon C., Cox, W. R., & Koop, F. D. (1974). Analysis of Laterally Loaded Piles in Sand. *OTC-2080-MS*.

Reese, Lymon C, & Matlock, H. (Eds.). (1956). *Non-dimensional solutions for laterally-loaded piles with soil modulus assumed proportional to depth*. Association of Drilled Shaft Contractors.

Robertson, P. K., & Campanella, R. G. (1983). Interpretation of cone penetration tests. Part I: Sand. *Canadian Geotechnical Journal*, *20*(4), 718–733. https://doi.org/10.1139/t83-078

Roscoe, K. H., & Burland, J. B. (1968). *On the generalized stress-strain behaviour of wet clay*. *Cambridge University Press*.

Sheil, B. B., & McCabe, B. A. (2017). Biaxial Loading of Offshore Monopiles: Numerical Modeling. *International Journal of Geomechanics*, *17*(2), 04016050. https://doi.org/10.1061/(ASCE)GM.1943-5622.0000709

Sørensen, S. P. H. (2012). *Soil-Structure Interaction for Non-Slender, Large-Diameter Offshore Monopiles* [PhD Thesis]. Department of Civil Engineering, Aalborg University.

Sørensen, S. P. Hyldal., Ibsen, L. B., & Augustesen, A. H. (2010). Effects of Diameter on Initial Stiffness of p-y Curves for Large-Diameter Piles in Sand. In T. Benz & S. Nordal (Eds.), *Numerical Methods in Geotechnical Engineering: Proceedings of the seventh european conference on numerical methods in geotechnical engineeering* (pp. 907–912). CRC Press.

Staubach, P., & Wichtmann, T. (2020). Long-term deformations of monopile foundations for offshore wind turbines studied with a high-cycle accumulation model. *Computers and Geotechnics, 124*, 103553. https://doi.org/10.1016/j.compgeo.2020.103553

Tolooiyan, A., & Gavin, K. (2011). Modelling the Cone Penetration Test in sand using Cavity Expansion and Arbitrary Lagrangian Eulerian Finite Element Methods. *Computers and Geotechnics*, *38*(4), 482–490. https://doi.org/10.1016/j.compgeo.2011.02.012

UPME. (2015). *Integración de las energías renovables no convencionales en Colombia. Convenio de cooperación técnica UPME-BID ATN/FM-12825-CO.* Ministerio de Minas y Energía. Unidad de Planeación Minero Energética - UPME.

UPME. (2020). *Informe de Gestión 2019*. Ministerio de Minas y Energía. Unidad de Planeación Minero Energética - UPME.

Verdure, L., Garnier, J., & Levacher, D. (2003). Lateral cyclic loading of single piles in sand. *International Journal of Physical Modelling in Geotechnics*, *3*(3), 17–28. https://doi.org/10.1680/ijpmg.2003.030303

Vergara, W., Deeb, A., Toba, N., Cramton, P., & Leino, I. (2010). *Wind Energy in Colombia: A Framework for Market Entry. World Bank Study.* World Bank.

Versteijlen, W. G., Van Dalen, K. N., Metrikine, A. V., & Hamre, L. (2014). Assessing the small-strain soil stiffness for offshore wind turbines based on in situ seismic measurements. *Journal of Physics. Conference Series (Online)*, *524*. https://doi.org/10.1088/1742-6596/524/1/012088

von Wolffersdorff, P. A. (1996). A hypoplastic relation for granular materials with a predefined limit state surface. *Mechanics of Cohesive-Frictional Materials*, *1*(3), 251–271.

Wang, S., & Larsen, T. J. (2019). Permanent accumulated rotation of an offshore monopile wind turbine in sand during a storm. *Ocean Engineering*, *188*, 106340. https://doi.org/10.1016/j.oceaneng.2019.106340

Westermann, K., Zachert, H., & Wichtmann, T. (2014a). Vergleich von Ansätzen zur Prognose der Langzeitverformungen von OWEA-Monopilegründungen in Sand. Teil 1: Grundlagen der Ansätze und Parameterkalibration. *Bautechnik*, *91*(5), 309–323. https://doi.org/10.1002/bate.201300094

Westermann, K., Zachert, H., & Wichtmann, T. (2014b). Vergleich von Ansätzen zur Prognose der Langzeitverformungen von OWEA-Monopilegründungen in Sand. Teil 2: Simulationen und Schlussfolgerungen. *Bautechnik*, *91*(5), 324–332. https://doi.org/10.1002/bate.201400015

Wichtmann, T. (2005). *Explicit accumulation model for non-cohesive soils under cyclic loading* [PhD Thesis]. Schriftenreihe des Institutes für Grundbau und Bodenmechanik der Ruhr-Universität Bochum.

Wichtmann, T. (2016). *Soil Behaviour Under Cyclic Loading: Experimental Observations, Constitutive Description and Applications*.

Wichtmann, T., Niemunis, A., & Triantafyllidis, Th. (2008). Prediction of long-term deformations for monopile foundations of offshore wind power plants. *Geotechnics in Maritime Engineering. 11th Baltic Sea Geotechnical Conference*.

Wiemann, J. K., Lesny, K., & Richwein, W. (2004). Evaluation of Pile Diameter Effects on Soil-Pile Stiffness. *Dokumentation Der 7th German Wind Energy Conference DEWEK*.

WindEurope. (2020). *Offshore Wind in Europe: Key trends and statistics 2019*. WindEurope. windeurope.org

XM. (2019). *Reporte integral de sostenibilidad, operación y mercado 2019*. https://informeanual.xm.com.co/

Yang, M., Luo, R., & Li, W. (2018). Numerical study on accumulated deformation of laterally loaded monopiles used by offshore wind turbine. *Bulletin of Engineering Geology and the Environment*, *77*(3), 911–921. https://doi.org/10.1007/s10064-017-1138-9

Zachert, H., & Wichtmann, T. (2020). Approaches for the Design of Foundations for Offshore Wind Turbines. In T. Triantafyllidis (Ed.), *Recent Developments of Soil Mechanics and Geotechnics in Theory and Practice* (pp. 113–135). Springer International Publishing. https://doi.org/10.1007/978-3-030-28516-6_7

Zhang, L., Silva, F., & Grismala, R. (2005). Ultimate Lateral Resistance to Piles in Cohesionless Soils. *Journal of Geotechnical and Geoenvironmental Engineering*, *131*(1), 78–83. https://doi.org/10.1061/(ASCE)1090-0241(2005)131:1(78)